

PbS COLLOIDAL QUANTUM DOTS BASED
PHOTODETECTORS FOR INTEGRATED SWIR DETECTION

by

EMRE HEVES

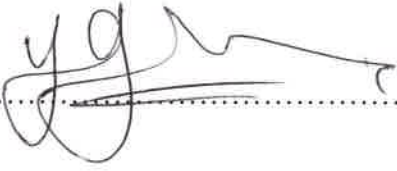
Submitted to the Graduate School of Engineering and Natural Sciences
in partial fulfillment of
the requirements for the degree of
Doctor of Philosophy

Sabancı University
Spring 2012

PbS COLLOIDAL QUANTUM DOTS BASED
PHOTODETECTORS FOR INTEGRATED SWIR DETECTION

APPROVED BY:

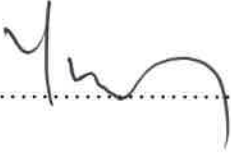
Prof. Dr. Yaşar Gürbüz
(Dissertation Supervisor)



Asst. Prof. Dr. Cem Öztürk
(Dissertation Co-advisor)



Prof. Dr. Yusuf Mencilođlu



Asst. Prof. Dr. Volkan Özgüz



Assoc. Prof. Dr. Şenol Mutlu



DATE OF APPROVAL 06.08.2012

© Emre Heves 2012

All Rights Reserved

PbS COLLOIDAL QUANTUM DOTS BASED PHOTODETECTORS FOR INTEGRATED SWIR DETECTION

Emre Heves

EL, Ph.D. Thesis, 2012

Thesis supervisor: Prof. Dr. Yaşar Gürbüz

Keywords: Infrared sensors, PbS colloidal quantum dots, short wave infrared, monolithic integration, plasmonic scattering

ABSTRACT

Due to the low water absorption and nightglow, sensing in short wave infrared (SWIR) is very attractive in applications such as; passive night vision, biomedical imaging and remote sensing. The monolithic integration of photodetectors to the read-out circuits is desirable in many applications to increase density of detectors and reduce costs, system size and power consumption. Solution-processed semiconductors are a promising alternative to conventional bulk crystalline photodetectors since their production is low cost and easy, their bandgap can be tuned depending on their sizes, and they can be easily integrated on any substrate. In this work, PbS colloidal quantum dot based photodiodes are realized that are compatible with the integration on Read Out Integrated Circuits (ROIC).

Various kinds of PbS quantum dots based schottky diodes are designed on glass and silicon substrates. Spin deposition steps and solid state ligand exchange processes are optimized to create pinhole free and high mobility PbS quantum dot layers. In addition to that Integrated Circuit (IC) compatible versions of PbS colloidal quantum dot (CQD) photodiodes are realized. ROIC chip surface is mimicked on Si substrates and fabrication steps are optimized for integration. Special importance is given to optimize highly conductive and transparent indium tin oxide layer using DC magnetron sputtering. Sensitivities of 1.4×10^{12} Jones, comparable to the conventionally used crystalline, bulk photodetectors is achieved. Also, plasmonic scattering effects of metal nanoparticles in PbS CQD layer are studied. Absorption and responsivity enhancement of 6 fold is presented using gold nanoparticles in PbS CQD based photoconductors.

KISA DALGA KIZILÖTESİ ALGILAMA İÇİN PbS KOLOİDAL KUANTUM NOKTA BAZLI FOTOALGILAYICILAR

Emre Heves

EL, Doktora Tezi, 2012

Tez Danışmanı: Prof. Dr. Yaşar Gürbüz

Anahtar Kelimeler: Kızılötesi algılayıcılar, PbS koloidal kuantum noktaları, kısa dalga kızılötesi, monolitik tümleştirme, plazmonik saçılma

ÖZET

Düşük su emilimi ve gece aydınlığı gibi özellikler nedeniyle kısa dalga kızılötesi algılama; pasif gece görüş sistemleri, biyomedikal görüntüleme ve uzaktan algılama gibi uygulamalar için önem kazanmaktadır. Foto detektörlerin okuma devrelerine (OD) monolitik tümleştirilmesine; detektör yoğunluğunu arttırmak ve maliyeti, güç tüketimini ve sistem boyutunu azaltmak için birçok uygulamada ihtiyaç duyulmaktadır. Solüsyon bazlı yarıiletkenler; üretim teknikleri ucuz ve kolay olması, bant genişliklerinin boyutlarına bağlı olarak ayarlanabilmesi ve herhangi bir tabana kolayca entegre edilebilmesi gibi özellikleri nedeniyle alışılmadık kristal foto detektörlere karşın umut verici bir alternatif olarak görülmektedirler. Bu çalışmada, OD'ye entegre edilebilecek, PbS koloidal kuantum noktaları (KKN) bazlı foto detektörler gerçekleştirilmiştir.

Bu çalışmada farklı tasarımlarda PbS KKN bazlı foto detektörler, cam ve silisyum tabanlar üzerine gerçekleştirilmiştir. Spin kaplama adımları ve katı hal ligand değişim süreçleri; delik ve çatlaklardan arındırılmış, yüksek hareketlilik kabiliyetine sahip PbS KKN katmanları oluşturmak için optimize edilmiştir. Buna ek olarak, PbS KKN foto detektörlerinin entegre devre uyumlu versiyonları gerçekleştirilmiştir. Okuma devresi yongasının yüzeyinin kopyası silisyum tabanlar üzerinde üretilmiş ve bu kopya üzerinde tamamen entegre PbS foto detektörler gerçekleştirilmiştir. Yüksek iletkenlik ve geçirgenlik özellikli indiyum kalay oksit katmanlarının DC sputter yöntemiyle kaplanma prosesinin optimizasyonuna önem gösterilmiştir. Gerçeklenen detektörlerde, konvansiyonel kristal foto detektörlerin hassaslık derecelerine, 1.4×10^{12} Jones, ulaşılmıştır. Ayrıca metal nano-parçacıkların PbS KKN katmanlarında plasmonic saçılma etkileri çalışılmıştır. Altın nano-parçacıklar kullanılarak PbS KKN katmanlarında 6 kattan yüksek bir emilim ve duyarlılık artışı elde edilmiştir.

To my wife

ACKNOWLEDGEMENTS

My journey in Sabanci University has begun in 1999 and now it is coming to an end as a student with this Ph.D. thesis. I owe to many people for all their support and belief in me in this journey. This thesis is the product of my Ph.D. study and is contributed by many people in both academic and personal aspects of my life.

Firstly, I would like to express my deep gratitude to my thesis supervisor Prof. Dr. Yaşar Gürbüz for guiding and mentoring me for long years. This thesis is realized by great support and farsightedness of him. I also am grateful for my thesis co-advisor Asst. Prof. Dr. Cem Öztürk for his support, his experience and motivation throughout the work. In addition, I would like to thank my jury member and also my director at SUNUM, Asst. Prof. Dr. Volkan Özgüz for his valuable feedbacks, support and patience throughout the thesis. I also appreciate the feedbacks and different perspective he brought in to thesis of Prof. Dr. Yusuf Menciloğlu who is also the dean of our faculty. I also would like to thank to Assoc. Prof. Dr. Şenol Mutlu for his valuable comments and directions he gave. Besides from my Jury, I would like to thank to Assoc. Prof. Meriç Özcan for his creative ideas and recommendations for the thesis.

I would like to thank; ROIC group Huseyin, Melik, Ömer and Burak for beneficial discussions and feedbacks; Emre, Tolga and İlker and; Reza and Irena for recommendations, SUNUM for providing many high tech fabrication and testing facilities, TUMSIS spin-off for providing Read-out IC's; SUNUM colleagues Dr. Javed, Dr. Anjum, Dr. Saravan, Dr. Burak, Dr. Meltem, Dr. Feray, Dr. Burcu, Dr. Serkan, Dr. Meral, Dr. Alp who turned this exhaustive process into an endurable work. Besides, I would like to especially thank to Bülent Koroğlu and Serkan Bostan for their helps and clever solutions in technical problems. I would also like to than lab specialists Ali and Mehmet for their supports. Many thanks to my colleagues from materials department, especially my close friend for years Dr. Eren, my old home mate Dr Deniz, Mustafa, Oğuz, Kağan, Hasan, Melike, Burcu and many others I could not recall.

Finally and most importantly, I would like to express my deepest gratitude to my wife Işıl Heves and my families (Heves and İsmet). Their constant encouragement, unflinching support and boundless love have always been the true sources of strength and inspiration throughout my life. Thank you with all my heart.

TABLE OF CONTENTS

Abstract	iv
Özet	v
Acknowledgements	vii
Chapter 1	1
Introduction	1
1.1 Optical Detection History	1
1.2 IR Detection Applications	4
1.3 IR Market Shift	5
1.4 SWIR Detection	6
1.4.1 Nightglow	6
1.4.2 SWIR Imaging Advantages	7
1.4.3 SWIR Applications	9
1.4.4 SWIR Detector Types	11
1.5 Drawbacks of Current SWIR Detectors	11
1.6 Thesis Objectives	13
1.7 Thesis Overview	14
Chapter 2	17
Colloidal Quantum dot photodetectors	17
2.1 Colloidal Quantum Dots	17
2.2 Synthesis of Colloidal Quantum Dots	19
2.3 CQD Based Photodetectors	20
2.3.1 Photodiode Detectors	21
2.3.2 Photoconductive Detectors	23
2.4 Noise Sources	24
2.4.1 Photon noise	24
2.4.2 Detector noise	25

2.5	Photodetector Performance Parameters	27
2.5.1	Dark Current (I_d).....	27
2.5.2	Responsivity (R).....	28
2.5.3	Quantum Efficiency (QE).....	28
2.5.4	Noise Equivalent Power (NEP).....	28
2.5.5	Detectivity (D^*).....	29
2.6	CQD Photodetectors Previous Works.....	29
Chapter 3		32
PbS CQD Photodiodes		32
3.1	Photodiode Topography Selection	33
3.2	Colloidal Quantum Dot Schottky Photodiode Structure.....	35
3.2.1	PbS Colloidal Quantum Dots	35
3.2.2	CQD Schottky Photodiode Architecture	36
3.3	Deposition of CQD PbS films.....	40
3.3.1	Spin Coating	40
3.3.2	Dip coating	40
3.3.3	Inkjet printing	40
3.3.4	Layer by layer spin deposition of PbS CQDs.....	42
3.4	Surface Modification on CQD Films: Ligand exchange.....	45
3.5	Schottky Metal Deposition.....	48
3.6	Measurement procedure and results.....	50
3.6.1	Test setup.....	50
3.6.2	Test and characterization of Al/PbS CQD photodiode.....	52
3.6.3	Test and characterization of Au-Ti/PbS CQD photodiode.....	56
3.6.4	Results and Discussion	58
Chapter 4		62
IC Integrable Pbs CQD Photodetectors.....		62

4.1	Read-out Integrated Circuits Integration.....	63
4.2	ITO Deposition Optimization	64
4.2.1	General properties of ITO	65
4.2.2	Electrical Properties of ITO.....	65
4.2.3	Sputter Processing of ITO	67
4.2.4	Results	67
4.3	PbS CQD Photodiodes on Si Substrates	69
4.3.1	PbS CQD Photodiode structure	69
4.3.2	Fabrication Process.....	70
4.3.3	Measurement Setup	72
4.3.4	Measurement Results.....	73
4.4	PbS CQD Photodiodes on Mimic of ROIC.....	78
4.4.1	ROIC Mimic.....	79
4.4.2	Test Setup and Measurements of PbS CQD photodiodes on ROIC mimic	84
4.5	Results and Discussion.....	86
Chapter 5		89
Plasmonics in PbS CQD Photoconductors		89
5.1	PbS CQD based photoconductor.....	90
5.1.1	Structure and fabrication of PbS CQD based photoconductor	90
5.1.2	Test setup and measurements of PbS CQD photoconductors	92
5.2	Responsivity Enhancement of PbS Photoconductors Using Plasmonics	96
5.2.1	Plasmonic PbS photoconductor structure	96
5.2.2	Fabrication of plasmonics enhanced PbS CQD photoconductors	97
5.2.3	Measurement results	98
5.3	Results and Discussion.....	103
Chapter 6		105

Conclusions & Future Work.....	105
References	113
Appendix I.....	118

LIST OF FIGURES

Figure 1. Electromagnetic spectrum [1]	1
Figure 2. History of the development of infrared detectors [13].....	3
Figure 3. Various applications for IR detectors [14].....	4
Figure 4. Sketch of the Air Glow Process in the Infrared [17]	6
Figure 5. Night time illumination sources.....	7
Figure 6. Visible (left) and SWIR (right) image of a Humvee. In SWIR, the camouflage is less effective [19].	8
Figure 7. Building scene in the presence of fog recorded by visible camera (on the left) and by a SWIR camera [20].	8
Figure 8. Imagery taken with a SWIR camera of a hotel from more than a mile away in the midst of haze. Frame on the top right is the same hotel and weather conditions imaged with a commercial visible camera [21].	9
Figure 9. Various detectors used for infrared detection with their normalized detectivities and operating wavelength. Uncooled SWIR detectors are marked with rectangles [23].....	12
Figure 10. The absorption spectrum of PbS for a range of QD sizes [29]	18
Figure 11. Setup for colloidal quantum dot synthesis.....	19
Figure 12. A schematic representation of the organometallic CQD growth process. Synthesis results in inorganic crystalline semiconductor cores surrounded by organic ligands that passivate the crystal surface, as shown in the final step of the growth process [30].	20
Figure 13. a) Spatial band diagram of photodiode b) The structure of CQD photodiode [31].....	22
Figure 14. a) Spatial band diagram of photoconductor b) The structure of CQD photodiode [31].....	24
Figure 15. Absorption & emission spectra of 5.3 nm PbS quantum dots.1st excitation peak of absorption is at 1450 nm whereas emission peak is at 1532 nm. (Provided by Evident Technologies)	35
Figure 16. High resolution TEM images of PbS CQDs. On the left a monolayer of close packed CQDs is shown. On the right a close-up view of a single quantum dot is shown [52]	36
Figure 17. Equilibrium energy band diagram of Schottky-barrier junction of metal/p-type semiconductor [14].....	37

Figure 18. 3D schematic of the PbS quantum dots based schottky photodiode composed of ITO anode, photosensitive PbS quantum dot layer and schottky cathode composed of Ti and Au stack or Al.	38
Figure 19. The Schottky barrier at the Ti-Au or Al CQD interface forms a depletion region (DR) in the CQD film with a bias dependent width (w_{DR}) and a built in potential (V_{bi}). The remaining CQD film is unaffected by the Schottky barrier and is denoted as quasi-neutral region (QNR) [53].....	39
Figure 20. Transmission spectra of the glass samples and the ITO coated glass samples used in the work provided by Teknoma [54].....	39
Figure 21. Schematic of spin deposition process including drop, spread, coat, dehydrate steps [47].....	41
Figure 22. Steps of dip coating deposition process [47]	41
Figure 23. Schematic representation of inkjet printing [47]	41
Figure 24. Poor quality PbS CQD films with pinholes and cracks as a result of low concentration PbS in toluene use	43
Figure 25. Pinhole free good quality PbS CQD films achieved with optimized concentration and layer by layer deposition process	44
Figure 26. EDS analysis of the PbS CQD layer coated on Al deposited Si/SiO ₂ substrates. The Pb, S peaks can easily be seen together with C and O peaks that come from oleic acid.	44
Figure 27. Long chain of oleic acid (C ₁₈ H ₃₄ O ₂) used for organic ligand for passivation and solubility of PbS colloidal quantum dots. a) 3D molecular illustration where black spheres stands for H ₂ , white spheres stands for C and red ones are O atoms [59].....	46
Figure 28. Structure of originally oleic acid capped PbS QD and the shorter ligands to replace long OA chain [57].....	46
Figure 29. DC probe station equipped with shielded enclosure used for electrical and optical characterization	50
Figure 30. Probe station chuck is replaced with optic table for exposing the device from the bottom with a fiber cable.....	51
Figure 31. Since the contact areas are very small, photodiodes are measured with the help of Tungsten probes. The photodiode is illuminated from the bottom.....	51
Figure 32. I-V characteristic of Al/PbS CQD schottky photodiode under dark conditions. Strong rectification is observed at ± 1 and 2 volt applied bias voltages.	53

Figure 33. I-V curves of Al/PbS CQD schottky photodiode under dark (black curve) and under 5 mW/cm ² illumination (red curve)	54
Figure 34. I-V curves of Al/PbS CQD schottky photodiode under dark (black curve), and under 5 mW/cm ² illumination centered at 1527 nm (red curve), 1547 nm (blue curve) and 1567 nm (magenta curve).	55
Figure 35. I-V characteristic of Ti-Au/PbS CQD schottky photodiode under dark conditions. Strong rectification is observed at ±1.5 volt applied bias voltages.....	56
Figure 36. I-V curves of Al/PbS CQD schottky photodiode under dark (black curve) and under 5 mW/cm ² illumination (red curve)	57
Figure 37. Comparison of dark current and photoresponse of Al/PbS and Au-Ti/PbS schottky photodiodes	59
Figure 38. Read-out circuit for FPA integration. Pond pad openings for each pixel is shown on zoomed picture (top left)	63
Figure 39. Schematic cross-section of the ROIC and PbS CQD photodetectors integration	64
Figure 40. The experimental and calculation of the carrier concentration as function of the tin doping level [80]	66
Figure 41. 3D schematic of the PbS quantum dots based schottky photodiode fabricated on Si substrate, composed of ITO anode, photosensitive PbS quantum dot layer and Al schottky cathode.....	69
Figure 42. PbS CQD layer on top of Al coated Si/SiO ₂ substrate during layer by layer deposition process that takes place on spin coater. The layer has a shiny and yellowish/light brown color	70
Figure 43. 20mm x 20 mm size aluminum sheet hard masks that have 0.4 mm diameter holes on them.	71
Figure 44. Tungsten-Halogen lamp spectral distribution [81]	72
Figure 45. The graph of the illumination power measured by optical power meter system at 1550 nm, 1310 nm and 890 nm wavelength, with respect to different color temperature adjusted by Motic light source.....	73
Figure 46. I-V graph of Al/PbS photodiode on Si substrate under dark. Rectification over 10 is achieved between ±2V	75
Figure 47. I-V curves of Al/PbS CQD schottky photodiode under dark (black curve) and under 140 μW/cm ² illumination (red curve)	75

Figure 48. Bias voltage vs diode current graph for irradiance between 8,469 $\mu\text{W}/\text{cm}^2$ and 134,093 $\mu\text{W}/\text{cm}^2$	76
Figure 49. Photocurrent change depending on irradiance measured under 1V reverse bias. Linear behavior is observed from 8,469 $\mu\text{W}/\text{cm}^2$ and 134,093 $\mu\text{W}/\text{cm}^2$	77
Figure 50. Schematic of mimicking the top layer of ROIC and fabricating PbS photodiodes in order to test integration	78
Figure 51. Size and spacing of pixels measured from ROIC chip. The bond pad openings are 5 μm x 5 μm and the vertical spacing of pixels are 33 μm from center to center and horizontal spacing is 40 μm	80
Figure 52. The mimic chip layout for 2 x 3 pixel array with the size of 5 μm x 5 μm . Pads are connected to each pixel for testing.....	80
Figure 53. Fabrication steps of PbS CQD photodiodes integrated on ROIC mimic	81
Figure 54. Microscope picture of patterned bottom Al contacts. The bottom contact has a size of 6,5 μm x 6,5 μm	82
Figure 55. Microscope picture of the oxide over the Al layer is patterned and the bond pond areas left open which defines the photodiode area.	83
Figure 56. PbS diode picture after ITO etch.	83
Figure 57. I-V characteristics of PbS CQD diode under dark.....	84
Figure 58. I-V characteristics of the sample under dark and under 140 $\mu\text{W}/\text{cm}^2$ illumination.....	85
Figure 59. 3D illustration of PbS CQD based photodiode	91
Figure 60. I-V characteristics of PbS CQD photoconductor under dark conditions	92
Figure 61. I-V characteristics of photoconductor under dark and under 140 $\mu\text{W}/\text{cm}^2$ illumination.....	93
Figure 62. Responsivity change due to the applied bias. At higher biases responsivity increases due to higher electric field.....	94
Figure 63. Photocurrent vs. bias voltage graph for irradiances between 8,5 $\mu\text{W}/\text{cm}^2$ to 134 $\mu\text{W}/\text{cm}^2$	95
Figure 64. Photoconductor current change due to the irradiance change	95
Figure 65. a) Conventional PbS CQD photoconductor b) gold nanoparticles applied for plasmonic scattering to enhancer responsivity c) absorption and reflection in	

conventional PbS CQD photoconductor d) gold nanoparticles scatter incident light more into the PbS film enhancing absorbance thus enhancing responsivity	96
Figure 66. Two different concentration of colloidal gold nanoparticle solution in citrate is prepared; one 0.01% and the other is 0.1% in citrate.....	98
Figure 67. I-V graph of reference sample under dark and 140 $\mu\text{W}/\text{cm}^2$ illumination.....	99
Figure 68. I-V graph of the sample that 0.01% gold nanoparticles is applied, under dark and 140 $\mu\text{W}/\text{cm}^2$ illumination.....	100
Figure 69. I-V graph of the sample that 0.1% gold nanoparticles is applied, under dark and 140 $\mu\text{W}/\text{cm}^2$ illumination.....	101
Figure 70. I-V graphs of all three samples under dark and under illumination. .	101
Figure 71. Responsivity of the thre devices for changing bias voltages. Responsivity increases with introducing Au nanoparticles.	102
Figure 72. Schematic of the sputtering system.....	118
Figure 73. A 4PP consists of equally spaced tungsten carbide points that are brought into contact with a layer (left). The spreading of current flow between probes 1 and 4 and the resulting electrostatic fields must be considered in calculating semiconductor resistivity from 4-point probe measurements.....	121
Figure 74. Thickness of sample #2 measured by surface profilometer.....	122
Figure 75. Sample #2 Transmittance between 700 nm – 200 nm	122
Figure 76. Thickness of sample #3 measured by surface profilometer.....	123
Figure 77. Transmission graph of sample #3 between 700-2000 nm wavelengths	123
Figure 78. Thickness of sample #4 measured by surface profilometer.....	124
Figure 79. Thickness of sample #5 measured by surface profilometer.....	124
Figure 80. . Transmittance graph of sample #4 between 700-2000 nm wavelengths	125
Figure 81. Transmittance graph of sample #5 between 700-2000 nm wavelengths. Transmittance decreased dramatically to 47.011% at 1450 nm	126
Figure 82. Measured thickness of sampe #6.	126
Figure 83. Transmittance graph of sample #6 between 700-2000 nm wavelength	127
Figure 84. 4 min sputtering at 350 W DC power resulted 150 nm thicknesses for sample #6	128

Figure 85. Transmittance graph of sample #7 in the range between 1000-1700 nm	128
.....	
Figure 86. Thickness measurement of sample #8	129
Figure 87. Transmittance graph of sample #8 in the range between 1000-1700 nm	130
.....	
Figure 88. Transmittance graph of sample #9 between 700 nm and 2000 nm....	130
Figure 89. Thickness of sample #10 is measured as 222 nm.	131
Figure 90. Transmittance graph of sample #10	131
Figure 91. Transmittance graph of sample #11	132
Figure 92. Thickness of sample #12. 7 min deposition at 200W resulted in 146 nm thickness.....	132
Figure 93. Transmittance graph of Sample #12	133
Figure 94. Measured thickness of sample #13. 10 min deposition with 150 W DC power resulted in 230 nm thickness.....	134
Figure 95. Transmittance graph of sample #13. 87.733 % transmittance is measured at 1450 nm	134

LIST OF TABLES

Table 1. Solution based photodetector review	31
Table 2. List of process steps used in layer by layer spin coating of PbS QDs and ligand exchange procedures.....	47
Table 3. Sputter deposition parameters of Schottky contact metals.....	49
Table 4. Comparison of PbS CQD photodiodes on glass realized in this work with the state of the art solution based photodiodes in the literature.....	61
Table 5. Summary of sputter deposition parameters and the measurement results of all the samples created.....	68
Table 6. Comparison of PbS CQD photodiodes on glass, silicon and ROIC, which are realized in this work, with the state of the art solution based photodiodes in the literature	88
Table 7. Comparison of PbS CQD photoconductors realized in this work, with the state of the art solution based photoconductors in the literature.....	104

Chapter 1

INTRODUCTION

1.1 Optical Detection History

Light detection has been an important sensory mechanism in various kinds of applications throughout the years. Human interest in light naturally centers on the visible part of the spectrum. The visible spectrum is the portion of the electromagnetic spectrum that is visible to (can be detected by) the human eye, responding to wavelengths from about 390 to 750 nm, as shown in Figure 1. Visible imaging applications include surveillance, machine vision, industrial inspection, spectroscopy, and fluorescent biomedical imaging. However, the visible light that we are all used to seeing and recording represents just a small fraction of the information that radiation carries about our world (Figure 1).

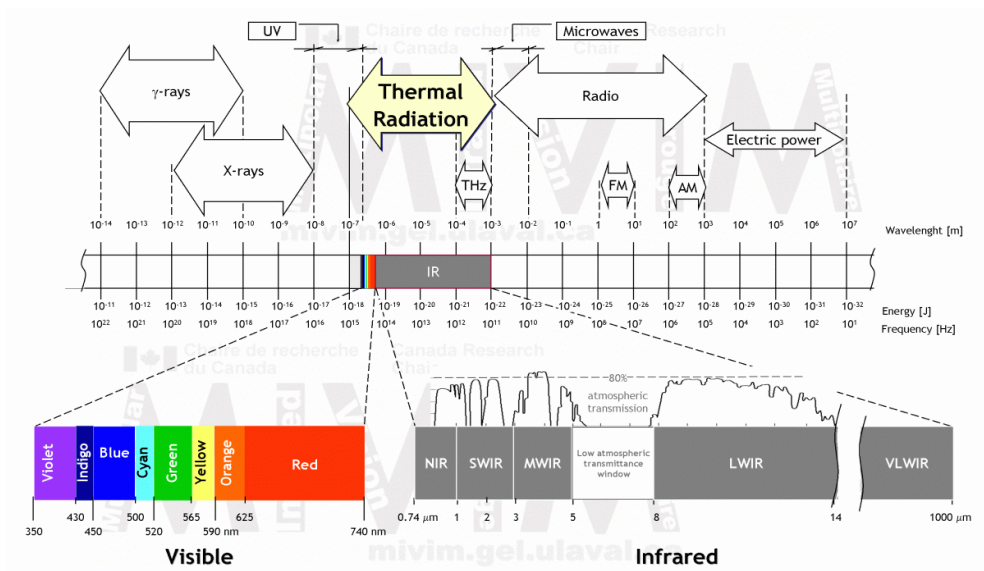


Figure 1. Electromagnetic spectrum [1]

Over the last several hundred years, our ability to detect and measure light has expanded to include UV and IR wavelengths through the development of detectors to

supplement the range of sensitivity of the human eye. Infrared portion of the radiation spectrum is only discovered approximately 210 years ago in Herschel's experiments with the thermometer. In order to measure the distribution of energy in sunlight, he built a simple monochromator and measure different colored rays and made measurements under visible rays and out of visible rays as well. The progress of developing an IR detector is connected mainly with thermal detectors and the most important steps in this progress can be listed as; Seebeck's discovery of thermoelectric effect and presentation of first thermocouple in 1921, Nobili's demonstration of the first thermopile by connecting a number of thermocouples in series in 1929, and Melloni's modification in thermocouple design by using bismuth and antimony [2]. Langley's bolometer that is composed of two thin ribbons of platinum foil connected to form two arms of Wheatstone bridge is appeared in 1880. With 20 years effort, he developed the bolometer as 400 times more sensitive than the first version so that he can detect heat of objects from a distance of a quarter mile.

In addition to thermal detectors, which are commonly used topology in early development phase, photon detectors are started appearing in 1900's and first IR photoconductors was developed by Case in 1917. Also in 1933 Kutzscher discovered lead sulphide (PbS) was photoconductive and had response to spectrum around 3 μm wavelength. Many materials and topologies have been investigated in the IR field later on such as, thermoelectric power (thermocouples), change in electrical conductivity (bolometers, pyroelectricity/pyroelectric detectors), internal emission (PtSi Schottky barriers), fundamental absorption (intrinsic photodetectors), impurity absorption (extrinsic photodetectors), low-dimensional solids (superlattice (SL)) and quantum well (QW) and quantum dot (QD) detectors, different type of phase transitions etc. [2]. Figure 2 gives the development efforts of IR detectors in years. Modern IR detector technology started in 60's with the advances in narrow bandgap semiconductor alloys such as III-V ($\text{InAs}_{1-x}\text{Sb}_x$), IV-VI ($\text{Pb}_{1-x}\text{Sn}_x\text{Te}$), and II-VI ($\text{Hg}_{1-x}\text{Cd}_x\text{Te}$). These alloys allowed the bandgap of the semiconductor and hence the spectral response of the detector to be custom tailored for specific applications. The fundamental properties of narrow-gap semiconductors (high optical absorption coefficient, high electron mobility, and low thermal generation rate), together with the capability for bandgap engineering, make these alloy systems almost ideal for a wide range of IR detectors Photon IR technology combined with semiconductor material science and photolithography

technology developed for integrated circuits resulted in extraordinary advances in IR sensing capabilities during the last century. Exactly, HgCdTe has inspired the development of the three “generations” of detector devices Figure 2. The first generation, linear arrays of photoconductive detectors, has been produced in large quantities and is in widespread use today. The second generation two-dimensional (2-D) arrays of photovoltaic detectors, also called Focal Plane Arrays – FPA, are now in high-rate production. At the present stage of development, staring arrays have more than 10^6 elements and are scanned electronically by control / process electronics circuits integrated with the arrays. These 2-D arrays of photodiodes connected with indium bumps to a readout integrated circuit (ROIC) chip as a hybrid structure are often called a sensor chip assembly (SCA). Third-generation devices defined here to encompass the more exotic device structure embodied in two-color detectors and hyper-spectral arrays and are now in demonstration programs. Both HgCdTe photodiodes [3-5] and QWIPs [6-8] are reported to offer multicolor capability in the SWIR, MWIR, and LWIR range. Recently, type II InAs/GaInSb superlattices [9, 10] and QDIPs [11, 12] have emerged as possible candidates for third generation infrared detectors.

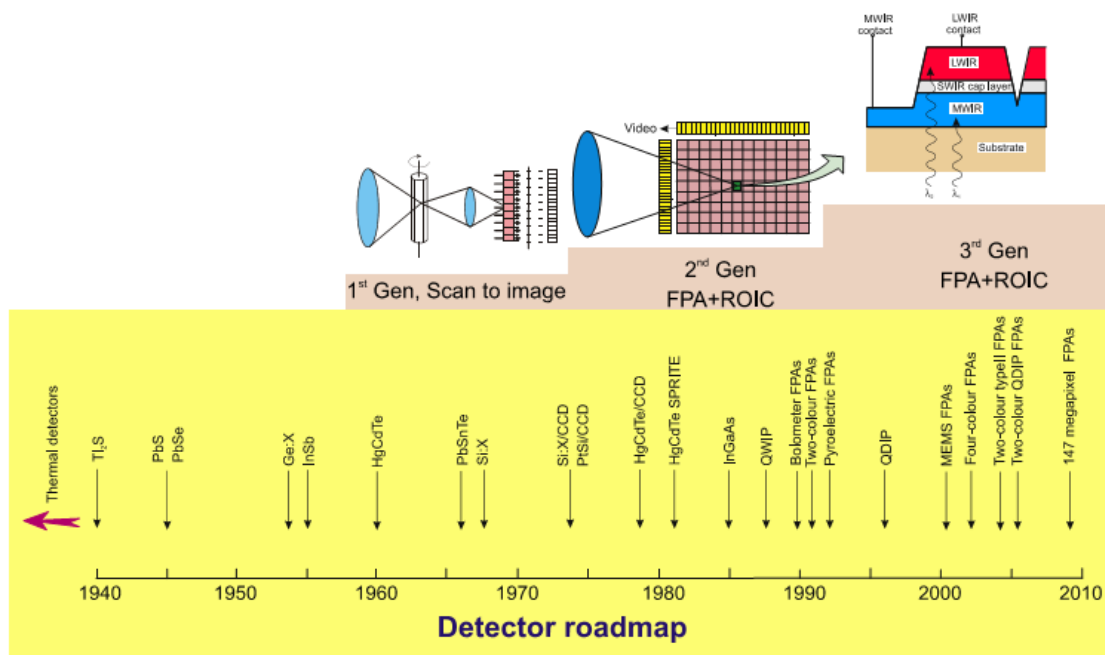


Figure 2. History of the development of infrared detectors [13].

The development of IR technology has been dominated by the photon detectors since about 1930's. However, the photon detectors require cryogenic cooling. This is necessary to prevent the thermal generation of charge carriers. The thermal transitions

compete with the optical ones, making uncooled devices very noisy. The cooled thermal camera usually uses the Sterling cycle cooler, which is the expensive component in the photon detector IR camera, and the cooler's lifetime is only around 10,000 hours. Cooling requirements are the main obstacle to the widespread use of IR systems based on semiconductor photon detectors making them bulky, heavy, expensive, and inconvenient to use.

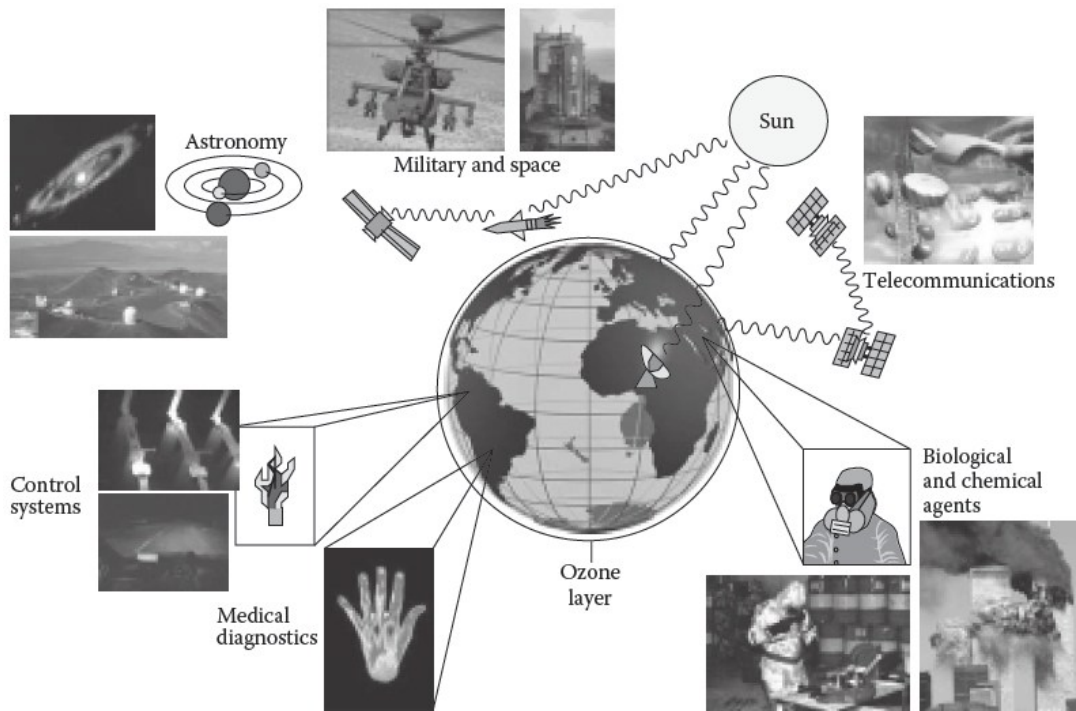


Figure 3. Various applications for IR detectors [14].

1.2 IR Detection Applications

Traditionally, infrared (IR) technologies are closely connected with controlling functions and night-vision. They are commonly used for military applications such as night-vision, recognition and surveillance systems, tank sight systems, anti-tank missiles, air-air missiles, etc. Most of the funding for IR detectors has been provided to fulfill military needs, but commercial applications have increased continuously, especially since the last decade of the twentieth century. These include medical, industry, earth resources, and energy conservation applications as shown in Figure 3. Medical applications include thermography in which IR scans of the body detect cancers or other trauma, which raise the body surface temperature. Earth resource determinations are done by using IR images from satellites in conjunction with field

observation for calibration. In some cases even the health and growth state of a crop is determined from space. Energy conservation in homes and industry has been aided by the use of IR scans to determine the points of maximum heat loss. Demands for these technologies are quickly growing due to their effective applications, for example, in global monitoring of environmental pollution and climate changes, longtime prognoses of agriculture crop yield, chemical process monitoring, Fourier transform IR spectroscopy, IR astronomy, driving safety of automobiles, IR imaging in medical diagnostics, and others.

1.3 IR Market Shift

The landscape of the infrared market has changed tremendously over the past 20 years, expanding in terms of commercial applicability, number of available components, widespread adoption and extreme growth in overall market value. The IR market was once entirely categorized and dominated by military applications and government funding. However, due to the recent decline in the costs of IR detectors,, the paradigm is shifting and more IR applications are becoming available in commercial markets. In 2008, a Maxtech International Inc. and Flir Systems Inc. report [15] estimated that the worldwide IR market totaled \$6.6 billion with approximately \$2.4 billion tied specifically to IR imaging systems. And it has been projected that these markets continuing to grow at a compound annual growth rate of 15% through 2012, whereas more aggressive estimates predict growth of greater than 25% well into 2015 [15].

In the mid-1990s, the military IR market began to reach a point of technological saturation because of the long development cycle of second-generation focal plane arrays [15]. Yet, after the release of those arrays, the military market has seen a tremendous growth. Lately, the growth in the military sector is once again begins to slow, but, thanks to commercial IR sector, the decrease in military sector is compensated. The increase in the share of commercial devices is driven by the advancements in sensor technology. The advancements are focused on the integration of microelectronics with sensors and decreasing the production process costs, which will accelerate the commercial IR market [15].

1.4 SWIR Detection

Short Wavelength Infra-Red (SWIR) spectrum falls in between $1\mu\text{m}$ - $3\mu\text{m}$ as seen in Figure 1. Unlike Mid-Wave Infrared (MWIR) ($3\mu\text{m}$ - $5\mu\text{m}$) and Long-Wave Infrared (LWIR) ($8\mu\text{m}$ - $14\mu\text{m}$) light, which is emitted from the object itself; SWIR is similar to visible light in that photons are reflected or absorbed by an object, providing the strong contrast needed for high resolution imaging. Ambient star light and background radiance (nightglow) are natural emitters of SWIR and provide excellent illumination for outdoor, night-time imaging.

1.4.1 Nightglow

Nightglow is the very weak emission of light by a planetary atmosphere. In the case of Earth's atmosphere, this optical phenomenon causes the night sky to never be completely dark (even after the effects of starlight and diffused sunlight from the far side are removed). The airglow phenomenon was first identified in 1868 by Swedish scientist Anders Ångström [16]. Since then it has been studied in the laboratory, and various chemical reactions have been observed to emit electromagnetic energy as part of the process. In the short wave infrared (SWIR) between $1.0\ \mu\text{m}$ and $1.7\ \mu\text{m}$, it is due to emissions from hydroxyl radicals transitioning from excited rotational and translational states to lower energy states and emitting a SWIR photon in the process.

During the day, UV photons strike water molecules and initiate the production of hydrogen and ozone. At night, the hydrogen and ozone recombine and form the excited hydroxyl radicals with elevated vibration and rotational energy states. The molecules then transition to a lower energy state emitting a SWIR photon. The process can be quenched by other molecules, among them O_2 and N_2 , which carry off the energy [17].

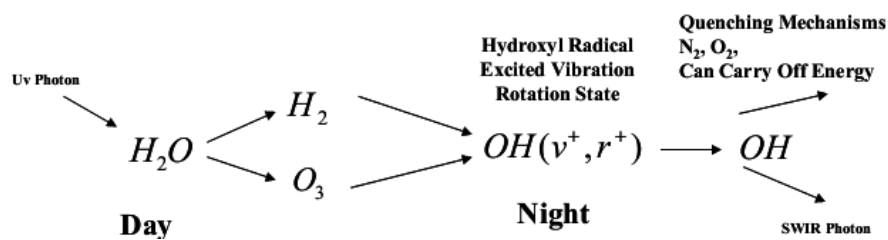


Figure 4. Sketch of the Air Glow Process in the Infrared [17]

The moon, airglow, integrated starlight and zodiacal light are all illumination sources at night time. The moon is the brightest source of all as seen in Figure 5. When the moon is not out, or is obscured by the clouds, sky glow provides a significant source much greater than thermal radiation in the SWIR band. Nightglow gives us the advantage that the photons that are emitted from the atmosphere will illuminate the objects in the night and by using SWIR detectors we can actually see these objects with strong contrast needed for high resolution imaging.

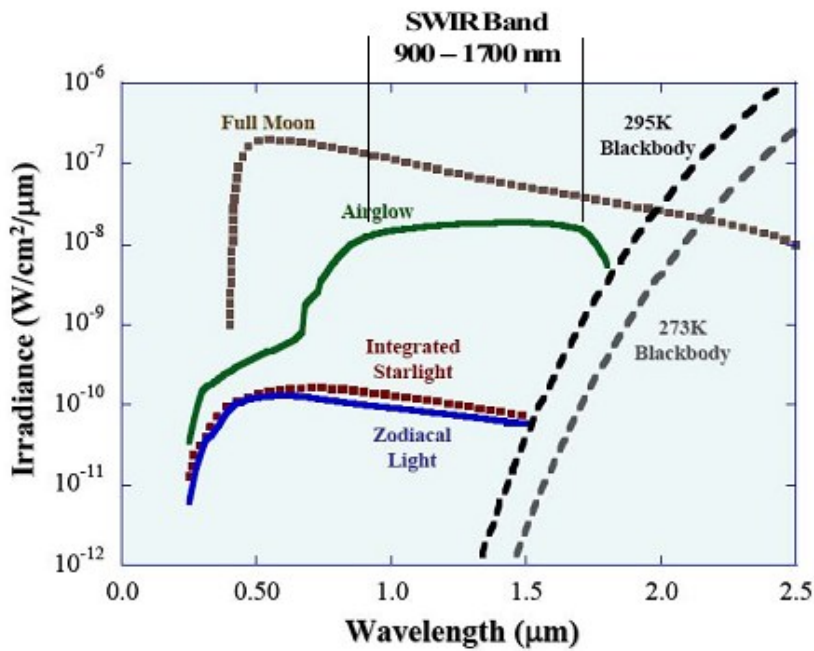


Figure 5. Night time illumination sources.

1.4.2 SWIR Imaging Advantages

The SWIR wavelength band offers unique imaging advantages over visible and thermal bands. Like visible cameras, the images are primarily created by reflected broadband light sources, so SWIR images are easier for viewers to understand. As a result of reflective principle, images from SWIR cameras also show shade and contrast, and are also comparable in resolution and detail with normal images under visible light. In Figure 6, the pictures of a Humvee are shown for both taken with SWIR and visible camera. It can be easily seen that camouflage pattern on the Humvee blends in the environment in the visible whereas, SWIR image gives better contrast and camouflage becomes less effective. Also, thermal imaging does not work well at dawn or dusk,

which are known as the crossover points. What surveillance experts discovered is that SWIR works well around the clock and especially well at those crossover points.

Most materials used to make windows, lenses, and coatings for visible cameras are readily usable for SWIR cameras, keeping costs down. Ordinary glass transmits radiation to about $2.5 \mu\text{m}$. Therefore, simple glass optics replaces lenses made from expensive special materials such as germanium, silicon or zinc selenide. Moreover, these kinds of cameras, unlike thermal IR cameras, require neither a lens shutter nor expensive cryo-cooling the array. Without these components, the reliability increases, the costs, overall size and weight fall, and the cameras are less sensitive to vibrations [18].



Figure 6. Visible (left) and SWIR (right) image of a Humvee. In SWIR, the camouflage is less effective [19].



Figure 7. Building scene in the presence of fog recorded by visible camera (on the left) and by a SWIR camera [20].



Figure 8. Imagery taken with a SWIR camera of a hotel from more than a mile away in the midst of haze. Frame on the top right is the same hotel and weather conditions imaged with a commercial visible camera [21].

SWIR cameras can image many of the same light sources, such as YAG laser wavelengths. Thus, with safety concerns shifting laser operations to the “eye-safe” wavelengths where beams won’t focus on the retina (beyond 1.4 μm), SWIR cameras are in a unique position to replace visible cameras for many tasks. Due to the reduced Rayleigh scatter of light at longer wavelengths, particulate in the air, such as dust or fog, SWIR cameras can see through haze better than visible cameras. Figure 7 and Figure 8 shows the comparison between SWIR and visible cameras while imaging a foggy scene.

1.4.3 SWIR Applications

1.4.3.1 Detection of laser designators

Many applications exist for lasers on the modern battlefield: range-finding lasers are used to detect the range of an object whereas target designator lasers are used for attack. The most common military lasers operate around 850 nm, 1060 nm, or 1550 nm. The first two types are visible to night vision goggles; the third one, 1550 nm, is therefore considered covert. SWIR cameras are able to see all three at the same time.

1.4.3.2 Night vision and target recognition

Thermal imaging cameras, such as LWIR uncooled microbolometer cameras, have excellent detection abilities at night. SWIR cameras however, are a good

complement to thermal imaging cameras. While thermal imaging can easily detect the presence of warm/hot objects, e.g., cars, trucks, people etc., in a cooler environment, a SWIR camera can be used to identify and recognize those objects. SWIR night vision is based on reflection of infrared rays from atmospheric glow or nightglow rather than on thermal radiation. Therefore, SWIR images are close representations of what is seen in the visible spectrum. Compared to thermal imagers, SWIR cameras also have a better dynamic range. Additionally, by using SWIR illumination for example 1550 nm LEDs or lasers, a scene can be covertly illuminated, i.e., viewing is only possible with a SWIR camera. Moreover, SWIR lasers are eye-safe, i.e., they can be used to safely illuminate targets and humans.

1.4.3.3 Laser gated imaging

Laser gated imaging allows for imaging at long distances while reducing the effect of obscurants in the atmosphere. In laser gated imaging, a pulsed laser is used to illuminate the scene, while the reflected light is detected by a camera with a short exposure or gating time. The exposure is delayed, so imaging occurs at a particular distance, thus the image is formed only from the reflection of objects at that distance. When using a SWIR camera, covert and eye-safe pulsed lasers can be used.

1.4.3.4 Situational awareness – gunshot detection

Conventionally, acoustic sensors that “listen” to the shockwave of a bullet are used for gunshot detection. However, gunshot signature can be identified, located and processed even faster using high-speed SWIR cameras, either at night or during daytime. The combustion gases and hot debris projected from the gun upon firing are detectable using SWIR cameras.

1.4.3.5 Seeing through haze, smoke and fog

Compared to visible cameras, SWIR cameras offer superior performance in imaging through dust, fog, haze or smoke. In case of fire, the location of the flames can easily be found.

1.4.3.6 Airborne reconnaissance, remote sensing and surveillance

Small, low-power and lightweight SWIR cameras can be used on airplanes and UAVs (unmanned air vehicles) for reconnaissance and surveillance missions. Hyperspectral SWIR cameras can be used to detect the unique spectral signature of militarily important items, for example camouflage material.

1.4.4 SWIR Detector Types

To serve these SWIR applications, a variety of detectors can be used, such as Germanium (Ge), Indium Gallium Arsenide (InGaAs), Indium Antimonide (InSb), and Mercury Cadmium Telluride (MCT or HgCdTe), Lead Sulfide (PbS) and Lead Selenium (PbSe) as shown in Figure 9. Also in Figure 9 the detectors that operate at SWIR and operate in room temperatures are marked with rectangles. Of these, InGaAs array detectors have proved to be the most practical for imaging applications due to their high normalized detectivity values, higher than 10^{12} Jones at room temperature operation. They also achieve high quantum efficiency and low dark current at room temperature, particularly for lattice matched InGaAs/InP detector structures operating in the 0.9 to 1.7 micron wavelength range [22].

Ge detectors are also used in SWIR applications. In cryo temperatures they achieve very high normalized detectivities; however, under ambient temperatures their normalized detectivities (D^*) are between 10^{10} and 10^{11} Jones ($\text{cm}\cdot\text{Hz}^{1/2}\cdot\text{W}^{-1}$). At ambient temperatures, PbS photodetectors are also been used in SWIR range with normalized detectivities similar to Ge detectors as seen in Figure 9. PbSe photodetectors; however, give poorer performance parameters at room temperatures in this spectrum such as; below 10^9 Jones.

Other detector types such as; InSb and MCT (HgCdTe) are also being used in SWIR spectrum. But usually, these detectors are operated in cryo temperatures in order to achieve high performance parameters.

1.5 Drawbacks of Current SWIR Detectors

The combination of visible and infrared detection provides a powerful tool that offers information extracted from the interaction of light of different wavelengths with

matter. Such functionality is of limited use today due to the high fabrication cost and modest performance of such photodetectors. Present-day multispectral image sensors that are composed of various semiconductor processes, which are not monolithically integrable, are required to be embedded on a single platform. Semiconductors are typically used to realize the optical detectors that convert incident photons to electronic charge carriers. These optical devices are characteristically grown on monocrystalline semiconductor substrates that are epitaxially grown or formed in a melt. Both the substrates and the additional deposition of lattice matched semiconductor material, introduce high costs and integration difficulties and thus limit the range of potential applications of the detectors.

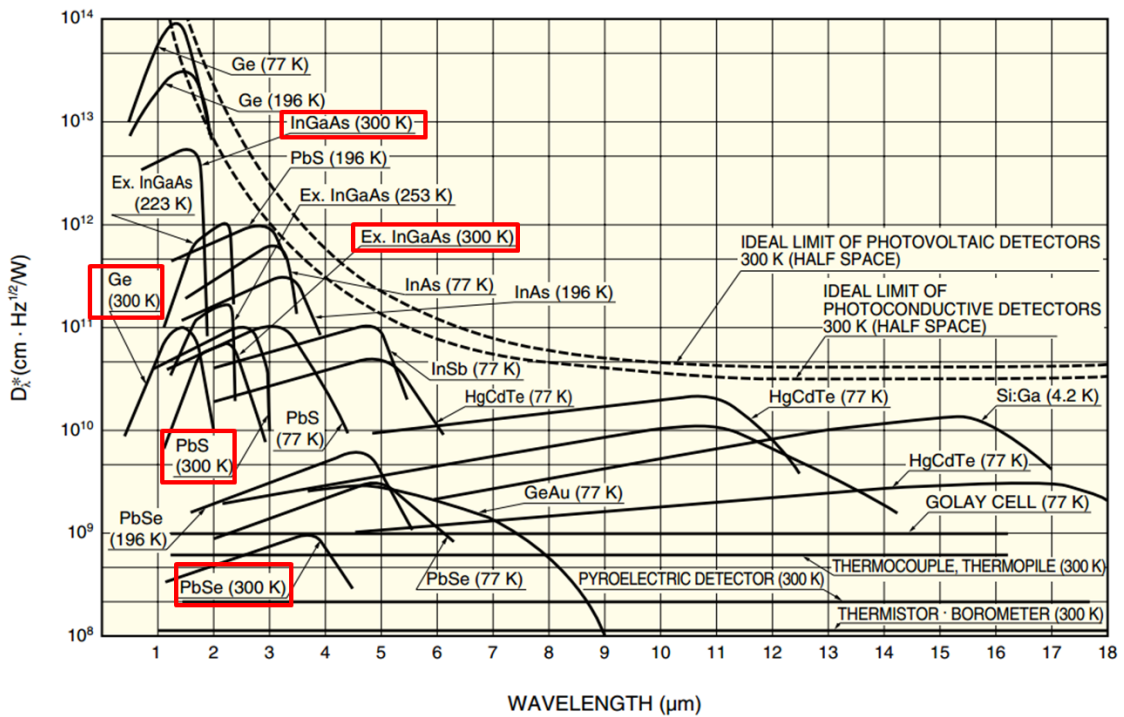


Figure 9. Various detectors used for infrared detection with their normalized detectivities and operating wavelength. Uncooled SWIR detectors are marked with rectangles [23].

The integration of the optoelectronic detection devices to the electronic charge carrier processing devices as closely as possible is desirable. This is because, the integration results in an increase in the density of the detectors, their operating speed and their overall sensitivity while reducing manufacturing costs associated with die-by-die hybrid integration, system size and weight and power consumption. Visible light can be detected by silicon which is widely used in microelectronics and this allows fully

integration of detectors with signal processing electronics. However bandgap of the Si is too wide to provide sensitivity to the IR. Commonly, narrow bandgap semiconductors are used in IR detectors such as; Ge, InSb, InGaAs, HgCdTe and leadsalts (PbS) [24]. The systems generated using these materials have been studied for a long time and demonstrate excellent performance; however, densely integrated signal processing electronics are not available in these materials. Silicon based signal processing electronics cannot be integrated with these photodetectors due to lattice matching requirements. This constraint prevents monolithic integration of IR detectors and as a result, IR detection systems composed of multiple substrates are connected with mechanical bonds to form a hybrid device. Hybrid integration decreases the operating speed due to the parasitics introduced by the mechanical bonds and decreases the number of photodetectors because of the size and spacing requirements for hybrid integration and thus, decreases the yield, reliability and increases cost. For instance, a typical focal plane array (FPA) of InGaAs on Si that has the spectral range of 900 to 1700 nm and that has a pixel count around 200000 costs a couple of thousands of dollars whereas, integrated Silicon FPA that works in visible range and that have millions of pixels costs around a couple of tens of dollars.

Solution-processed semiconductors are a promising alternative to inorganic semiconductor devices due to their low-cost and large-scale fabrication capability. These materials' growth, synthesis and processing take place while dispersed in a liquid medium and as a result the structural and electronic properties of solution processed semiconductors are independent of the substrate onto which they are ultimately deposited. In addition to that, bandgap of colloidal quantum dots can be tuned depending on their sizes and this provides optical absorption covering the ultraviolet, visible and infrared. For example, CQD absorption onsets have been demonstrated at wavelengths up to 2000 nm for PbS CQDs [25].

1.6 Thesis Objectives

In this thesis, it is aimed to design and implement low cost, high performance; colloidal quantum dots based photodetectors that is fully compatible for the direct integration onto the silicon read-out circuits. The goal is to achieve comparable performance parameters to InGaAs or HgCdTe counterparts in terms of responsivity

and detectivity and present an alternative to them especially for the applications where there are cost constraints. In order to implement directly on the IC ROICs, the process steps will be designed to be IC compatible.

Up to now in the literature the PbS CQD based photodiodes is mainly fabricated on ITO coated glass samples. In this work it is also aimed to fabricate them on silicon substrates and also mimics of the ROICs. In terms of integration, it is crucial to realize them in this manner, because monolithic integration is the most important advantage of solution based photodetectors.

Creating PbS CQD photodetectors on Si substrates or on ROIC chips entails successful deposition of transparent conductive layers which will form the top layer of the device where the incident light is transmitted into the PbS layer. So it is also aimed in this thesis to study sputter deposition of high quality transparent conductive layers on PbS CQD films.

Another aim of this thesis is to implement metal nanoparticles for plasmonic scattering in PbS CQD films in order to improve the absorption characteristics. In PbS CQD photoconductors thick films are required to fully absorb the incident light; however, having thicker films presents a bottleneck in achieving efficient carrier extraction. In order to overcome this bottleneck plasmonic scattering will be used to enhance absorbance in thin films. Conventional method in PbS CQD photoconductors is to create metal nanoparticle islands under the PbS CQD film, however, this required high temperature annealing. Thinking of IC integration, annealing temperatures presents a bottleneck for integration. In this work, it is aimed to implement plasmonic scattering using solution based metal nanoparticles. Metal nanoparticles will be applied into PbS CQD films by spin coating them in the middle of spin coating steps of PbS CQD film formation. This process will be fully IC compatible.

1.7 Thesis Overview

The overall work in this thesis is divided into three main chapters. In line with the aim of realizing IC compatible high performance and low cost PbS CQD based photodetectors, the work is started with building the PbS CQD based photodiodes on glass samples using different schottky metal contacts which is described in Chapter 2.

After optimizing the PbS CQD film deposition and ligand exchange procedures in PbS CQD photodiodes on glass samples, and after achieving good performance parameters, these photodiode structures are realized; first on the Si samples, and second on the mimic of ROIC in order to demonstrate the monolithic integration of these structures on the ROICs. And this forms the Chapter 4. Lastly, in Chapter 5, the effect of plasmonic scattering using metal nanoparticles on absorbance and responsivity in PbS CQD films is studied. In this part, unlike the other two chapters, photoconductor topology is used because of its simplicity. The detail of each chapter is given below in more detail.

The thesis begins with introduction of the IR detection applications, describing the IR market roadmap, and IR applications. Also the importance of SWIR detection presented and also currently used SWIR detector types are listed. Also the drawbacks of current SWIR detectors are presented.

In Chapter 2, colloidal quantum dot photodetectors is presented. The principles of colloidal quantum dots together with synthesis are given in this chapter. Two different types of photodetection mechanisms employed in CQD photodetectors; photoconductivity and photovoltaic response, are reviewed. Also the sources of noise that limit photodetector and the performance parameters of photodetectors are explained in this chapter. Lastly, a review of CQD photodetectors is presented in this chapter. Chapter 3 presents the design and implementation of PbS CQD schottky photodiodes on glass substrates. This chapter presents the baseline for this thesis work. The principles of implementing a schottky diode using PbS CQDs are given. The implementation of PbS CQD photodiodes is given in detail in terms of PBS layer formation, surface modification and schottky metal deposition. Ligand exchange procedure is also given in this chapter. The spin coating and ligand exchange procedures given in this chapter is used for all the processes in this thesis. Two types of schottky photodiodes are presented in this chapter one with Al schottky contact and one with Ti/Au schottky contact. Measurement setup is presented together with measurement results of these photodiodes.

In Chapter 4, realization of IC integrable PbS CQD Photodetectors are given. The possible-read out integration is presented and PbS CQD schottky photodiodes are designed in this manner. Also top layer of a typical ROIC chip is mimicked on Si substrates and PbS CQD diodes are realized on these mimic substrates. Fabrication

steps of this process are given in detail. Also the measurement setup and the test results are presented. It has been observed; the detectors achieve lower noise than the versions that are built on glass substrates. However, the rectification performance of the diodes decreased especially in the ones that are built on chip mimics. It has been observed that they act more like photoconductors.

Chapter 5 presents the application of plasmonics in PbS CQD Photoconductors in order to increase the absorption and hence the responsivity of photoconductors. PbS CQD photoconductors is implemented on Si substrates and details are given in this chapter. In addition to that solution based metal nanoparticles is applied in PbS CQD films with different concentrations and these versions are also tested and compared with reference photoconductors. Up to 6 fold responsivity increase is demonstrated by test results.

Chapter 6 summarizes the work done in this thesis in terms of CQD photodetector performances and CQD materials and device. The chapter concludes with recommendations for future work in the development of this very promising class of solution-processed optoelectronic device.

Chapter 2

COLLOIDAL QUANTUM DOT PHOTODETECTORS

2.1 Colloidal Quantum Dots

Nanocrystal quantum dots are the semiconductor particles with radii less than 10 nm. Nanocrystals preserve the crystal structure of the bulk material they are composed, yet, they have the characteristic of confining charge carrier motion in three dimensions. Semiconductor CQDs composed of very small crystals of semiconductor material surrounded by a layer of organic ligands that are chemically bonded to the surface of the crystal, providing electronic and chemical passivation of dangling bonds and solubility in polar or non-polar solvents, determined by the ligand species.

The most crucial property of these quantum dots are the quantum confinement phenomena. If the size of the semiconducting crystal is reduced to the point where the electron and/or hole wave functions begin to be squeezed into a region smaller than their characteristic Bohr radius, their allowed Eigen energies increase in energy from that of bulk. Bohr radius (r_b) is defined as,

$$r_b = \varepsilon \frac{m}{m^*} r_{hydrogen} \quad (2.1)$$

where ε is the dielectric constant of the material, $r_{hydrogen}$ is the Bohr radius of the hydrogen atom, m is the mass and m^* is the effective mass of the excited particle [26]. A first order approximation to the size-quantized electronic properties of a semiconductor quantum dot is provided by the particle-in-a-sphere model in which QD is modeled as a small sphere of semiconducting material and the perfect insulator surrounding it. The particle-in-a-sphere model predicts an inverse-squared dependence of quantum dot bandgap, $E_{g,QD}$ on the radius of the nanocrystal, R [26],

$$E_{g,QD} = E_g + \frac{\hbar^2 \pi^2}{2R^2} \left[\frac{1}{m_e^*} + \frac{1}{m_h^*} \right] \quad (2.2)$$

where E_g is the bulk semiconductor bandgap, \hbar is reduced Planck constant and m_e^* and m_h^* are the effective masses of electrons and holes in lattice, respectively. Thus, decreasing quantum dot size leads to an increase in bandgap and a shift of photon absorption and emission maxima towards shorter wavelengths, compared to the bulk semiconductor material.

The bandgap of a nanocrystal begins with that of bulk material and subsequently shifts up in energy; certain semiconductors are more suitable to specific applications than others. For instance, CdSe and CdS can be tuned across the entire visible spectrum by varying the bandgap energy from 1.8 eV to 3.1 eV (corresponding to a shift from 400 nm to 700 nm), a dramatic change considering the bulk bandgap energy of CdSe is 1.73 eV [27]. On the other hand PbS has a bulk bandgap of 0.41 eV (3100 nm) and can be tuned across the spectral region of 800-2000 nm. This makes it suitable for near-IR emitters, detectors, modulators and photovoltaics [28]. Figure 10 shows the adsorption spectrum shift of PbS quantum dots due to the size tuning of them during their synthesis.

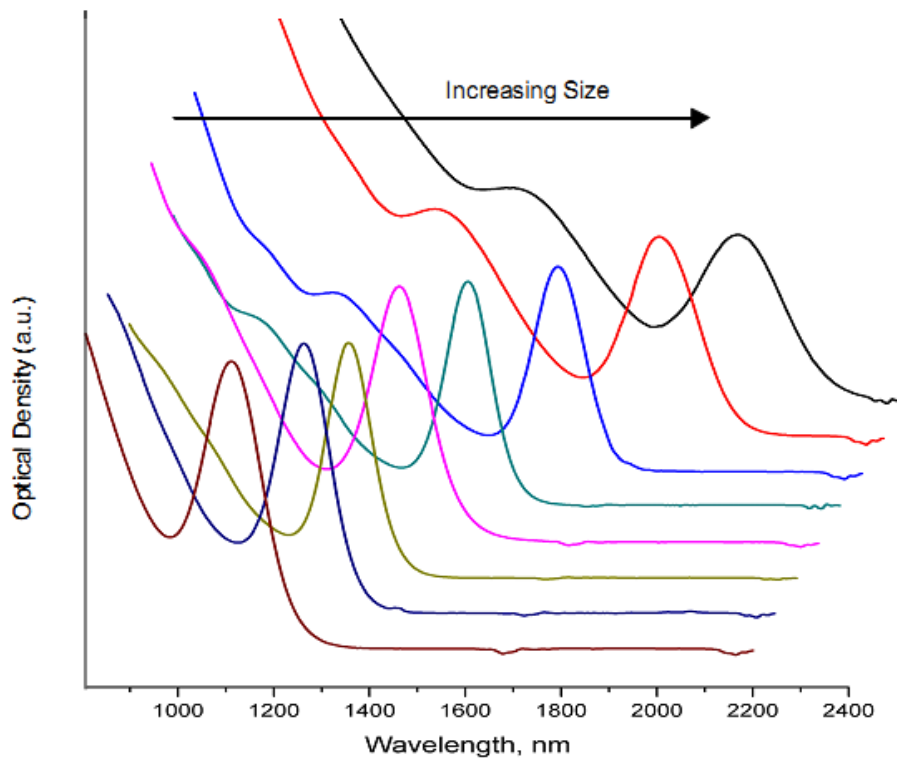


Figure 10. The absorption spectrum of PbS for a range of QD sizes [29]

2.2 Synthesis of Colloidal Quantum Dots

Conventional way of synthesis of colloidal quantum dots entails pyrolysis of metal-organic precursors in hot coordinating solvents of temperatures in the range of 120 - 360 °C. The process is very straightforward and carried out in a three necked flask on a temperature controlled hot plate and inert atmosphere as shown in Figure 11.

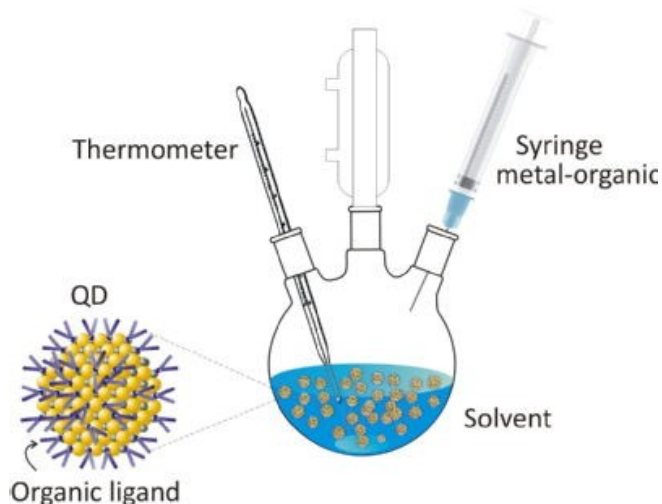


Figure 11. Setup for colloidal quantum dot synthesis

Typically, one precursor is mixed with the coordinating solvent and held at steady temperature. Then the other precursor is injected into this mixture resulting in spontaneous nucleation. Nucleation results from the thermal decomposition of the precursor agents upon injection and supersaturation of monomers that form the building blocks of the CQDs as shown in Figure 12 stage 1. Nucleation is followed by relatively rapid growth of the crystalline semiconductor cores of CQDs (Figure 12 stage 2). Growth may be followed by slower Ostwald ripening (sacrificial dissolution of smaller, higher-surface-energy particles to enable the growth of larger particles) after one or more of the precursors are exhausted (Figure 12, stage 3). The synthesis reaction may take anywhere between several seconds up to several hours to reach completion, depending on the materials involved.

The synthesis monomers shown in Figure 12, stage 1 include metallic atoms bound to one or more molecules of the coordinating solvent (balls with tails in the figure), and the second component of the compound semiconductor, which may or may not be bound to a coordinating solvent (balls without tails in the figure). When attached

to a semiconductor atom, the coordinating solvent acts as a ligand, providing solubility and controlling the rate of monomer interaction and CQD growth. After nucleation, the CQD cores are surrounded by a ligand layer that provides solubility and prevents individual CQDs from aggregating during or after synthesis.

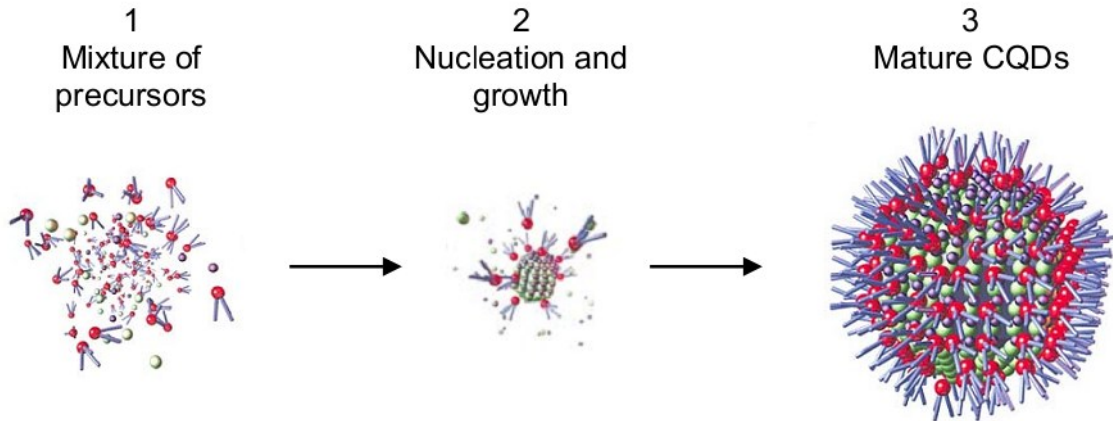


Figure 12. A schematic representation of the organometallic CQD growth process. Synthesis results in inorganic crystalline semiconductor cores surrounded by organic ligands that passivate the crystal surface, as shown in the final step of the growth process [30].

2.3 CQD Based Photodetectors

Photodetectors are typically classified depending on their detection mechanisms which is either thermal detection that absorb radiation and measure the change in the physical properties of the detector material in response to a change in temperature or photon detection. Most commonly used photon detection techniques include photovoltaic and photoconductive mechanisms and these mechanisms based on the generation of free carriers within semiconductor materials by absorption of photons with energies equal to or greater than the semiconductor bandgap. CQD photodetector development mainly centers on photovoltaic and photoconductive mechanisms where spectral tuning of the detector is accomplished through semiconductor type selection and quantum size effect control of bandgap energy.

The photovoltaic and photoconductive photon detection mechanisms are based on the generation of free carriers within semiconductor materials by absorption of photons with energies, E_{photon} , equal to or greater than the semiconductor bandgap, E_g ,

$$E_{\text{photon}} = \frac{hc}{\lambda_p} \geq E_g \quad (2.3)$$

where h is the Planck constant and c is the speed of the light. This minimum energy corresponds to the detector absorption cutoff wavelength, λ_p [14].

2.3.1 Photodiode Detectors

Photovoltaic detectors based on the measuring the generated potential across a metallurgical junction, in result of incident optical radiation. Generally photodiodes rely on the use of two media, at least one of them being a semiconductor, and the difference between the work functions of these two media creates a built in potential. This built in potential used to separate excess electrons and holes generated through the absorption of the light by the semiconductor. The energy levels within the device are such that the extraction of photogenerated charge may be driven entirely through diffusion, not requiring an external voltage bias for operation; however, applying a reverse bias across the diode structure can result in increased charge collection efficiency. The response speed of a photodiode is determined by the time required for photogenerated carriers to be transported to the contacts and this time should be less than the carrier lifetimes in order to maintain high quantum efficiency. Photodiodes are commonly operated in a current sensing (short circuit) mode providing a linear current response to illumination and providing detector impedance independent of the photon flux.

The current-voltage, I-V, characteristic of a photovoltaic detector,

$$i = i_{\text{dark}} + i_{\text{photo}} \quad (2.4)$$

is a combination of the un-illuminated I-V characteristic of the junction, i_{dark} ,

$$i_{\text{dark}} = i_o(e^{qV/\beta k_B T} - 1) \quad (2.5)$$

represented by the diode equation, and the photogenerated current, i_{photo} . In the diode equation, i_o is the saturation current density, q is the electronic charge, V is the potential drop across the junction, k_B is Boltzmann's constant, T is the temperature and β is the ideality factor changes between 1 to 2 depending on the fabrication process and semiconductor material. The photogenerated current,

$$i_{photo} = q\eta\phi \quad (2.6)$$

is a linear function of the quantum efficiency of the detector, η , and the photon flux, ϕ and the electron charge, q [14].

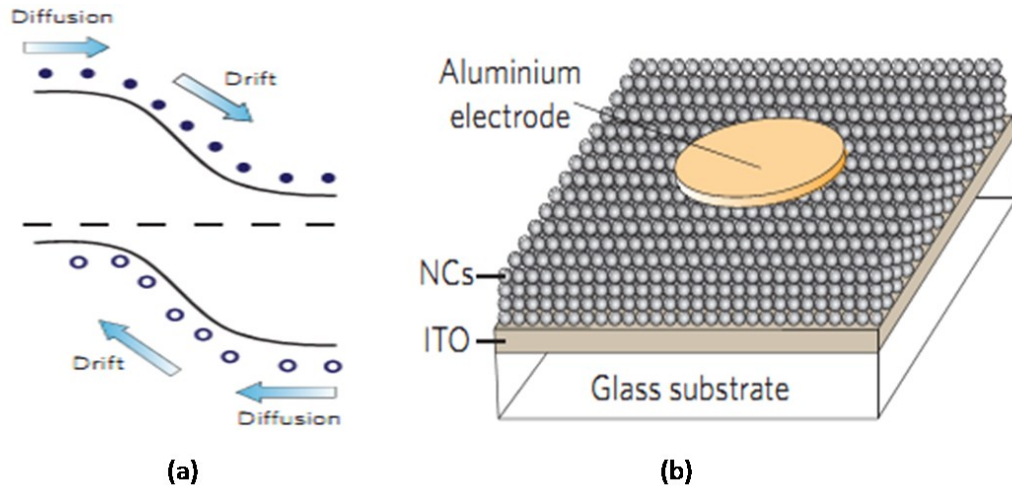


Figure 13. a) Spatial band diagram of photodiode b) The structure of CQD photodiode [31]

In typical CQD photodiode, a thin film of CQDs is contacted ohmically on one side via a transparent conductive oxide (TCO) and on the other side using a shallow work function metal at which a significant built-in potential is established relative to the (natively p-type) CQD film. Indium tin oxide (ITO) is typically used as the ohmic TCO, while aluminum and magnesium have been widely used as the shallow work function metal. Figure 13 shows the device architecture along with a corresponding spatial band diagram. Drift and diffusion of both electrons and holes are exploited in photodiodes, in which electron–hole pairs are separated by the action of a built-in electric field represented by the spatial bending of the bands. Upon light absorption, the energy of the photon is transferred to an electron (filled circles) in the semiconductor, elevating it to the conduction band (upper black line) and leaving behind a hole (open circles) in the valence band (lower black line). This spatial band diagram depicts the junction between a p-type (hole-rich, left side) and n-type (electron-rich, right side) semiconductor near equilibrium. In this p–n junction diode, the dashed line represents the Fermi level.

2.3.2 Photoconductive Detectors

In photoconductive detectors, the incident optical radiation increase the number of the free carriers available to transport current and this proportionally change the conductivity of the detector, $\Delta\sigma$.

$$\Delta\sigma = q\Delta N\mu \quad (2.7)$$

where q is the electron charge, μ is the mobility of free carriers and ΔN is the net change in the carrier concentration, ΔN , depends on the carrier lifetime and strongly influenced by the presence of traps in the semiconductor [14]. The current response of the photoconductive carrier is very similar to the photodiode with an additional gain factor as seen in equation 2.8 [14].

$$i_{photo} = q\eta\phi G \quad (2.8)$$

where q is the electron charge, η is the quantum efficiency of the detector, ϕ is the photon flux.

For photoconductive devices with ohmic contacts, response time is determined by the lifetime of the photogenerated carriers. In these devices, photogenerated carriers are swept out of the device by the electric field, and are replenished at the opposite side of the device by an efficient injecting contact. This results in the possibility of more than one charge carrier traversing the device for a single carrier generation event resulting photoconductive gain, which is a function of the electric field in the semiconductor and increases with bias as seen in equation 2.9, where E is the electric field in the semiconductor, μ is the mobility of free carriers, t_1 is the carrier lifetime and d is the distance between the electrical contacts [14].

$$G = \frac{\mu Et_1}{d} \quad (2.9)$$

A typical CQD photoconductor employ coplanar electrodes coated with a continuous film of nanocrystals as seen in Figure 14 (b). The realization of these devices is greatly simplified by the simple spin casting of a quantum dot film atop electrodes prefabricated on a substrate. The current flow direction is primarily within the horizontal plane. The distance photocarriers must travel — and thus their transit time,

relevant to gain — is determined by the contact separation. In a photoconductor, one type of carrier is trapped while the other circulates under the influence of an electric field as seen in Figure 14 (b), and electrons are trapped in this depiction. Red arrows depict the capture of electrons from the conduction band into associated trap states. If the hole lifetime exceeds the time it takes for the hole to transit the device, then the long lifetime of the trapped electrons ensures that holes can circulate through an external circuit many times, resulting in gain.

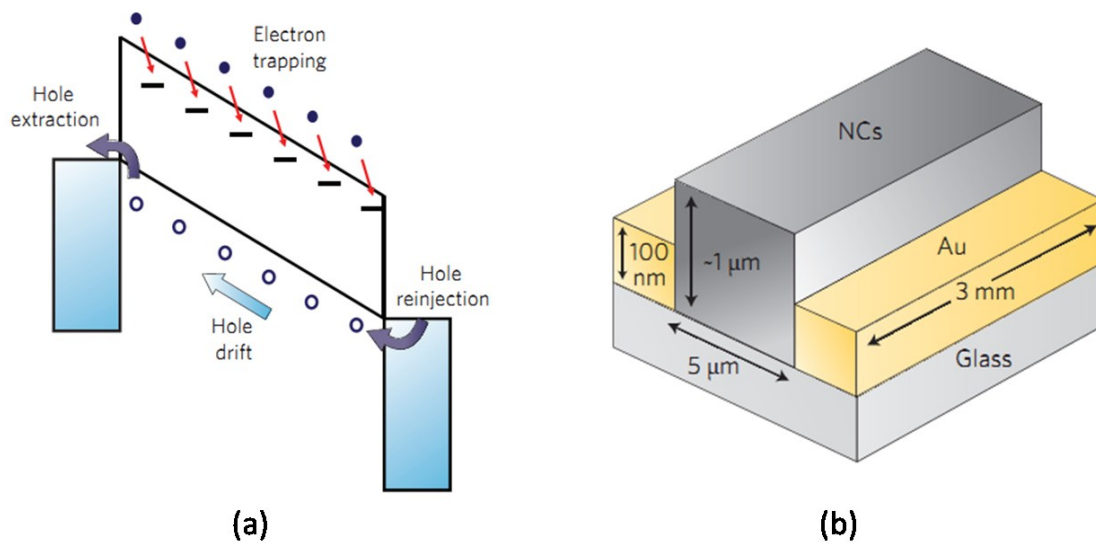


Figure 14. a) Spatial band diagram of photoconductor b) The structure of CQD photodiode [31]

2.4 Noise Sources

The photon noise in the signal and background illumination and electrical noise generated in the detectors are the noise sources that define the limitations of the resolution and sensitivity of a detector. Detector architecture and operating conditions are important in terms of noise performance. That is because, the total noise is cumulative and different noise components can add to total noise depending on the photodetector architecture and operating conditions.

2.4.1 Photon noise

The lowest detectable limit in optical detection is defined by photon noise independent of any detector properties. Photons are discrete entities that obey Poisson

statistics. The instantaneous rate of photon emission from a source varies with time, resulting in a distribution of photon arrivals at a detector. The standard deviation of a Poisson distribution, σ ,

$$\sigma = \sqrt{n} \quad (2.10)$$

is equal to the square root of the mean, n , of the distribution. As these photons are detected, the variation in the arrival rate is translated into a variation in the output signal of the detector.

Photons originate from two sources, the signal and any background illumination. A well designed detection system maximizes the ratio of signal to background illumination incident on the detector. When working in the IR, detectors may be sensitive to background photons emitted by objects acting as blackbody sources. The ability to cutoff detector sensitivity to longer wavelength photons is critical for limiting this sensitivity, especially when working at or near room temperature.

2.4.2 Detector noise

The principal noise sources within photovoltaic and photoconductive detectors are thermal noise, shot noise, 1/f noise, and generation-recombination noise. These noise sources can be treated as voltage or current sources in the detector circuit model. In the context of photoconductors and photovoltaic detectors operated in short circuit mode, it is convenient to work with noise currents.

2.4.2.1 Thermal noise

Thermal noise, also known as Johnson noise or Nyquist noise, originates from the thermal motion of charge carriers in a resistive element. It is an intrinsic noise source found in all materials. Thermal noise current, i_t ,

$$i_t = \sqrt{\frac{4k_B T \Delta f}{R_o}} \quad (2.11)$$

where R_o is effective shunt resistance of the device, T is the temperature, Δf is the operating bandwidth and k_B is the Boltzmann's constant [24].

2.4.2.2 Shot noise

Shot noise originates with the discrete nature of charge carrier emission over a potential barrier, similar to the emission of photons from an optical source. Shot noise is present only in devices with a potential barrier, such as photodiodes, and is associated with both the photocurrent and dark current of the device. Shot noise is equivalent to the standard deviation of a Poisson distribution representing the arrival of the charge carriers. Shot noise current, i_s ,

$$i_s = \sqrt{2qi\Delta f} \quad (2.12)$$

where q is the electron charge, i is the mean current including dark current and photogenerated current, and Δf is the noise measurement bandwidth. Shot noise is the dominating source when operating in photoconductive (biased) mode [24].

2.4.2.3 1/f noise

1/f noise is the least understood noise source, but is commonly encountered in detectors at low frequencies (<1 kHz). The source of this noise has been attributed to non-ohmic contacts and variation in the time constants of charge carrier traps that interrupt current flow in semiconductors. 1/f noise current, i_f ,

$$i_f \propto \sqrt{\frac{i^2 df}{f^{-1}}} \quad (2.13)$$

is proportional to the mean dc current, i , and inversely proportional to the square root of the operating frequency, f [24]. The exact dependence on frequency varies between devices and is determined empirically.

2.4.2.4 Generation-recombination noise

Generation-recombination noise results from statistical fluctuation in free charge carrier generation and recombination rates. These variations in these rates are attributable to the distribution of carrier lifetimes and variation in the generation processes. Generation-recombination noise current, i_{gr} ,

$$i_{gr} = 2qG\sqrt{\eta\phi A\Delta f + g_{th}A\Delta f} \quad (2.14)$$

is proportional to the electron charge, q , optoelectronic gain, G , quantum efficiency, η , photo flux, ϕ area, A , operating bandwidth, Δf , thermal generation rate, g_{th} , and thickness of the detector, d [24]. In the case of photoconductors, the photon generation rate is typically larger than the thermal generation rate, and its variation is tied to photon noise. The relative contribution of generation-recombination noise in photo conductors can be very large, as it is the only noise source dependent on the gain of the device.

2.4.2.5 Total noise

The total noise observed at the output of the detector is the sum of the power of the individual noise sources. As such, noise current sources add in quadrature,

$$i_{noise} = \sqrt{i_t^2 + i_s^2 + i_f^2 + i_{gr}^2 + \dots} \quad (2.15)$$

The relative contribution of each of these noise sources depends on the detector architecture and operating conditions. In the absence of illumination or applied bias, at very low frequencies, $1/f$ noise dominates the electrical noise of photovoltaic and photoconductive detectors. In photoconductors, with increasing frequency, GR noise becomes dominant until, finally, only thermal noise is present [32]. In photovoltaic detectors, current noise at frequencies above the $1/f$ knee originates entirely from thermal noise [33], as excess noise in the absence of an external current or illumination source violates thermodynamic principles [34]. Application of a bias introduces dark current shot noise and moves the $1/f$ knee to higher frequencies. In photodiodes under bias, shot noise, rather than thermal noise, defines the frequency-independent background noise intensity at higher frequencies [33].

2.5 Photodetector Performance Parameters

2.5.1 Dark Current (I_d)

The dark current is a small current which flows when a reverse voltage is applied to a photodiode even in the dark state. This is a major source of noise for applications in which a reverse voltage is applied to photodiodes.

2.5.2 Responsivity (R)

Responsivity is the ratio of the generated photocurrent in a photodetector to the incident optical power. For photodetectors operated in a current sensing mode, responsivity, R , is the output current, i_{out} , per watt of optical input power, P_{in} ,

$$R_i(\lambda, f) = \frac{i_{out}(\lambda, f)}{P_{in}} \quad (2.16)$$

in units of $A \cdot W^{-1}$ [23]. Responsivity in photon detectors is inherently a function of the wavelength of the incident optical power, λ . Responsivity is also a function of the frequency of the illumination, as the frequency response of a photodetector is finite. In addition to that, responsivity increases slightly with applied reverse bias due to improved charge collection efficiency in photodiode. Also there are responsivity variations due to change in temperature.

2.5.3 Quantum Efficiency (QE)

Quantum efficiency is defined as the percentage of the incident photons that contribute to photocurrent. It is related to responsivity by:

$$Q.E. = \frac{R_{Observed}}{R_{Ideal(100\%)}} = R \frac{hc}{\lambda q} = 1.24 \times 10^3 \frac{R}{\lambda} \quad (2.17)$$

where h is the Planck constant, c is the speed of light, q is the electron charge, R is the responsivity in A/W and λ is the wavelength in nm. Quantum efficiency is commonly expressed in percent (%) [23].

2.5.4 Noise Equivalent Power (NEP)

Noise equivalent power is the amount of incident light power on a photodetector, which generates a photocurrent equal to the noise current. Stated differently, it is the light level required to obtain signal-to-noise ratio of unity. NEP is defined as [23];

$$NEP [W/\sqrt{Hz}] = \frac{\text{Noise current } [A/\sqrt{Hz}]}{\text{Photo sensitivity at } \lambda_p [A/W]} \quad (2.18)$$

Since the noise level is proportional to the square root of the frequency bandwidth, the NEP is measured at a bandwidth of 1 Hz. Sensitivity, in terms of NEP,

is dependent on detector geometry and operating conditions, and is not suitable for comparing dissimilar detectors.

2.5.5 Detectivity (D^*)

D , which is the reciprocal of NEP, is the value used to indicate detectivity, or detection capacity. However, because the noise level is normally proportional to the square root of the sensitive area, NEP and D characteristics have improved, enabling detection of even small photo-sensitive elements. This makes it possible to observe the characteristics of materials by multiplying the square root of the sensitive area and D , with the result being used as D^* [23].

$$D^* = \frac{\sqrt{A\Delta f}}{NEP} \quad (2.19)$$

Detectivity is in units of Jones ($cm \cdot \sqrt{Hz} \cdot W^{-1}$), and allows direct comparison of detectors with different active areas, A , and operating bandwidths, Δf .

2.6 CQD Photodetectors Previous Works

There have been many works reported on colloidal quantum dot based photodetectors in last decade and significant advances have been achieved. Table 1 summarizes the published work on solution based photodetectors with published year, performance parameters, the materials used as well as remarkable points of the work.

The results in Table 1 fall into two performance classes, one corresponding to photodiodes and the other corresponding to photoconductors. In a photodiode, the electrons and holes generated by the incoming photons move to opposite electrical contact, so the quantum efficiency of such devices cannot be higher than one (unless effects such as avalanche or carrier multiplication are exploited). However, photodiodes can have fast response times, shorter than electron–hole recombination times, which are typically microseconds or less for the direct-gap semiconductors commonly used. Photodiodes thus populate the higher-frequency reaches of Table 1. Photoconductors, on the other hand, are capable of high gain because one type of charge carrier is able to circulate through an external circuit many times before it recombines with its opposite carrier, which meanwhile remain trapped in the photoconductor bulk. Table 1 lists a

number of photoconductors with responsivity values in the range of 100 – 1,000 A W⁻¹, corresponding to gains of 100–1,000. Although these high gains increase responsivity and simplify the job of any photo-detector read-out circuits, they also reduce the bandwidth because of the long circulating carrier lifetimes involved. The performance of a photodetector can be improved, not only by maximizing its electrical response to light, but also by minimizing the noise in its electrical output, which can obscure real signals. One way to compare detector sensitivities is therefore to examine the signal-to-noise level at a given illumination intensity. Or, conversely, one can examine the noise-equivalent power, which reports the optical power at which the signal-to-noise ratio (SNR) is one (or 0 dB). This noise level is very low, corresponding in some photodetectors to single-photon detection per integration period. The detectivity D* (formally defined in Table 1, and measured in units called Jones) seeks to normalize for variations in device area and speed of response, thus providing a figure of merit that enables comparison among different devices. Table 1 shows that the best solution-processed detectors have achieved D* values of up to 5×10^{13} , which is comparable to the best values reported for single-crystal photodiodes. This a remarkable achievement because single-crystal photodiodes have benefited from several decades of engineering, including both materials purification and device structure optimization, whereas solution-processed detectors have reached similar levels of performance after just three years of development.

Table 1. Solution based photodetector review

Year	λ (nm)	EQE(%) or R(AW ⁻¹)	D* meas (Jones)	D*inf. (Jones)	3dB BW (Hz)	Mech anism	Material	Features
2005 [35]	400- 700	0.2 %		10 ⁸	5x10 ⁴	PD	CdSe quantum dots	Early quantum- photodiode
2006 [36]	Vis- 1300	2700 AW ⁻¹	2x10 ¹³	5x10 ¹³	2x10 ¹	PC	PbS QD	Record sensitivity, pure QD device.
2007 [37]	Vis- 850	120 AW ⁻¹	5x10 ¹²	3x10 ¹³	2x10 ¹	PC	PbS QD	Visible only device using ultraconfined dots
2007 [38]	Vis- 3000	4.4 AW ⁻¹	3x10 ¹⁰		10 ¹	PC	HgTe QD	Long wavelength operation
2008 [39]	350- 650	50 AW ⁻¹		5x10 ¹²		PC	P3HT+PCB M+CdTe quantum dots	Sensitive heterojunction device
2008 [40]	Vis- 850	10 AW ⁻¹		1.3x10 ¹³	5x10 ¹	PC	PbS QD	High- uniformity device
2008 [41]	Vis- 850	12 AW ⁻¹	10 ¹²		3x10 ¹	PC	PbS CQ	Single-trap time constant
2009 [42]	50- 930	18 AW ⁻¹		1.5x10 ¹⁴	3x10 ¹	PC	PbS CQ	Multi excition generation enhanced
2009 [43]	Vis- 1600	0.2AW ⁻¹	10 ¹²		10 ⁶	PD	PbS QD	Megahertz response in fully depleted photodiode
2009 [44]	Vis- 1800	51%	2x10 ⁹		2x10 ³	PD	PbS QD +PCBM + P3HT	Integrated into an image array
2009 [45]	Vis- 1450	20%		10 ¹² NIR 10 ¹³ VIS		PD	PDDTT + PCBM	Long- wavelength polymer photodetector
2010 [46]	250 – 2000 nm	24%und er PV op				PD	PbS QD – C60 Heterojuncti on	Heterojunction with C60
2011 [47]	Up to 1300 nm	23% 430nm 7% 610nm		4.7x10 ⁹		PD	P3HT:Pbs QD:PCBM blend	Pb QDs with polymer blend
2011 [48]	600- 1400 nm	1 AW ⁻¹	1x10 ¹²			PD	TFB+PbSe CQ + ZnO NC	Better dark current perf. With blocking layers

Chapter 3

PBS CQD PHOTODIODES

The photogenerated charge carriers have to be efficiently transferred on length scales comparable to the absorption length of light in the semiconductor material in order to achieve sensitive photodiodes. As a result of this efficient transfer largest possible portion of the incident photons is absorbed and converted into charge carriers and collected at the electrical contacts before the photogenerated electrons and holes recombine. Also a large built-in potential is required for highly-sensitive photodiodes for efficient charge carrier separation and suppression of noise that would otherwise limit sensitivity. Achieving these requirements requires a semiconductor material with high conductivity (via high mobility) and sufficient passivation for forming metallurgical junctions with minimal interfacial effects. Any other materials used to form the metallurgical junction must be chemically and structurally compatible with this semiconductor material in order to minimize interfacial effects

A fundamental advantage of inorganic-organic hybrid CQD materials is the ability to adjust the macroscopic electronic properties of films through CQD surface modification. CQD films offer a number of chemically-tunable degrees of freedom linked to the organic molecules used to passivate their surfaces and the degree of oxidation of the CQD surface. The spacing between individual CQDs is controlled by the length of the organic ligands used to passivate their surfaces. This is a determining factor in the conductivity of CQD films: inter-dot spacing controls the likelihood of individual charge carriers moving between adjacent CQDs, in turn determining their overall mobility.

The consistency of surface passivation is also important, as this limits oxidation and other chemical modification of the CQD surface. Oxidation provides a route to effectively dope a CQD film; however, uncontrolled variation in the CQD surface leads to interface states and a reduction of the built-in potential when forming metallurgical junctions. In diodes, the energetic barrier associated with the metallurgical junction

defines the effective shunt resistance (R_o), which, in turn, determines noise performance. Thus, this interfacial control is essential for fabricating high sensitivity photodiodes. In sum, control over sensitivity and speed of the photodiode derives directly from engineering of CQD film properties.

In this chapter, PbS colloidal quantum dots is studied to be used in photodiode structure. The optimization of PbS quantum dot film formation, ligand exchange procedure, schottky contact formation is carried out using the basic schottky photodiode structure.

3.1 Photodiode Topography Selection

Response time in photoconductor is limited by carrier lifetime whereas in photodiodes, it is limited by the carrier transport time. Long lived minority carrier traps which is essential to photoconduction, lead to slow photoresponse speeds in photoconductors. Because of that, respond speed of photodiodes to the illumination is generally higher than photoconductors. Higher respond speed to illumination makes photodiodes more suitable to imaging applications. In addition to that, photodiodes achieve lower dark currents, high impedance and low power dissipation comparing to photoconductors which makes them more suitable for integration with read out circuits.

Photodiodes provide an additional degree of freedom in device design compared to photoconductive detectors. In photovoltaic detectors; semiconductor material properties and the properties of metallurgical junction that provides the built-in potential for carrier separation play an important role on photoresponse. Together modifying chemical and physical properties of the semiconductor for photoresponse optimization, as conventionally applied in photoconductor architecture, modification in device architecture and physical design of the detector in photovoltaic detectors can enable better performance parameters.

Doped homojunctions, heterojunctions and schottky barriers are typical methods to form metallurgical junctions in semiconductor photodiodes. The p-n junction is a commonly used homojunction implemented in a single type of semiconductor by having electron rich and hole rich regions. When in contact with each other, a depletion region and a built in voltage occurs. There is a trade-off between junction width and built-in

potential of the junction in photodiodes fabricated from p-n junctions; such that, low doping levels are required to provide a wide junction for efficient photocarrier capture but low doping levels limit the built-in potential of the junction. Doping of bulk semiconductor crystals are very well established and widely used in many applications; however, in colloidal nanocrystals, it remains a challenge to introduce impurities and control the doping [49].

Heterojunction is an alternative method to form a p-n junction using two dissimilar types of CQDs. This type of junction is easier to implement in nanocrystals than bulk crystals, since in nanocrystals, no lattice matching requirements must be met. However, a heterojunctions would require the development and optimization of two types of colloidal quantum dot films. There are suitable counterparts to PbS nanocrystals such as PbSe and PbTe, yet still studies on film morphology, carrier mobility and effective doping is required to form heterojunctions between these two type of nanocrystals [50].

In Schottky barrier type metallurgical junction, a junction is formed between metal and the semiconductor as a result of the work function difference between them. A Schottky barrier to a semiconductor film requires the development of only a single semiconductor material; however, it is more sensitive to effects of interface states which can significantly alter the energy band alignment at the metallurgical junction. Compared to p-n junction diodes, Schottky barrier diodes can have higher saturation currents, resulting in lower impedance and higher dark current. However, Schottky barrier devices have higher response speed than p-n junction diodes as they are not limited by diffusion capacitance resulting from minority carrier transport in the neutral regions of the device.

Schottky barrier diodes are selected in this work to be used as SWIR infrared photodetectors due to their higher response speeds and their ease of implementation for colloidal quantum dot nanocrystals.

3.2 Colloidal Quantum Dot Schottky Photodiode Structure

3.2.1 PbS Colloidal Quantum Dots

In this work, it is aimed to realize a photodiode using colloidal quantum dots that is sensitive in SWIR spectrum. As mentioned before, the bandgap of a nanocrystal can be tuned as a result of quantum confinement principle. The bandgap of a nanocrystal begins with that of bulk material and subsequently shifts up in energy. Most commonly used nanocrystals in colloidal quantum dot photodetectors are CdSe, CdS, PbSe, PbS and HgTe. Certain semiconductors are more suitable to specific applications than others. For instance, CdSe and CdS can be tuned across the entire visible spectrum by varying the bandgap energy from 1.8 eV to 3.1 eV (corresponding to a shift from 400 nm to 700 nm). On the other hand PbS has a bulk bandgap of 0.41 eV (3100 nm) and can be tuned across the spectral region of 800-2000 nm.

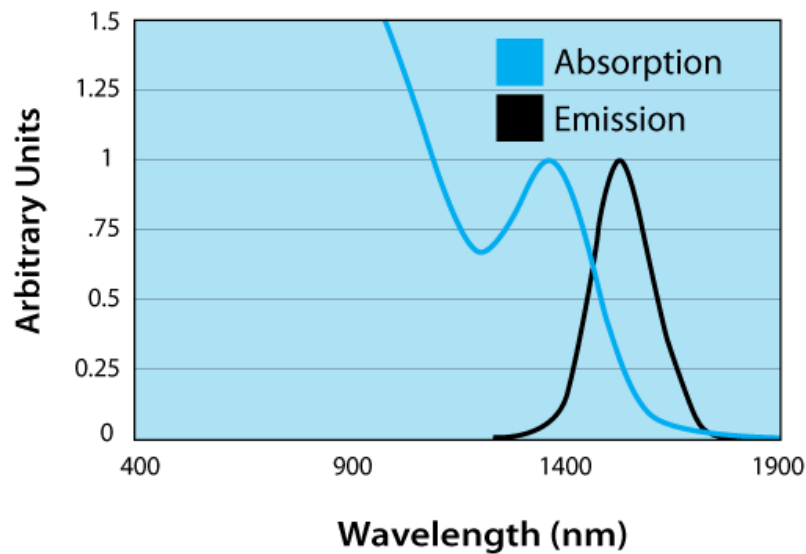


Figure 15. Absorption & emission spectra of 5.3 nm PbS quantum dots. 1st excitation peak of absorption is at 1450 nm whereas emission peak is at 1532 nm. (Provided by Evident Technologies)

PbS colloidal quantum dots with the crystal size of 5.5 nm is used in this work, which is purchased from Evident Technologies [51]. Diameter of 5.5 nm increases the effective bandgap of the bulk PbS value of 0.41 eV to 0.8 eV through the quantum size effect. This bandgap corresponds to an emission peak at 1532 nm and emission peak full width at half maximum (FWHM) of 149 nm. In addition to that 0.8 eV bandgap PbS quantum dots achieve a ground-state excitonic absorption peak at 1450 nm. The

absorption and emission spectra of 5.5 nm diameter PbS quantum dots that is provided by supplier is given in Figure 15.

PbS quantum dots are grown using organometallic CQD growth process, using the procedure very similar to the process given in Section 2.2. The synthesized PbS quantum dots are surrounded with oleic acid capping agent around them, which improves the surface passivation and serves as a dispersant. Quantum dots, with the help of oleic acid ligands are dispersed in toluene and are processed as dispersed in toluene. Total particle diameter of the PbS quantum dots including the oleic acid ligands is 9.5 nm.

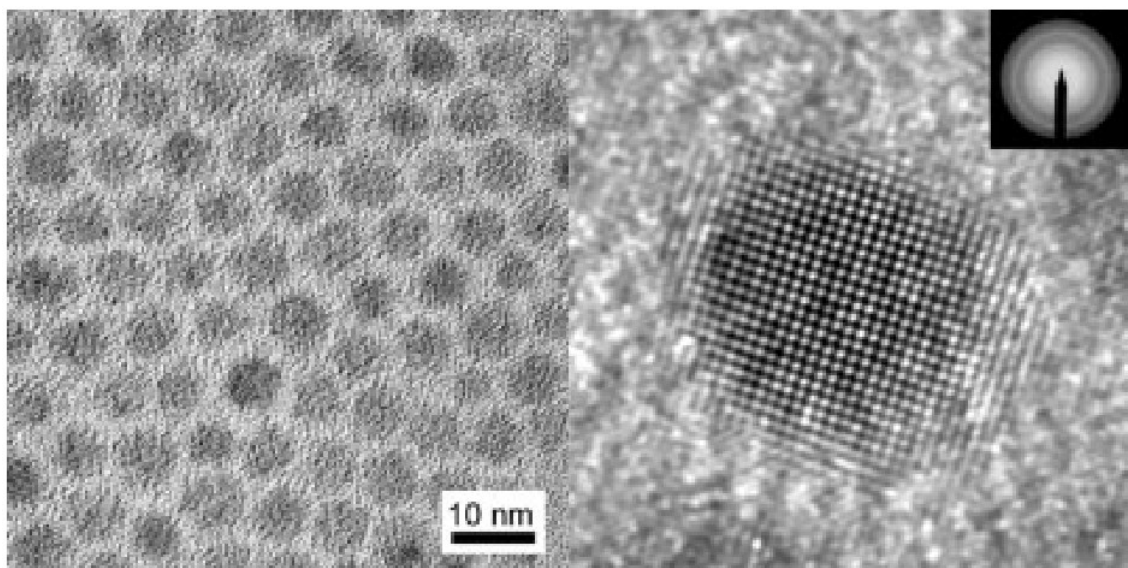


Figure 16. High resolution TEM images of PbS CQDs. On the left a monolayer of close packed CQDs is shown. On the right a close-up view of a single quantum dot is shown [52]

3.2.2 CQD Schottky Photodiode Architecture

In this work, schottky diode topology is selected because of faster response, so the metallurgical junction for the CQD photodiode is provided by a Schottky barrier to a CQD film. In a typical schottky photodiode, the rectifying property of the metal-semiconductor contact arises from the presence of an electrostatic barrier between the metal and the semiconductor, which is due to the difference in work functions ϕ_m and ϕ_s of the metal and semiconductor, respectively. The equilibrium energy band diagram

of a Schottky-barrier junction of metal/p-type semiconductor is shown in Figure 17. For a p-type semiconductor, ϕ_m should be less than ϕ_s . The barrier height is given as;

$$\phi_b = \chi_s + E_g - \phi_m \quad (3.1)$$

where χ_s is the electron affinity of the semiconductor and E_g is the bandgap energy. The potential barrier between the interior of the semiconductor and the interface, known as band bending, is given by equation 3.2

$$\psi_s = \phi_m - \phi_s \quad (3.2)$$

If $\phi_b > E_g$, the layer of the p-type semiconductor adjacent to the surface is inverted in type and we have a p-n junction within the material. However, in practice the built-in barrier does not follow such a simple relationship with ϕ_m and is effectively reduced due to interface states originating either from surface states or from metal-induced gap states and/or due to interface chemical reactions of metal and semiconductor atoms.

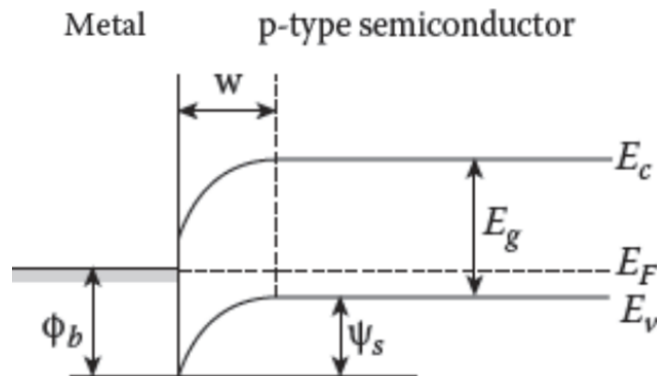


Figure 17. Equilibrium energy band diagram of Schottky-barrier junction of metal/p-type semiconductor [14]

The PbS CQD Schottky photodiode is formed by sandwiching photon sensitive semiconducting PbS CQD film between low workfunction metal Schottky contact and transparent ohmic indium tin oxide (ITO) contact. The photodiode is fabricated on glass substrate and the illumination is applied from glass substrate side. A planar, transparent indium tin oxide (ITO) conductive thin film is deposited on glass substrate. ITO layer on this device forms the opposing ohmic contact to the metal/Pbs CQD Schottky diode. The Schottky barrier, in this work, is formed at the interface between the PbS CQD film and a low work function metal such as titanium (Ti) / gold (Au) stack or aluminum (Al).

The working principle is such that incident light from glass substrate travels from transparent ITO contact and generates electrons and holes in depletion region of CQD and schottky metal contact, and these electrons and holes are collected at the Ti-Au or Al and ITO contacts, respectively.

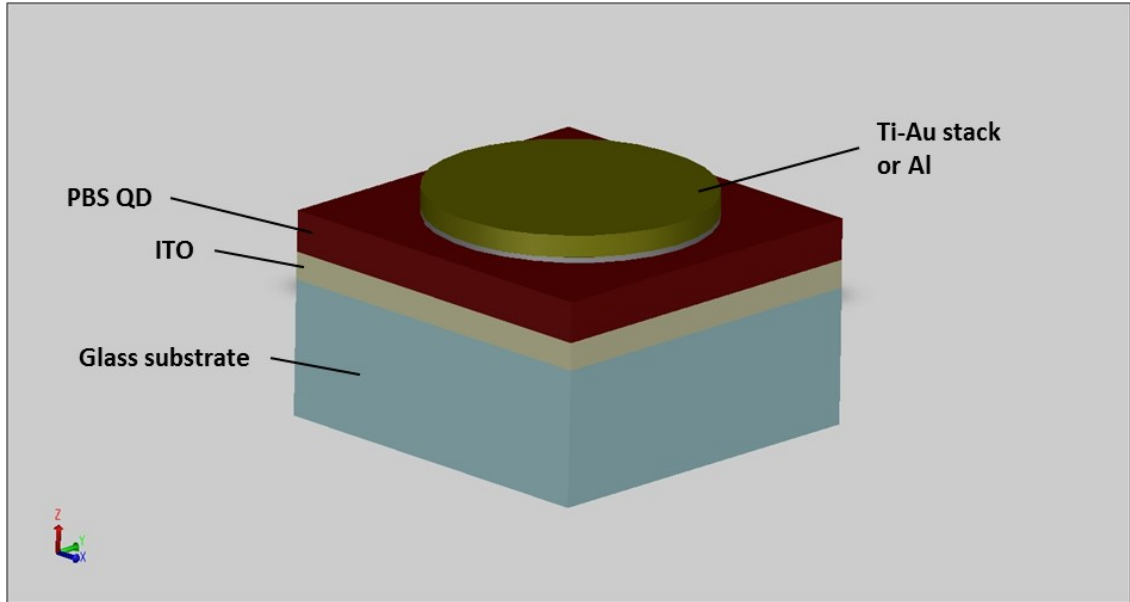


Figure 18. 3D schematic of the PbS quantum dots based schottky photodiode composed of ITO anode, photosensitive PbS quantum dot layer and schottky cathode composed of Ti and Au stack or Al.

Figure 19 shows the energy band diagram of the Schottky barrier formed at the Au-Ti or Al and PbS CQD interface. The built-in potential, V_{bi} is resulted from the difference in work functions between the CQD film and the schottky metal contact as mentioned before in this section. Charge transfer between the semiconductor and the metal results in the formation of a wide depletion region in the CQD film, while the remaining volume of CQD film is a quasi-neutral region of p-type semiconductor with no net charge or electric field. The large potential barrier in the valence band limits majority carrier (hole) injection from the Al contact, resulting in highly rectifying dark I-V characteristics [53].

The fabrication process of the devices starts with ITO coated glasses as a substrate that is provided by Teknoma [54]. The transparent conductive layer, ITO has the conductivity of $25 \Omega/\square$ and transparency of 60% around 1500 nm as shown in Figure 20. The photosensitive layer composed of PbS quantum dots is formed by spin coating on ITO coated glass. Layer by layer deposition technique is used to form a pinhole and

crack free PbS QD layer which will be discussed in following sections. As a final step Schottky metal contact composed of either Ti-Au stack or Al is sputter deposited on PbS layer using a shadow mask of different photodetector active area sizes. The final structure of the device is shown in Figure 18.

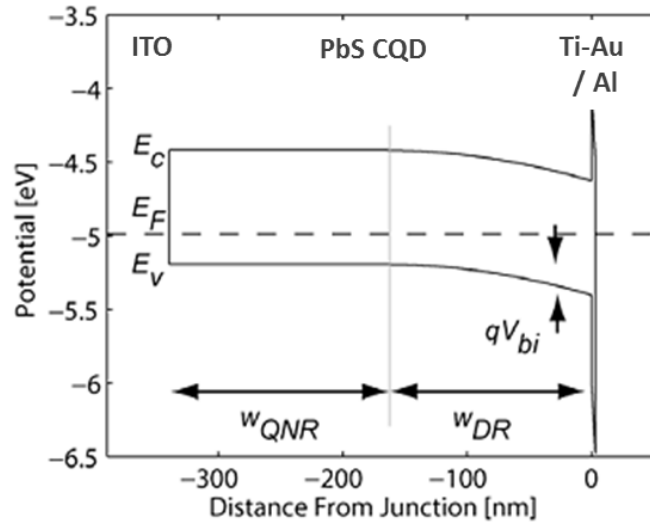


Figure 19. The Schottky barrier at the Ti-Au or Al CQD interface forms a depletion region (DR) in the CQD film with a bias dependent width (w_{DR}) and a built in potential (V_{bi}). The remaining CQD film is unaffected by the Schottky barrier and is denoted as quasi-neutral region (QNR) [53]

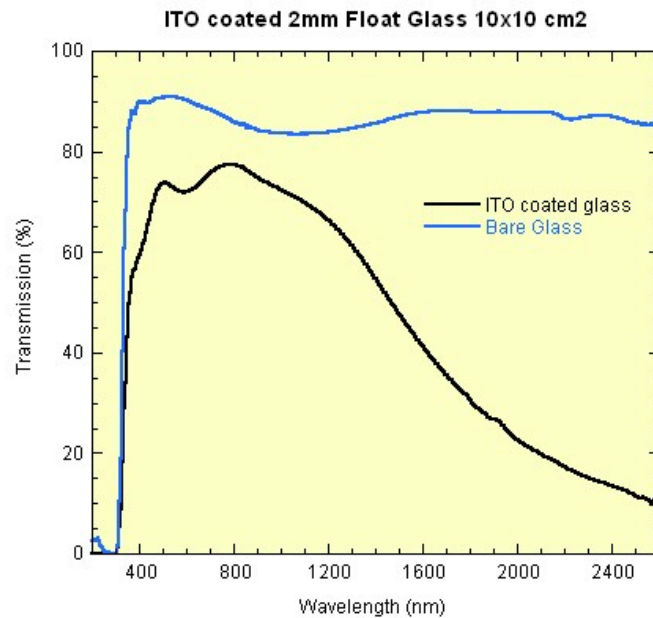


Figure 20. Transmission spectra of the glass samples and the ITO coated glass samples used in the work provided by Teknoma [54]

3.3 Deposition of CQD PbS films

Solution-synthesized colloidal quantum dots can readily be deposited using spin-coating, spray-casting, or inkjet printing techniques on any substrate conducting or insulating, crystalline or amorphous, rigid or flexible.

3.3.1 Spin Coating

The spin coating technique is widely used in microelectronics to apply photoresists. This technique allows obtaining thin homogeneous layers by dropping the liquid on a substrate maintained on a rotary chuck Figure 21. By rotation at appropriate acceleration, speed, and time, the liquid is spread by the centrifugal force. The film thickness depends on the fluid viscosity and the rotation speed. At the end of the process, one side of the substrate is coated.

3.3.2 Dip coating

Dip coating is the method of choice if both sides of the substrate need to be coated. It is used in large scale for industrial applications such as specific treatments for large area windows or scratch resistance treatment for optical lenses. The principle consists of immersing the substrate in the coating liquid and lifting it out to deposit the coating Figure 22. The coating thickness depends on the lifting speed and on the fluid viscosity. One of the main drawbacks is the comparably large volume of liquid needed.

3.3.3 Inkjet printing

Inkjet printing is commonly used in everyday life and also is a well-known technique to dispense silver inks to use as low cost conductive traces. Inkjet printing is becoming more and more popular in organic electronics as it is a versatile and contactless technique. It consists of dispensing the fluid in the form of picoliter droplets through a print-head (Fig. 6). There are two main technologies in current inkjet printers, continuous inkjet (CIJ) and drop-on-demand (DOD). In the continuous technology the ink is delivered in a continuous flow and the drops are deviated to the substrate depending on the digital pattern to print. In the drop-on-demand technology, the drop is delivered on demand depending on the digital pattern. This technology is also divided in

two delivering method: thermal DOD and piezoelectric DOD. This last option is mostly used in material jetting. A drop is formed when the piezoelectric part of the print-head is bent by an applied voltage. To increase productivity, print-heads got several nozzles able to deliver many droplets at once. Using inkjet printing, patterning a device is straight forward and only a low volume of ink is necessary. The ink viscosity needs to match the print-head nozzle size and influences the final thickness of the printed area.



Figure 21. Schematic of spin deposition process including drop, spread, coat, dehydrate steps [47]

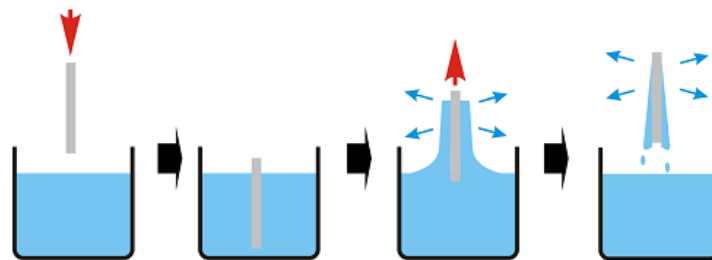


Figure 22. Steps of dip coating deposition process [47]

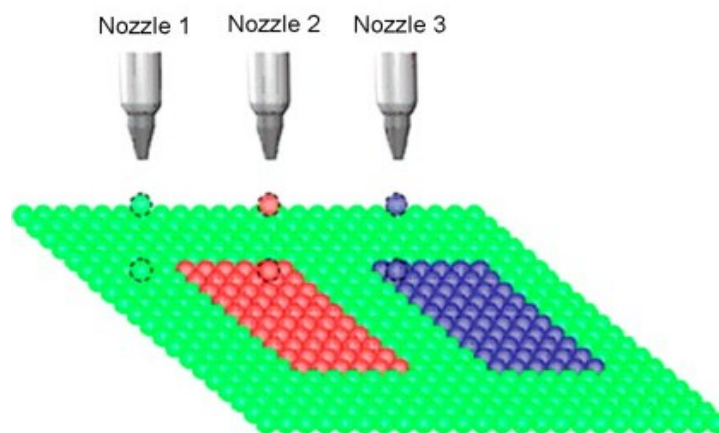


Figure 23. Schematic representation of inkjet printing [47]

3.3.4 Layer by layer spin deposition of PbS CQDs

Among different available techniques of solution based material coating, spin coating method is used in this work. The reason for that is spin deposition is well established process, enabling better thickness control, consuming less material than dip coating and less complex and cost effective process than inkjet printing. PbS quantum dots dispersed in toluene is dropped to the surface of ITO coated glasses and successfully coated with spinning at moderate speeds.

The goal of the optimization steps carried out while spin coating the PbS CQD layer is to achieve a uniform, pinhole and crack free PbS layer with the thickness around 250 nm. Absorbance of PbS CQD layer lies in the range of 10^4 - 10^5 cm^{-1} [31] so thick layers of PbS CQD layers is required to fully absorb the incoming light. However minority carrier diffusion lengths in these layers are around 100-200 nm and can be increased by correct ligand passivation [31]. So in order to have moderate absorption and fast device we have selected the PbS CQD layer thickness as 250 nm.

The important parameters in the process of achieving good quality coatings was spin speed and PbS CQD concentration in toluene. Many trials have been made varying the spin speed. At slow speeds, such as 1000 rpm, non-uniformity of the coated layer increases; whereas, at very high spin speeds nanocrystals cannot successfully stick to the substrate surface. As a result it has been observed that 2500 rpm spin speed has provided the best results.

PbS quantum dots concentration in toluene was another important parameter that affects the quality of coated film. Throughout the work, various concentrations of PbS are used in spin coating process. Low concentrations of PbS in toluene is used at first such as 10 mg/mL and these concentration levels resulted poor quality PbS films with cracks and pinholes. The best quality films are achieved with 40 mg/mL PbS concentration in toluene. It is important to note that the concentration and spin speed parameters are correlated with each other, so the parameters are changed iteratively to achieve optimum results.

Special importance has been given to forming a pinhole-free, crack free and uniform PbS quantum dots film on ITO coated glass substrate. Using low concentration PbS quantum dots in toluene caused pinholes and cracks in the film and this resulted

shorts between ITO and Schottky metal contact. The devices prepared with this poor quality films resulted resistance like behavior.

In order to get rid of these pinholes and cracks, layer by layer (LBL) spin deposition technique is used. 150 μL of 40mg/mL PbS CQD in toluene is dropped onto the surface and spinned at 2500 rpm. Then solid state ligand exchange procedure is applied, which will be described in following section, and the sample is washed with 1 mL of methanol. As a final step, a 1 mL of toluene is dropped on surface and the sample is spinned again in order to relocate PbS quantum dots to achieve a uniform coating. All these processes are repeated 9 times to reach 250 nm PbS CQD film thickness and also to achieve smooth, pinhole and crack free, uniform PbS CQD layer. SEM picture of the resulted film is shown in Figure 25. Comparing to Figure 24, it can easily be seen that the film has no cracks or pinholes. Also Energy Dispersive Spectrometer (EDS) in SEM is used to chemically analyze the coated film. This time PbS quantum dots are deposited on silicon substrates coated with SiO_2 and aluminum. The EDS analysis result is shown in Figure 26. The peaks Pb and S can easily been observed, indicating that the film is formed successfully. Also C and O peaks refer to oleic acid capping layer around the PbS quantum dots. Strong peaks of Si and Al comes from the substrate used.

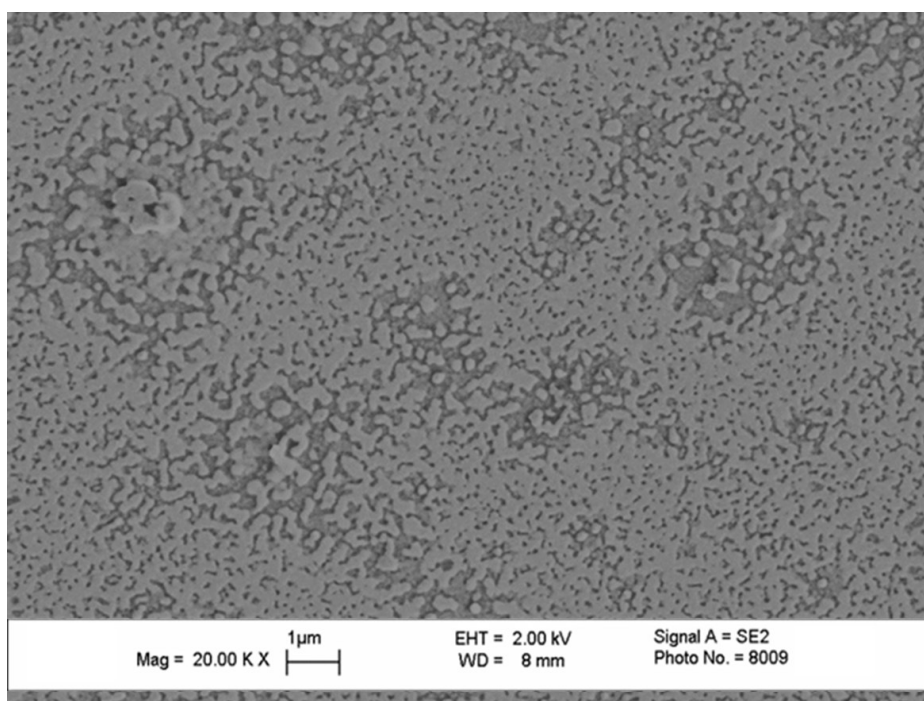


Figure 24. Poor quality PbS CQD films with pinholes and cracks as a result of low concentration PbS in toluene use

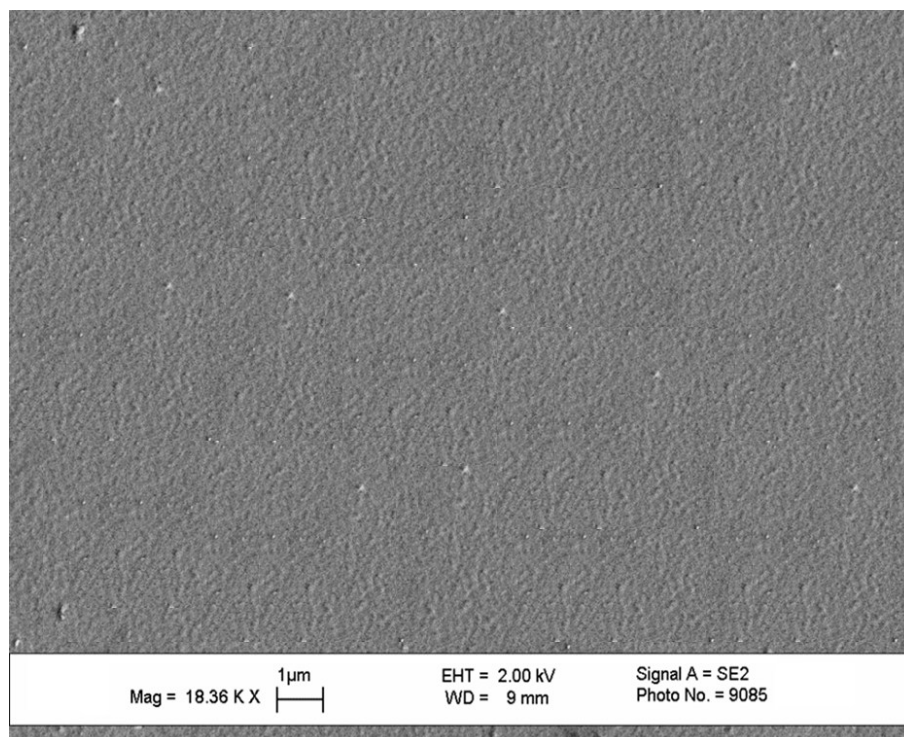


Figure 25. Pinhole free good quality PbS CQD films achieved with optimized concentration and layer by layer deposition process

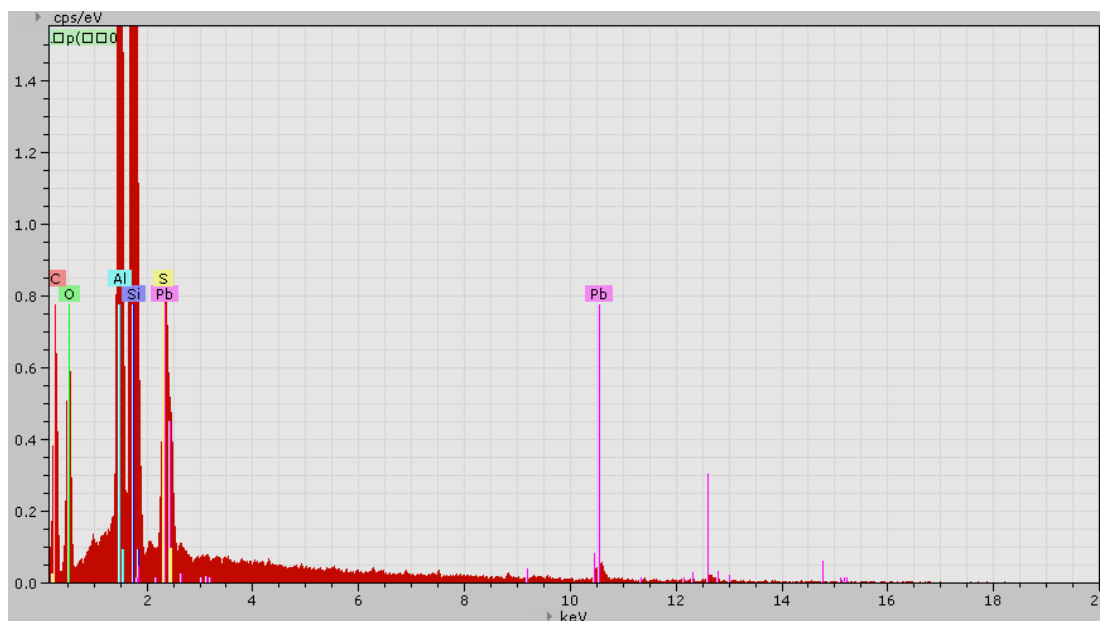


Figure 26. EDS analysis of the PbS CQD layer coated on Al deposited Si/SiO₂ substrates. The Pb, S peaks can easily be seen together with C and O peaks that come from oleic acid.

3.4 Surface Modification on CQD Films: Ligand exchange

Charge collection in the active PbS CQD layer is most efficient in the depletion region. Therefore, the optimal thickness of the active layer is usually kept close to the depletion width [55]. The efficiency of photodiodes is determined in part by the efficiency at which photons are absorbed and converted into independently diffusing charge carriers and by the quantum yield for collecting those charge carriers in an external circuit. Optimized test structures must balance competing demands of these processes because each is optimized under different conditions. For example, a thick active layer is required to absorb higher portion of the incident photons at the bandgap of CQDs. On the other hand, charge collection efficiency decreases as the active layer increases in thickness because charge carriers are susceptible to recombination if their transit time exceeds the charge recombination lifetime. This competition between electrical transport and charge recombination sets an effective electrical length of a few hundred nanometers in optimized devices. The need to balance these processes makes it challenging to construct CQD test structures that absorb all incident photons, especially those in the near-IR close to the band gap. A promising approach against the trade-off between efficient light absorption and charge collection to increase the external quantum efficiency particularly at the band gap of PbS CQD films is to enhance the diffusion length of charge carriers; so that, charges can be harvested from thicker PbS layer active layers [56]. The diffusion length, l , of charge carriers is related to the square root of the mobility-lifetime product, $\mu\tau$, according to equation 3.3,

$$l = \sqrt{\frac{k_B T}{e} \mu \tau} \quad (3.3)$$

where k_B , T and e are Boltzmann's constant, temperature and the elementary charge [57]. PbS CQDs, following the synthesis are generally capped with organic ligands that employ long chains (8-18 carbons) to ensure the surface passivation and solution processability [58]. Oleic acid is one of the most commonly used organic ligand in PbS colloidal quantum dots. These long ligands produce insulating barriers between CQDs that reduces efficient carrier transport when processed into films. Therefore these long ligands have to be changed by shorter ligands in order to minimize inter-particle spacing to promote carrier transport and lower the defect density to reduce recombination loss.

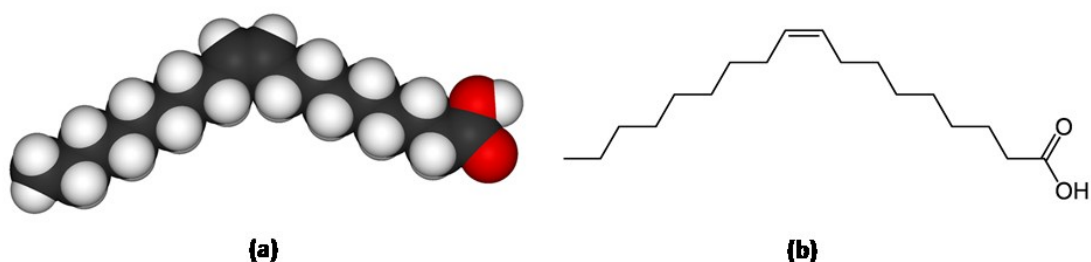


Figure 27. Long chain of oleic acid ($C_{18}H_{34}O_2$) used for organic ligand for passivation and solubility of PbS colloidal quantum dots. a) 3D molecular illustration where black spheres stands for H_2 , white spheres stands for C and red ones are O atoms [59].

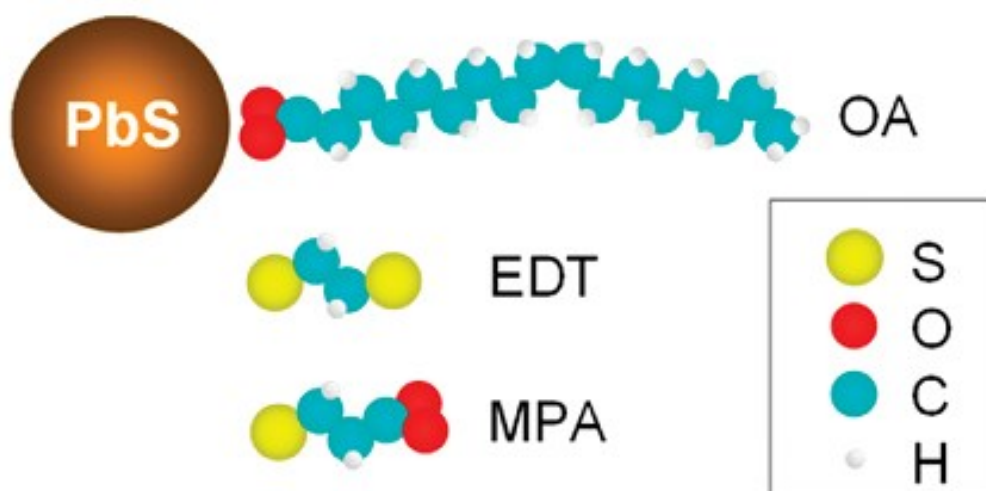


Figure 28. Structure of originally oleic acid capped PbS QD and the shorter ligands to replace long OA chain [57]

Several ligand exchange strategies have been explored in the literature that include replacement of the original ligands with ethanedithiol [60], benzenedithiol [61], hydrazine [62], and pyridine [63] etc. These solution state ligand exchange treatments have led to impressive enhancements of carrier mobilities. In addition to that solid state ligand exchange procedures studied utilizing ethanedithiol (EDT) and 3-mercaptopropionic acid (MPA) leading to 7 fold improvement in mobility lifetime product comparing traditional organic passivation strategies [57]. Structures of shorter ligands; 3 carbon MPA and 2 carbon EDT is shown in Figure 28.

In this work, solid state ligand exchange procedure is applied to replace long oleic acid ligands with shorter MPA ligands in order to enhance the mobility-lifetime products of PbS CQD films leading to increases in both the diffusion lengths of charge carriers and the efficiencies of PbS CQD photodiodes.

Table 2. List of process steps used in layer by layer spin coating of PbS QDs and ligand exchange procedures

	Step #	Step Name	Sample Amount	Spin Speed	Spin Time
Ligand exchanged PbS CQD Coated Layer 1	1	Spin Coating	150 μ L	2500 rpm	15 sec.
	2	Ligand Exchange by 3-MPA (1:10 in methanol)	200 μ L	2500 rpm	15 sec.
	3	Methanol rinse and dry	1 mL	2500 rpm	45 sec.
	4	Toluene rinse and dry	1 mL	2500 rpm	45 sec.
	5	Final Drying	-	2500 rpm	45 sec.
	⋮	Steps 1 – 5 are repeated as many as desired (9 time in this study) to achieve the required film thickness			
	Final	Anneal	In ambient conditions	100 °C	5 min

Solid state ligand exchange procedure is applied in parallel to spin deposition steps and takes place in the spin coater. First 3-mercaptopropionic acid in methanol solution, 1:10, is prepared which will be mainly used for ligand exchange. After the first layer of PbS CQD is coated, the 3-MPA solution previously prepared is dropped on the coated PbS layer and then the sample is spun again to remove the excess solution. When 3-MPA is applied to the surface, ligand exchange takes place. Methanol in the solution, removes the oleic acids from the surface of PbS nanocrystals and 3-MPA ligands in the solution binds in places of OAs. This step is repeated three times in order to be sure that ligand exchange is completed for all PbS particles. Following this step, the sample is flushed with methanol three times to remove the bi-products of ligand

exchange reactions. Once the ligand exchange is completed and the bi-products are removed from the surface, the sample is flushed with toluene that relocates the ligand exchanged PbS QDs and improves the uniformity of the film. Finally the sample is spin dried and coating of one layer of ligand exchanged PbS CQD is completed. All these steps are repeated 9 times to achieve smooth shiny PbS QD film of 250 μm thickness. As a final step, when the desired thickness is achieved, the sample is annealed in ambient conditions at 100 $^{\circ}\text{C}$ for 5 minutes. All these steps are given in Table 2 together with used sample quantities, spin speeds and spin time required for each step. It is important to make note again that steps 1 to 5 is repeated many times to achieve the desired thickness of the PbS film. And also very thin films such as 1 layer or 2 layer, have pinhole problems but after 3rd layer the problem is removed and no shorts depending on the pinholes have been observed after this thickness. In this work, steps from 1-5 are repeated ranging from 9 times.

3.5 Schottky Metal Deposition

The fabrication process of the CQD Schottky photodiodes starts with ITO coated glasses. ITO serves as conductive and transparent ohmic contact as described in previous sections. Then the PbS CQD layer is deposited by layer by layer spin coating process and also the ligand change procedure is applied during the LBL coat process which is described in detail in section 3.3 and 3.4. Last step of the fabrication process involves deposition of the Schottky metal through the shadow mask.

A shadow mask is designed that have circular openings of 200 μm . A 20 mm X 20 mm square thin aluminum sheet is drilled using ultra-precision CNC machine KernEvo in order to be used as shadow mask to define the Schottky metal area, and thus the active area of the detector. When depositing Schottky metal this hard mask is attached to the surface of coated PbS layer. In this way, the metal is only come in contact with PbS CQD layer at opened areas of the shadow mask. After deposition is finished, the mask is removed leaving circular Schottky contacts. This is a very easy and straight forward process to define metal contacts on PbS CQD surface.

Low work function metals such as Al and Ti-Au stack used in order to create Schottky barrier on PbS CQD interface. DC sputter deposition technique is used to deposit schottky metals on top of PbS CQD layer. No chamber or substrate heating is

applied during sputtering process in order not to affect PbS quantum dot layer by exposing it to high temperatures.

Aluminum layer is directly sputter deposited from aluminum target. First the chamber base pressure is pumped down to 10^{-6} mbar pressure. Then 5 min pre sputtering is applied with 35 sccm argon flow and chamber pressure is kept constant at 2×10^{-2} mbar. 150 W DC power is applied for both pre sputtering and deposition process. Following the pre sputtering, deposition started with same parameters and 10 min deposition resulted in ~ 200 nm Al film on top of PbS CQD.

For titanium-gold stack samples the sputtering is started with Ti target. The chamber pressure is pumped down to 10^{-6} mbar. Following this Ar flow is set to 35 sccm and the chamber pressure is adjusted to 1.7×10^{-2} mbar. DC power for Ti deposition is applied as 310 W. After 5 min pre sputtering, Ti is sputter deposited 3 min. Subsequently, the chamber is vacuumed again and the DC power is connected to gold magnetron. Ar flow is set to 35 sccm and chamber pressure is adjusted to 1.7×10^{-2} mbar by adjusting positional valve. Setting the DC power to 110 W, Au is deposited 3 min. The resulting thickness is measured as 150 nm. Sputter deposition parameters summary is given in Table 3.

Table 3. Sputter deposition parameters of Schottky contact metals

Target	Base Pressure	Ar Flow	Deposition Chamber Pressure	DC Power	Pre-Sputtering Time	Deposition Time
Aluminum	1×10^{-6} mbar	35 sccm	2×10^{-2} mbar	150 W	5 min	10 min
Titanium	1×10^{-6} mbar	35 sccm	1.7×10^{-2} mbar	310 W	5 min	3 min
Gold	1×10^{-6} mbar	35 sccm	1.7×10^{-2} mbar	110 W	0	3 min

3.6 Measurement procedure and results

3.6.1 Test setup

Since the dimensions of the photodiodes are relatively small, the electrical and optical characterizations are carried out in Cascade PM5 DC probe station using tungsten needles and the probe station is equipped with a shielded enclosure. The overall system is shown in Figure 29. The probes are used to take contact from underlying ITO layer and top Al or Ti-Au Schottky contact. For dark current measurements and I-V characterization, probes are connected to Agilent Semiconductor Parameter Analyzer.

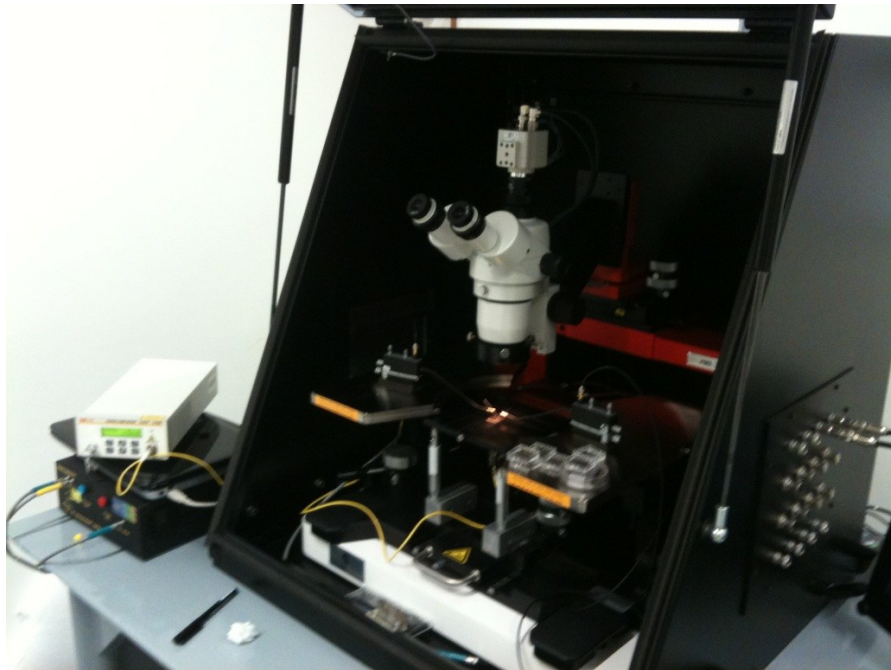


Figure 29. DC probe station equipped with shielded enclosure used for electrical and optical characterization

As mentioned before, the photodiodes in this part are realized on glass substrates with a transparent and conductive ITO bottom ohmic contact. So, the device is exposed to illumination from the bottom. This introduces a challenge while constructing the test setup because we have to probe the contacts in order to apply and measure signals in the device and at the same time we have to expose the sample from the bottom where normally the device in probe station sits on vacuum chuck.

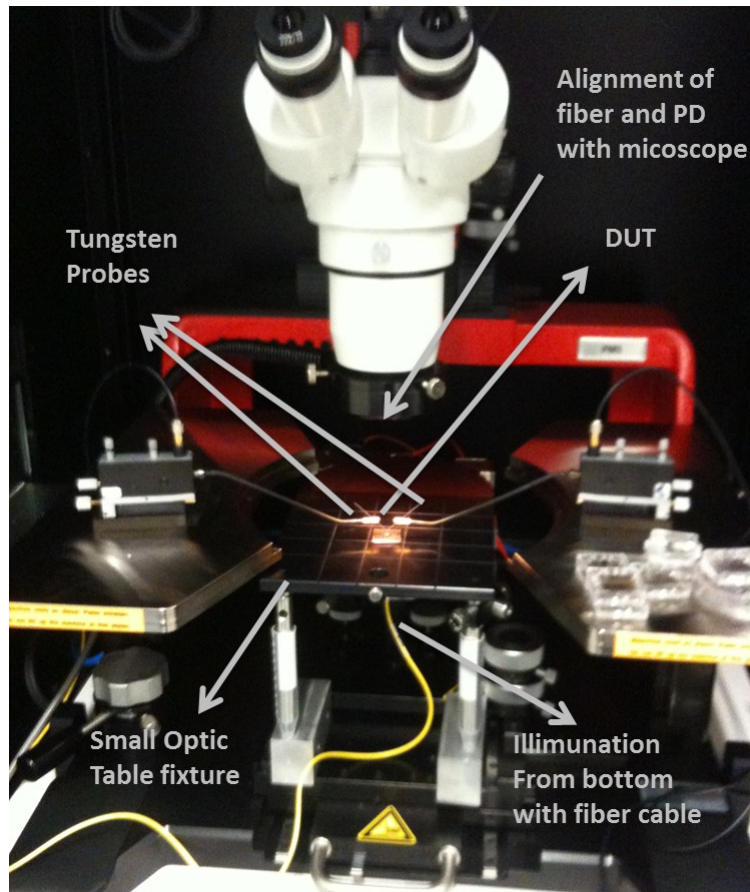


Figure 30. Probe station chuck is replaced with optic table for exposing the device from the bottom with a fiber cable

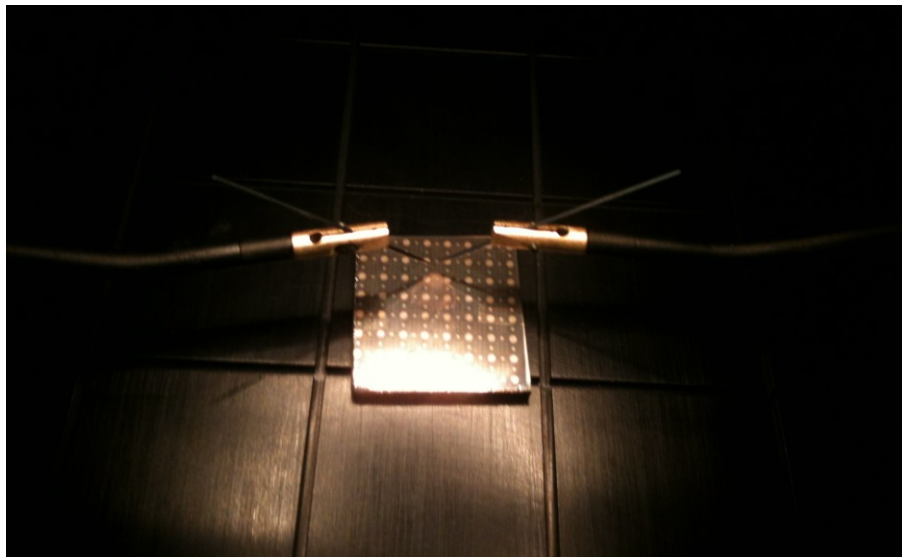


Figure 31. Since the contact areas are very small, photodiodes are measured with the help of Tungsten probes. The photodiode is illuminated from the bottom.

As a solution, the probe station chuck is replaced with a small optic table that has a threaded opening in the center. Fiber cable from an illumination source is connected to

this fixture and fixed as close as possible to the bottom of the sample. The alignment of the fiber and the photodiode is done with the help of powerful microscope of the probe station. The modified probe station configuration for optical characterization is shown in Figure 30. A closer picture of the photodiode with probes are connected and illuminated from the bottom with the fiber optic cables can be seen in Figure 31.

3.6.2 Test and characterization of Al/PbS CQD photodiode

As described in previous sections in detail, a Al/PbS CQD schottky photodiode is designed and fabricated on glass substrate. ITO coated glass substrate is coated with PbS CQD film, using layer by layer technique composed of 9 layers, resulting thickness of 250 nm. Then Schottky contact is formed by depositing Al through shadow mask. The measured photodiode has a diameter of 400 μm .

As a first step, the photodiode is placed in Probe station and connected to Agilent Parameter Analyzer to measure current voltage diode characteristics under dark. The enclosing shield is closed while making measurements in order to block the surrounding light. The bias voltage is applied to Al contact and swept from -2 V to 2 V and diode currents are measured for each applied bias voltage. The resulting I-V graph of Al/PbS schottky diode is given in Figure 32. The dark current of the Al/PbS diode is found to be 2.19 nA at 1V reverse bias. This high dark current can be attributed to the interaction of PbS–Al interface. Sputter depositing Al on PbS CQD film may be damaging the surface resulting high dark currents.

The slope characteristic in Figure 32 is the typical diode behavior such that, at reverse applied biases, a small amount of reverse current flows till the breakdown and at forward biases the current increases exponentially with the applied bias. Strong rectification is observed in Al/PbS schottky photodiode; such as at -1 V the diode current is 2.19 nA and at +1 V the diode forward bias current is 67.8 nA giving a rectification of 30. At higher voltages, such as ± 2 V, the rectification increases to ~ 100 . The exponential portion of the forward bias I-V characteristic is well-described by a simple diode equation, Equation 3.4, where J_s is the saturation current density, q is the electronic charge, V is the potential drop across the junction, n is the ideality factor, k_B is Boltzmann's constant and T is the temperature.

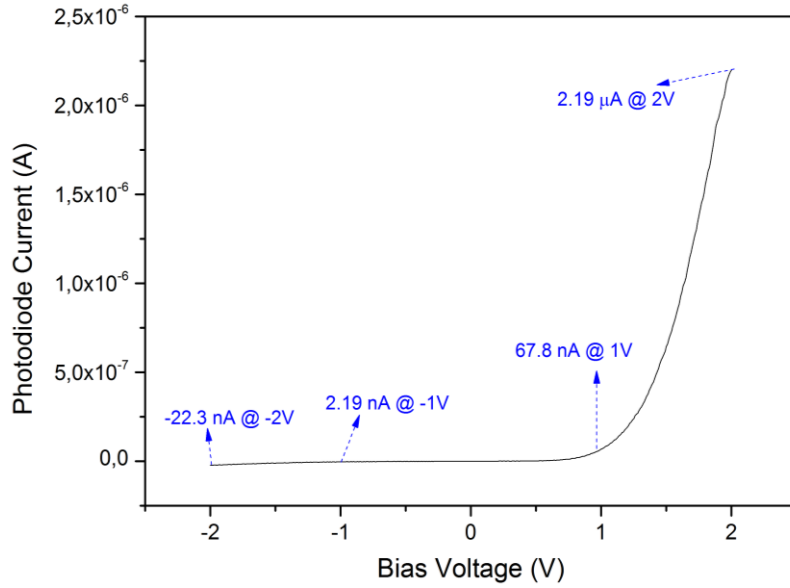


Figure 32. I-V characteristic of Al/PbS CQD schottky photodiode under dark conditions. Strong rectification is observed at ± 1 and 2 volt applied bias voltages.

$$J = J_s \left[\exp\left(\frac{qV}{nk_B T}\right) - 1 \right] \quad (3.4)$$

In addition to that the reverse-bias characteristics of the CQD Schottky barrier are in line with the diffusion theory which suggest that the field in the depletion region is dependent on applied bias, resulting in non-saturating reverse-bias currents.

As a next step the Al/PbS CQD schottky photodiode is tested under illumination. The setup of the probe station is changed, as described in section 3.6.1, to illuminate the sample from the bottom while applying and measuring signals from the top contacts with the help of tungsten probes. The probes are connected to Semiconductor Parameter Analyzer and first I-V measurement for $\pm 2V$ is taken under dark conditions at room temperatures. After that the detector is illuminated from bottom with ThorLabs TL200C Tunable Laser Source that is tunable between the wavelengths 1527-1568 nm. In addition to this, the illumination irradiance on sample is calibrated using ThorLabs PM100 Optical Power Meter System. The Germanium (Ge) detector of Optical Power Meter System is put in place of the Al/PbS detector on the small optic table and then the power on the PbS detector is estimated from the power reading on the reference detector. It is found to be that the Al/PbS detector is illuminated with $5\text{mW}/\text{cm}^2$

The current characteristics depending on applied bias in both dark and when exposed to $5\text{mW}/\text{cm}^2$ illumination at 1527 nm is given in Figure 33. The red curve on

the graph represents the diode current under illumination and the black curve represents the dark current. Under photovoltaic operation at 0 V bias, the photocurrent is measured as 3,44 nA. When -1 V reverse bias voltage applied, the dark current is 2.2 nA and under illumination the photocurrent is 78.2 nA which presents 35 fold increase. Increasing reverse bias to -2 V, the responsivity to illumination improves a lot, as shown in Figure 33. The dark current was high under -2V reverse bias as 22.33 nA, however, when exposed to 5 mW/cm² illumination the current increases to 1.25 μA which is more than 50 fold increase. It can be easily seen that by increasing the reverse bias the photocurrent and the responsivity increases. The reason of this is the widening of depletion region by the applied reverse bias. Since the charge collection is more efficient in depletion region the responsivity of the detector increases. Another reason of this behavior is that, as the reverse bias increases the barrier becomes thinner and the hole injection from Al contact increases.

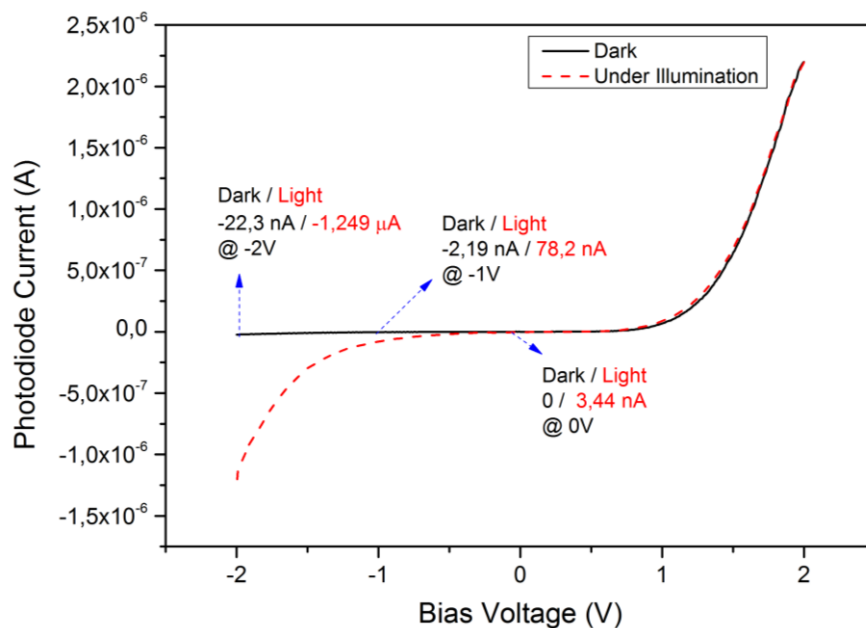


Figure 33. I-V curves of Al/PbS CQD schottky photodiode under dark (black curve) and under 5 mW/cm² illumination (red curve)

At zero bias the responsivity was low and quantum efficiency is measured was very low. When 1V reverse bias is applied, we observe an increase in the responsivity, but still it was quite low for a photodetector such as 0.012 A/W. Also the normalized detectivity is calculated based on the previous assumption that the noise-current spectral density is dominated by shot noise in the dark current and it is found to be $1,62 \times 10^{10}$ Jones. Increasing the reverse bias voltage more, to 2 V, the device response to

illumination is dramatically increased. The responsivity measured in 2 V reverse bias is around 0,195 A/W. The Al/PbS photodiode achieved 15,6 % quantum efficiency at this point. The normalized detectivity in 2 V reverse bias is calculated as $8,19 \times 10^{10}$ Jones.

The Al/PbS photodiode is also illuminated at a range of different wavelengths by ThorLabs TL200C Tunable Laser Source that is tunable between the wavelengths 1527-1568 nm. The absorption peak of the PbS CQDs was 1450 nm and the absorbance decreases after the peak point as shown in Figure 15. The photoresponse of the Al/PbS photodiode to illuminations at three different wavelengths is shown in Figure 34. It can be observed that as the wavelength increases from 1527 nm to 1568 nm, the photoresponse of the detector decreases. This is because the absorption coefficient of the PbS CQDs decrease and thus there is less absorbed photons to generate electrons and holes. For instance under 2V reverse bias, dark current is 24.248 nA and the current increases 1461.1 nA at 1527 nm illumination, 1047.9 nA at 1547 nm illumination and 862.2 nA at 1567 nm illumination.

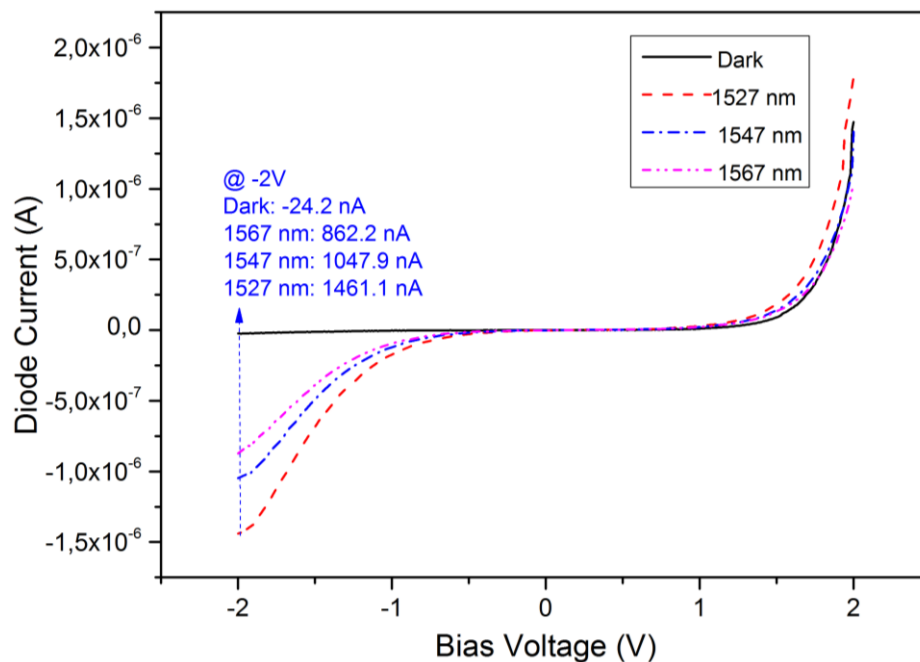


Figure 34. I-V curves of Al/PbS CQD schottky photodiode under dark (black curve), and under 5 mW/cm^2 illumination centered at 1527 nm (red curve), 1547 nm (blue curve) and 1567 nm (magenta curve).

3.6.3 Test and characterization of Au-Ti/PbS CQD photodiode

An alternative to Al/PbS CQD schottky photodiode, Ti-Au/PbS CQD schottky photodiode is also designed and fabricated on glass substrate. ITO coated glass substrate is coated with PbS CQD film using layer by layer technique composed of 9 layers resulting thickness of 250 nm. Then Schottky contact is formed by depositing Ti and Au metal layers through the shadow mask.

As a first step, the photodiode is placed in Probe station and connected to Agilent Parameter Analyzer to measure current voltage diode characteristics under dark. The enclosing shield is closed while making measurements in order to block the surrounding light. The bias voltage is applied to Ti-Au contact and swept from -4 V to 2 V and diode currents are measured for each applied bias voltage. It should also be noted that after 4V reverse bias, the diode enters breakdown. The resulting I-V graph of Ti-Au/PbS schottky diode is given in Figure 35.

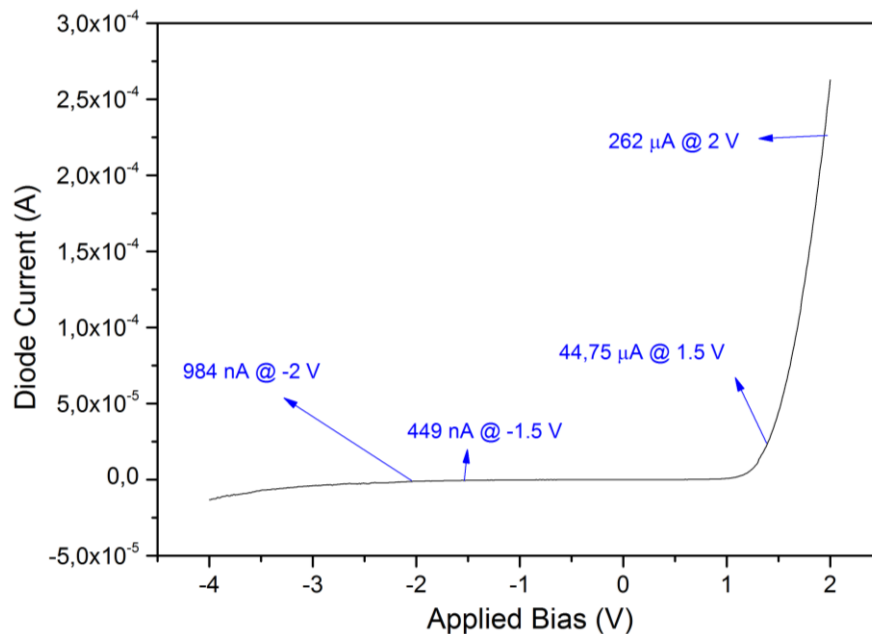


Figure 35. I-V characteristic of Ti-Au/PbS CQD schottky photodiode under dark conditions. Strong rectification is observed at ± 1.5 volt applied bias voltages

As seen in Figure 35 and as it was in Al/PbS case, the Ti-Au/PbS photodiode also show schottky diode characteristics such that on positive applied biases the current changes exponentially with applied bias, whereas on reverse applied biases small amount of reverse current flows. This device show higher rectification ratios than the Al/PbS one. At 1.5 V forward bias 44,75 μ A current flows from the diode whereas at

1.5 V reverse bias only 449 nA current flows giving rectification ratio of 100. Increasing the forward bias to 2 V, the diode current increases even 262.77 μA and 2V reverse bias results a reverse bias current of only 984 nA giving a rectification ration of 267.

Next, the photoresponse of Ti/Au-PbS photodiode is measured at dark and 5 mW/cm^2 illumination at 1527nm wavelength and the resulting I-V graph is presented in Figure 36. The red curve on the graph represents the diode current under illumination and the black curve represents the dark current. It can be seen from the graph that the photoresponse increases in parallel with the reverse bias. When 1 V reverse bias voltage applied, the dark current is measured as 117 nA and when the diode is illuminated the total current increases to 599 nA. Increasing reverse bias to 2 V, the dark current increases to 985 nA and the total current under illumination increases to 3.23 μA . At 3V reverse bias dark current is 3.9 μA and the photocurrent is 8.09 μA and further increase in reverse bias up to 4V results in dark current of 13.1 μA and the photocurrent of 18 μA .

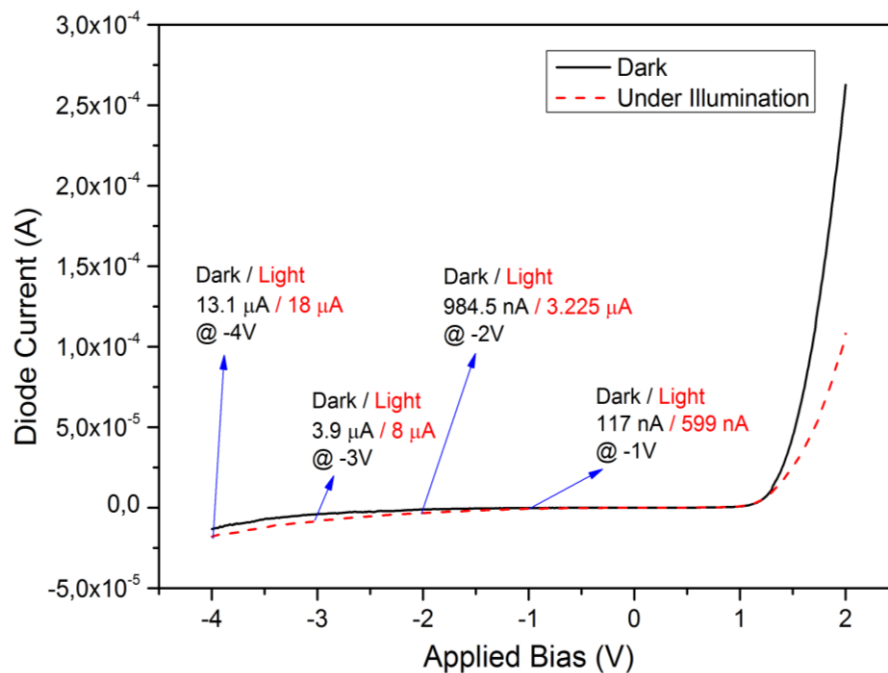


Figure 36. I-V curves of Al/PbS CQD schottky photodiode under dark (black curve) and under 5 mW/cm^2 illumination (red curve)

The dark current values of the Ti-Au/PbS diode are higher than Al/PbS. These high dark currents can be attributed to the interaction of PbS–Ti/Al interface. Sputter

depositing of Ti is done at higher powers than Al and the higher damage to PbS layer may increase the dark current in the device.

Comparing to Al/PbS photodiode counterpart, Ti-Au/PbS photodiode presents higher dark currents, on the other hand, they achieve higher photocurrents under same illumination. For instance, under 1V reverse bias, Ti-Au/PbS photodiode has 117 nA dark current, yet, under 5 mW/cm² illumination, it creates 599 nA photocurrent. These results give us a low responsivity and a quantum efficiency of 6.14%. The detectivity of photodiode is measured as $1,41 \times 10^{10}$ Jones. At 2V reverse bias, the dark current increases dramatically to 985 nA and the photoresponse to 3,23 μ A. The responsivity extracted from these parameters is around 0,356 A/W which is higher than the Al/PbS diode, and a quantum efficiency of 28,5 %; however, the detectivity of Ti-Au/PbS is $2,25 \times 10^{10}$ Jones, which is lower than Al/PbS diode because of the high dark current. High dark current limits the sensitivity of the diode. Increasing the reverse bias voltage to 3V, the dark current increases more, to 3,9 μ A and the photocurrent to 8.09 μ A, which translates into an increase in the responsivity that is extracted as 0,667 A/W. The quantum efficiency also increases to 53,3%. However, extracting detectivity, it is observed that, it has decreased to $2,12 \times 10^{10}$ Jones because of the limiting behavior of the high dark current. 4V reverse bias gives a responsivity of 0.78 A/W and a quantum efficiency of 62.42 %, however the normalized detectivity decreased to 1.35×10^{10} Jones due to high dark currents at this bias voltage.

3.6.4 Results and Discussion

Two different kinds of PbS CQD schottky diodes are implemented on glass, one having aluminum metal to form a schottky barrier and the other using titanium and gold stack. Ti-Au/PbS diode show higher rectification ratios than the Al/PbS one, as shown in Figure 96. The dark current of the Ti-Au/PbS diode is higher than Al/PbS. This high dark current can be attributed to the interaction of PbS–Ti/Al interface. Sputter depositing of Ti is done at higher powers than Al and the higher damage to PbS layer may increase the dark current in the device. On the other hand, Ti-Au/PbS photodiode achieve higher photocurrents than Al/PbS photodiode under same illumination. At 2V reverse bias, Ti-Au/PbS diode responsivity is measured as 0,356 A/W which is higher than the Al/PbS diode that achieves 0.195 A/W responsivity; however, the normalized detectivity of Ti-Au/PbS is $2,25 \times 10^{10}$ Jones, which is lower than Al/PbS diode that has

8.19×10^{10} Jones normalized detectivity because of the high dark current. High dark current limits the sensitivity of the diode. Increasing the reverse bias voltage to 3V in Ti-Au/PbS photodiode the responsivity increases to 0,667 A/W. The quantum efficiency is measured as 53.3 % at 3 V reverse bias. However, extracting detectivity for 3V reverse bias, it is observed that, it has decreased to $2,12 \times 10^{10}$ Jones because of the limiting behavior of the high dark current.

It has been also observed that the lifetime of the Ti-Au/PbS CQD photodiodes is higher than the Al/PbS CQD photodiodes. Al/PbS interface is known to be sensitive to ambient air and oxidation results in doping the PbS layer degrading the performance of the photodiode [64, 65]. Using Au-Ti stack instead of Al improves lifetime of the device by limiting the oxidation of underlying PbS layer. Ti is a low work function metal like Al and Au on Ti decreases the oxidation of Ti layer and hence the underlying PbS layer.

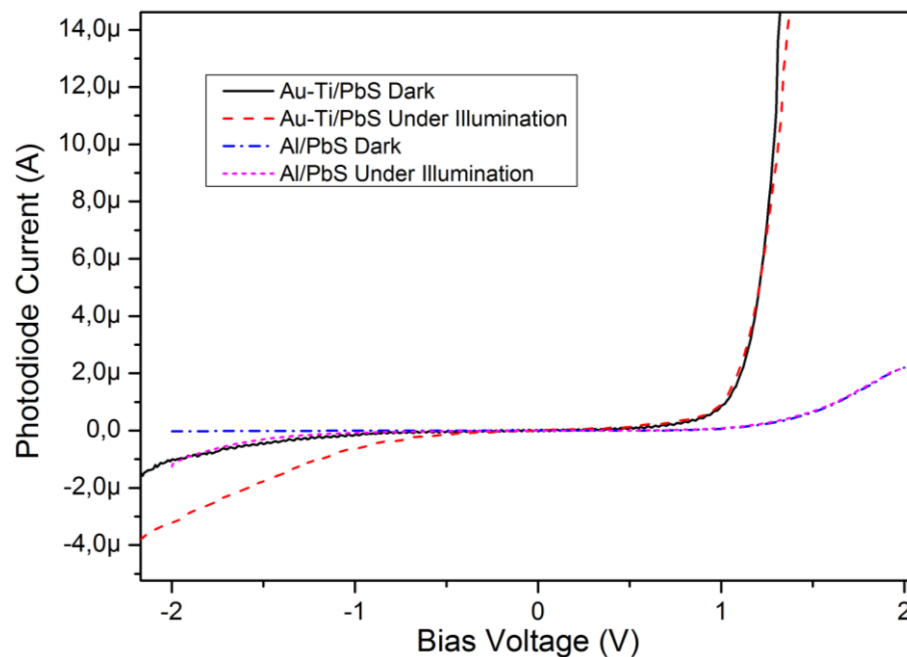


Figure 37. Comparison of dark current and photoresponse of Al/PbS and Au-Ti/PbS schottky photodiodes

Comparison of the photodetectors realized in this work with the state of the art solution based photodiodes is presented in Table 4. Al/PbS CQD photodiode achieves high normalized detectivity of 8×10^{10} Jones at 1550 nm under 2 V reverse bias. This performance is one of the highest normalized detectivity in long wavelengths. The examples in the Table 4 typically achieves high normalized detectivities at shorter

wavelengths however at most of them achieves detectivities lower than 10^{10} Jones even at 1200 nm range. Again the Al/PbS photodiode achieves good efficiency comparing to other examples. In Table 4, efficiency performance, as high as 49 %, can be observed but, this value is achieved at 980 nm wavelength.

Au-Ti/PbS CQD photodiode, on the other hand, achieves very high quantum efficiency and responsivity comparing other examples at high wavelengths. 53.3% is the highest efficiency achieved up to now and additionally it is achieved at 1520 nm wavelength. The responsivity of Au-Ti/PbS follows the same trend with the quantum efficiency and it is the highest one on the list. In addition to this Au-Ti/PbS photodiode achieved 2.12×10^{10} Jones at 1520 nm wavelength that is lower than Al/PbS photodiode due to higher dark currents; however, the normalized detectivity is still higher than most of the examples in the literature. Most of the examples perform high normalized detectivities at shorter wavelengths yet, at higher wavelengths their normalized detectivities fell below 10^{10} Jones.

It can be concluded as, our processing of PbS CQD layers and the solid state ligand exchange together with the optimized photodiode parameters result good efficiencies and responsivities comparing to the solution based photodiodes in the literature. Careful study and optimization of the spin deposition process and ligand exchange is the most crucial part in the way of achieving this. In this work, the processing and ligand exchange procedure carried on in ambient conditions and together with the final annealing step the doping of the PbS layer is stabilized. Direct application of short 3-MPA ligands to the oleic acid capped PbS CQDs, improves the stability of CQDs and improves the carrier mobilities in the film. Optimized steps of layer by layer deposition and the solid state ligand exchange ensures that 3-MPA is successfully replaced the long oleic acid ligands without any residues. Also, as to our knowledge, this is the first time that 3-MPA is applied directly to oleic acid capped PbS CQDs by solid state ligand exchange for SWIR photodiodes.

The high efficiencies achieved in this work is also related with the optimized thickness of the PbS film. Typically, absorbance of PbS CQD layer lies in the range of 10^4 - 10^5 cm^{-1} [31] so thick layers of PbS CQD layers is required to fully absorb the incoming light. However minority carrier diffusion lengths in these layers are around 100 nm and can be increased by correct ligand passivation [31]. So in order to have

moderate absorption and efficient device, together with successful ligand passivation, we also have selected the PbS CQD layer thickness as 250 nm. By applying reverse bias of 2V, which is acceptable for most of the IC processes, the diode is fully depleted and photogenerated carriers drifted by the presence of electric field increasing the quantum efficiency of the PbS CQD photodiodes.

Table 4. Comparison of PbS CQD photodiodes on glass realized in this work with the state of the art solution based photodiodes in the literature

Year	λ (nm)	EQE(%) or R(AW ⁻¹)	D* meas (Jones)	3dB BW (Hz)	Mechanism	Material	Features
2005 [35]	400-700	0.2 % @ 0V, 550nm 15% @ -6V, 550nm	10 ⁸	5x10 ⁴	PD	CdSe quantum dots	Early quantum-photodiode
2009 [43]	Vis-1600	25% @ -1V 12% @ 0V	10 ¹² @ 1450 nm	10 ⁶	PD	PbS QD	Megahertz response in fully depleted photodiode
2009 [44]	Vis-1450	16.5% @ -5V, 1220 nm 0,16 A/W @ -5V, 1220 nm	2.3x10 ⁹ @532nm	2x10 ³	PD	PbS QD +PCBM + P3HT	Integrated into an image array
2009 [45]	Vis-1450	20% at 1100 nm	10 ¹² NIR 10 ¹³ VIS		PD	PDDTT + PCBM	Long-wavelength polymer photodetector
2010 [46]	250 – 1600 nm	24% @ 0V, 980 nm 49% @ -2.5V, 980 nm			PD	PbS QD – C60 Heterojunction	Heterojunction with C60
2011 [47]	Up to 1300 nm	23% 430nm 7% 610nm	4.7x10 ⁹ @ 1300 nm		PD	P3HT:Pbs QD:PCBM blend	Pb QDs with polymer blend
2011 [48]	600-1400 nm	0.2 % at 1100 nm	1x10 ¹¹ @ 1200 nm 1x10 ⁹ @ 1300 nm		PD	TFB+PbSe CQ + ZnO NC	Better dark current perf. With blocking layers
This work Al/Pbs	Vis -1600	15,6 % @ -2V 0.195 A/W @ -2V	8.19 x 10 ¹⁰ @ -2V		PD	PbS QD	High detectivity @ 1550 nm
This work Au-Ti/Pbs	Vis -1600	53.3% @ -3V 0.667 A/W @ -3V	2.12 x 10 ¹⁰ @ -3V		PD	PbS QD	High efficiency, long lifetime

Chapter 4

IC INTEGRABLE PbS CQD PHOTODETECTORS

In the previous chapters, PbS colloidal quantum dot based schottky photodetectors are successfully realized on ITO coated glass substrates. In these photodiodes, we have optimized the PbS layer by layer deposition steps and ligand exchange procedures. Schottky contacts are realized using shadow masks by sputter deposition of metals on PbS CQD layers. Schottky diodes realized by this method achieved good performances such as normalized detectivity of 8.19×10^{10} Jones for Al/PbS photodiode and quite high efficiencies such as 53.3% at 3V reverse bias for Au-Ti/PbS photodiode.

In order to fully integrate these diodes on to read out integrated circuits (ROICs), the processing steps have to be reversed. The idea of fully integration of PbS CQD based photodiodes to ROIC chips centers on using the top metal layer of the IC process as schottky contact. The passivation layer openings will define the diode area and by applying PbS CQDs by spin deposition method and coating a transparent conductive layer on top, we will achieve self-aligned, fully integrated photodiodes on top of ROICs.

So in this chapter, the fabrication process used in chapter 3 will be reversed and optimized. Also, the deposition process of transparent and conductive layers of indium tin oxide will be presented in detail. Taking advantage of these studies, the PbS CQD based photodiodes will be realized on silicon substrates. Also, the chip surface will be mimicked on silicon substrate and the fabrication steps will be optimized on these mimicked substrates. Realized photodetectors will be analyzed and compatibility to ROICs will be discussed.

4.1 Read-out Integrated Circuits Integration

Conventional IR imaging arrays normally composed of crystalline substrates that are different from silicon and they require mechanical bonding with silicon electronics to form the complete imaging array. Therefore, size, yield, reliability and the cost of the bonds between these substrates dominate the size and resolution of these arrays. Solution-processed photodetectors allow monolithic integration of IR sensitive imaging arrays and eliminate the restrictions of these mechanical bonds.

Read-out circuits are realized using well established IC processes. IC process includes active devices (transistors) in the bulk and back-end process which includes a number of metal layers grown on the substrate and electrically isolated with dielectric layers (typically SiO_2). These metal layers are used for signal routing and connecting transistors. In ROICs, pads are placed to the top metal layer and pads are opened on the top dielectric passivation layer in order to allow bonds between ROIC and photodetectors, as shown in Figure 38. Typically flip-chip bonding is used to bond ROICs and photodetectors that are fabricated on different substrates.

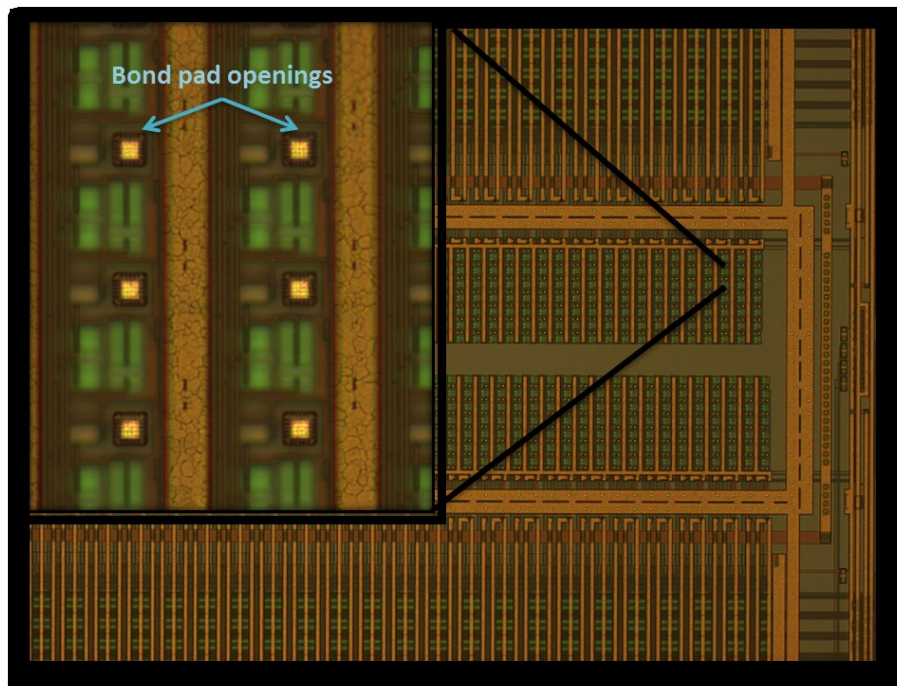


Figure 38. Read-out circuit for FPA integration. Bond pad openings for each pixel is shown on zoomed picture (top left)

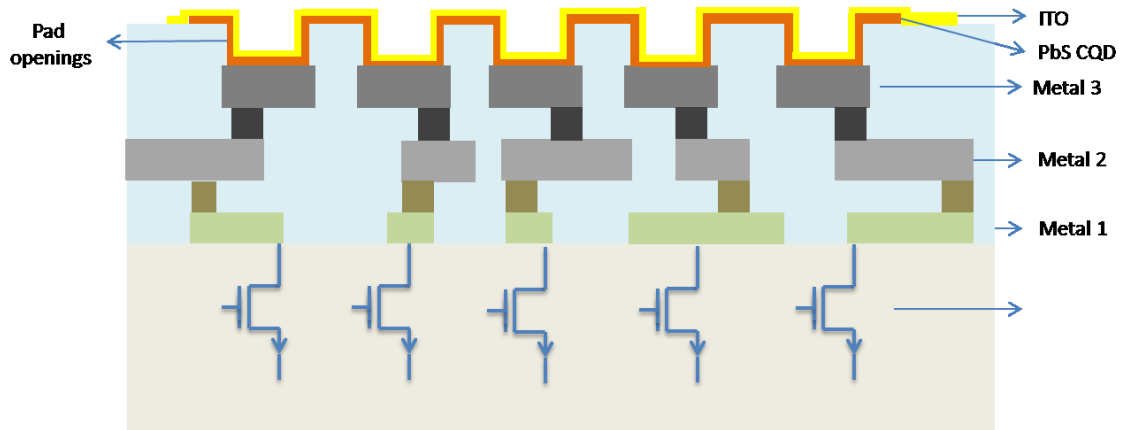


Figure 39. Schematic cross-section of the ROIC and PbS CQD photodetectors integration

Due to the solution based chemistry, PbS CQD can easily be spin coated on the surface of ROIC, forming self-aligned array of photodetectors. The bond pad openings in the ROIC will define the active area of the photodetector and the top metal layer of the ROIC will form the cathode of the photodiode. Addition of a transparent top contact, ITO, will form the anode and the photodetector will be completed. Monolithic integration strategy of the PbS CQD photodetectors is illustrated in Figure 39.

The photodiode formed in Figure 39 is very similar to what we have realized in Chapter 3. However, the fabrication steps are just the opposite of what we have done on glass substrates. So in this chapter, Al/PbS/ITO photodiodes will be realized on Si substrate starting the process from Al layer. Each step will be optimized in this manner taking into account of the integration to ROICs. Special importance is given to the deposition of ITO in this version; such that it will be deposited on PbS CQD layer and it have to be highly transparent and highly conductive.

4.2 ITO Deposition Optimization

ITO has been widely used in many microelectronics applications, such as transparent electrical contacts electrodes in displays, touch screens, thin film solar cells, optoelectronic devices etc. due to its high electrical conductivity and high transparency invisible wavelength range. Its deposition has been presented with many different methods and for many different applications. Typically, magnetron sputtering processes

are performed at high substrate temperatures (≥ 200 °C), as these allow the best results in terms of layer transparency and conductivity to be obtained. However PbS CQD layer is sensitive to high temperatures. Therefore the ITO deposition parameters have to be optimized for room temperature low power deposition for not damaging the underlying layer.

4.2.1 General properties of ITO

Indium Tin Oxide (ITO) thin film is a wide band gap semi-conductor which has good electrical and optical properties including low resistivity, high carrier concentration, high mobility rate and high transmissivity in the visible and near infrared light range (450 nm - 1100 nm). Because of these optical and electrical performances, ITO films had been applied in different fields including solar cells, inorganic and organic light emitting devices, liquid crystal displays, laser diodes and other optoelectronic devices [66-69]. ITO thin films are grown by several deposition techniques such as electron beam evaporation, DC/RF magnetron sputtering, pulsed laser deposition, ion beam deposition, reactive thermal evaporation, spray pyrolysis and chemical vapor deposition [70-77]. Among those, magnetron sputtering method had been the main method for preparing ITO thin films with the following advantages: forming large area films and high deposition rate, suitable for mass production, easy control and reproduction of ITO films thickness as well as no contamination in the sputtering process [78]. For these advantages, ITO layers have been frequently used as front contact or window layer in thin film photodetectors and solar cells devices.

4.2.2 Electrical Properties of ITO

Indium oxide (In_2O_3) is a wide gap semiconductor which has a band gap of 3.75eV [79]. Generally, In_2O_3 crystal structure is not ideal since oxygen vacancies are present. Oxygen vacancies dominate the conduction mechanism of In_2O_3 and the free charge carrier concentration has been reported to be in the range 10^{19} - 10^{20} cm^{-3} . Extrinsic doping can vary the electrical properties of indium oxide significantly. If In_2O_3 is doped with tin atom, tin atoms will replace indium atoms and form tin oxide in either SnO or SnO_2 depending on the valence. If SnO is formed, tin acts as an acceptor since it accepts

an electron. Otherwise, when SnO₂ is formed, it acts as donor since it gives off an electron. Usually, SnO₂ dominates, and tin atoms act as donors. Both tin and oxygen vacancies contribute to the conductivity of ITO.

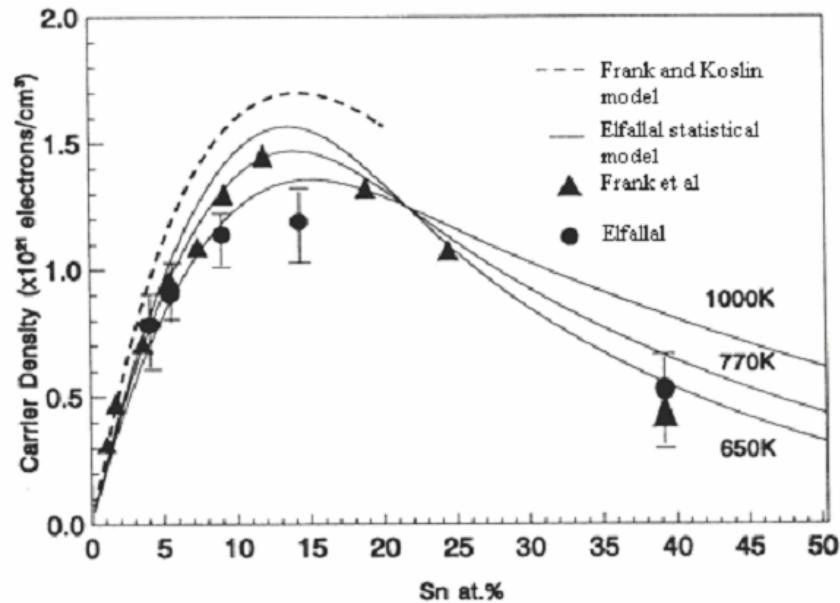


Figure 40. The experimental and calculation of the carrier concentration as function of the tin doping level [80]

The doping level is critical for electrical properties. As the tin concentration increases, the carrier concentration increases until a saturation level is reached. An increase in the tin concentration above this saturation level causes a decrease in the free carrier concentration. This is due to an increased probability of the occupation of adjacent cation positions by two or more tin atoms, which can deplete the active tin concentration [80]. The carrier concentration as a function of tin doping level is well illustrated in Figure 40. The highest carrier concentration, which corresponds to the lowest resistivity, occurs when the tin doping level is about 10%. The solid solubility of tin in indium oxide is approximately 8%. Beyond this range, tin oxide phase will be formed and distort the lattice structure. This will eventually cause a decrease of free carrier concentration. In this work, in order to get conductivity $> 10^3 \Omega^{-1} \text{cm}^{-1}$ and avoid the formation of tin oxide phase, sputter targets composed of 90%_{wt} In₂O₃, 10%_{wt} SnO₂ are used that are supplied by Kurt J. Lesker Company. This doping level will produce degenerative ITO [79].

4.2.3 Sputter Processing of ITO

The glass or silicon samples are cleaned through acetone, methanol, isopropanol and DI rinses in ultrasonic cleaner prior to the deposition. The ITO thin films have been prepared at room temperature (300K) by reactive DC magnetron sputtering from a metallic, In:Sn – 90:10 wt%, 99.99% purity, 2'' diameter, 0.125'' thick, circular targets. The sputter chamber is initially evacuated to a base pressure of 1×10^{-6} mbar. The flow rates of argon (sputter gas) and oxygen (reactive gas) are controlled through independent mass flow controllers. Ar and O₂ flow rates are varied throughout different samples. The chamber pressure, in the presence of sputter and reactive gasses, is adjusted to desired pressure using variable gate valve. The deposition time is generally kept at 10 min, resulting film thicknesses around 240 nm, depending on the power. DC powers from 50W to 350W are applied to different samples but the main intention was to keep power levels low.

4.2.4 Results

A detailed study is carried out on sputter deposition of high quality transparent conductive layers on PbS CQD films and the details of this study is given in Appendix I. It has been observed that higher DC powers results in better conductivity but decreases transmittance. Also, DC power levels above 300W damages the ITO target resulting in cracks on the target. In order to improve the transmittance and conductivity, it has been observed that the main chamber pressure has to be decreased. For that reason, all the ITO sputter deposition processes throughout the work is made at lowest chamber pressure achieved to start the plasma in our sputter deposition system, which is 8×10^{-3} mbar. In order to further increase the transmittance, conventional method is to introduce O₂ gas in the plasma during deposition. However, O₂ in the plasma gas decreases the conductivity of the ITO film. As a solution, O₂ is used in pre sputtering resulting in increased O₂ content in ITO target, and then sputter deposition is carried out using Ar only plasma and O₂ rich ITO target. The optimum pre-sputtering time is found to be 3 min for 10 min sputtering resulting in 230 nm ITO film. We have satisfied the aimed resistivity constraint, $< 1 \times 10^{-3}$ Ω.cm, by achieving $6,25 \times 10^{-4}$ Ω.cm resistivity. Also we have achieved good transmittance at 1450 such as 87,733 %.

Table 5. Summary of sputter deposition parameters and the measurement results of all the samples created

Sample #	Sputter Deposition Process Parameters						Measurement Results				
	DC Power (W)	Variable gate Pos. (/1000)	Pressure (mbar)	Ar/O ₂ Flow (sccm)	Sputtering time (min)	Pre Sputtering	Thickness (nm)	Electrical Resistance (Ω)	Sheet Resistance (Ω/□)	Resistivity (Ω.cm)	Transmittance % @ 1450 nm
1	50	360	1,70E-02	35 Ar	5	same parameters for 3 min	35	1300000	5891600	2,06E+01	100
2	50	360	1,70E-02	35 Ar	25	same parameters for 3 min	118	4300	19487,6	2,30E-01	94,154
3	100	360	1,70E-02	35 Ar	15	same parameters for 3 min	280	942	4269,144	1,20E-01	89,259
4	200	420	7,00E-03	30 Ar	5	same parameters for 3 min	150	25	113,3	1,70E-03	70,616
5	200	410	8,00E-03	30 Ar	10	same parameters for 3 min	330	10	45,32	1,50E-03	47,011
6	200	700	1,10E-02	77 Ar / 5 O ₂	7	same parameters for 3 min	193	228	1033,296	1,99E-02	78,802
7	350	500	8,00E-03	75 Ar / 4 O ₂	3	same parameters for 3 min	150	63	285,516	4,28E-03	88,486
8	150	450	1,05E-02	70 Ar / 2 O ₂	10	same parameters for 3 min	231	38000	172216	3,98E+00	88,234
9	80	360	1,70E-02	35 Ar	5	5 min pre sputtering with 5 sccm O ₂ and 35 sccm Ar	75	520	2356,64	1,77E-02	94,498
10	150	360	1,40E-02	25 Ar	10	3 min pre sputtering with 2 sccm O ₂ and 25 sccm Ar	222	47	213,004	4,73E-03	73,929
11	80	400	1,10E-02	35 Ar	10	3 min pre sputtering with 35 sccm Ar and 5 sccm O ₂ at 1.4e-2 mbar	110	120	543,84	5,98E-03	85,779
12	200	400	1,00E-02	35 Ar	7	3 min pre sputtering with 35 sccm Ar and 5 sccm O ₂ at 1.4e-2 mbar	146	40	181,28	2,54E-03	72,078
13	150	420	8,00E-03	35 Ar	10	3 min pre sputtering with 35 sccm Ar and 2 sccm O ₂ at 1.4e-2 mbar	230	6	27,192	6,25E-04	87,733

4.3 PbS CQD Photodiodes on Si Substrates

4.3.1 PbS CQD Photodiode structure

The designed PbS CQD photodiode shares the same principles of the previously designed photodiodes on glass samples. The structure of the PbS CQD photodiode is shown in Figure 41. PbS colloidal quantum dots with the crystal size of 5.5 nm is also used in this photodiode. Silicon dioxide (SiO_2) layer on silicon wafer serves as an insulation layer between the aluminum back contact and the substrate. Photon sensitive PbS CQD layer is spin coated on Al and schottky barrier is formed between low work function Al and PbS layer.

On the top of PbS CQD layer, a transparent and conductive ITO layer is deposited that serves as an anode. This photodiode is illuminated from the top where the ITO is placed to transmit incoming light to the photosensitive PbS CQD later. The electron and holes are generated at the depletion region between PbS CQD and Al interface and these electrons and holes are collected at Al and ITO contacts respectively.

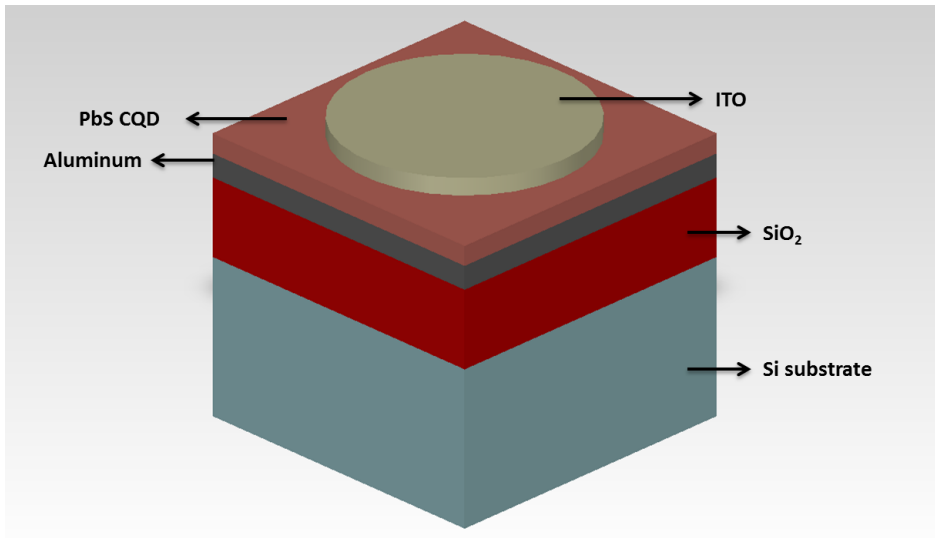


Figure 41. 3D schematic of the PbS quantum dots based schottky photodiode fabricated on Si substrate, composed of ITO anode, photosensitive PbS quantum dot layer and Al schottky cathode

4.3.2 Fabrication Process

The fabrication process of the PbS CQD photodiodes on silicon substrates starts with cleaning the substrates using Acetone, Methanol, Isopropanol and DI baths of 5 min. each in Ultrasonic cleaner and drying substrates using N₂ gun. The Si substrates used in this work is 100 oriented Boron doped silicon wafers with 1 μ thermally grown oxide layer on top. As a next step aluminum layer is sputter deposited on top of oxide layer to form the bottom contact of the photodiode.

DC magnetron sputtering is used to deposit aluminum film on top of oxide. The Al target used in sputtering, which has 2'' diameter, 0.125'' thickness and 99.999% purity, is acquired from Kurt J. Lesker company.. The DC sputtering power is selected as 250 W, Ar flow for the plasma is set to 35 sccm and the position of the variable gate valve is set to 360/1000 to achieve 1.7×10^{-2} mbar chamber pressure during sputtering. Using the same parameters, first pre-sputtering is run for 3 min in order to condition the chamber and to clean the target. Following that, aluminum sputtering process is run for 15 min. resulting 250 nm thickness. The sheet resistance of the Al layer is measured as 129 m Ω /□ by Cascade C4P 4-point-probe system.

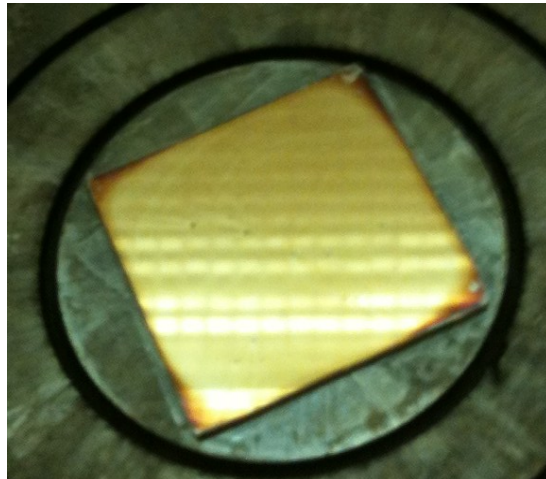


Figure 42. PbS CQD layer on top of Al coated Si/SiO₂ substrate during layer by layer deposition process that takes place on spin coater. The layer has a shiny and yellowish/light brown color

Following Al deposition as bottom contact, PbS CQD is coated using step by step spin coating technique which is explained in detail in section 3.3. Layer by layer spin

deposition method results in pinhole and crack free, shiny films on aluminum. Figure 42 shows the picture of PbS CQD layer on top of Al coated Si/SiO₂ substrate during layer by layer deposition process that takes place on spin coater. The layer has a shiny and yellowish/light brown color. Thickness of PbS layer is kept at 250 nm for optimum absorption and diffusion lengths.

The solid state ligand exchange procedure is applied during the layer by layer spin coating process. Long oleic acid ligands were removed by methanol and they are replaced by 3-MPA. The solid state ligand exchange procedure is described in detail in section 3.4

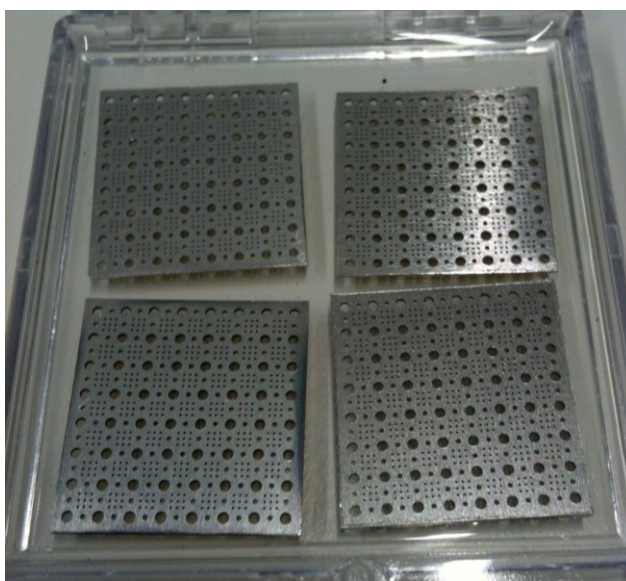


Figure 43. 20mm x 20 mm size aluminum sheet hard masks that have 0.4 mm diameter holes on them.

After the PbS CQD layer is deposited, the samples are prepared for ITO deposition is PVD tool. In these samples, shadow masks are used in order to define the ITO area, and thus the photodetector area. The hard masks are prepared using Kern-Evo precision drilling equipment and 0.4 mm holes are opened in 20 mm x 20 mm size thin aluminum sheet. The hard masks used are shown in Figure 43. When placing of wafer holder of the sputter system, the hard mask is fixed to the surface of the sample. The ITO deposition optimization is given in detail in section 4.2. 150 W DC power is used in sputtering. The ITO target (90%wt In₂O₃, 10%wt SnO₂, 2'', Kurt J. Lesker) is oxidized during 3 minute pre-sputtering process that is done with 150 W DC power, 35

sccm Ar flow, 2 sccm O₂ flow, 1.4 x 10⁻² mbar chamber pressure. Then 10 minute sputtering is carried out using the same power and Ar flow, but closing the O₂ flow and decreasing the chamber pressure to 8 x 10⁻³ mbar by setting the variable gate valve position to 420/1000. Resulting ITO thickness is measured as 230 nm.

4.3.3 Measurement Setup

Since the dimensions of the photodiodes are relatively small, the electrical and optical characterizations are carried out in Cascade PM5 DC probe station using tungsten needles. The probe station is equipped with a shielded enclosure which is used for dark current measurements. The probes are used to take contact from the top ITO layer and bottom Al Schottky contact. For dark current measurements and I-V characterization, probes are connected to Agilent Semiconductor Parameter Analyzer.

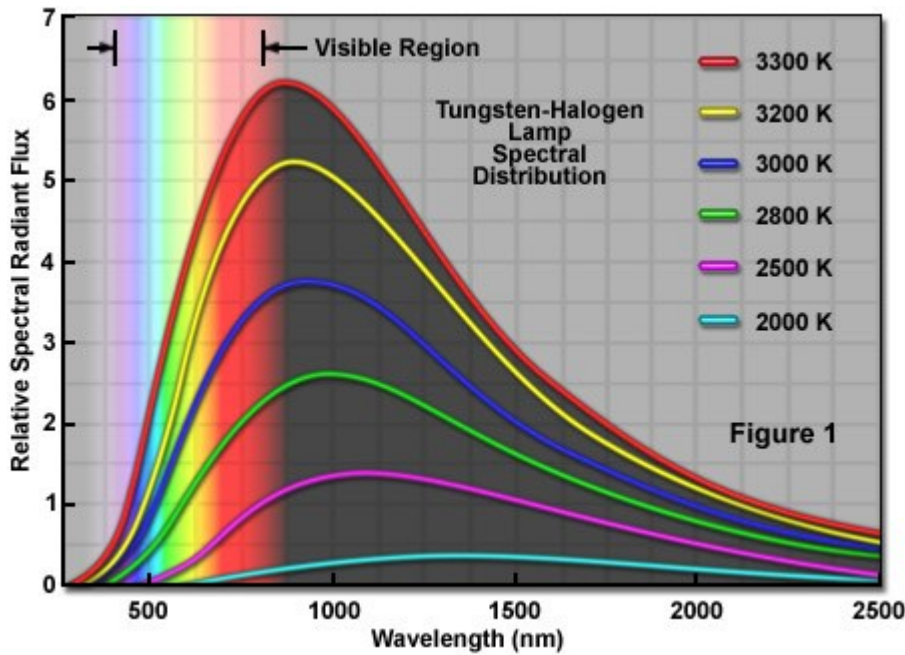


Figure 44. Tungsten-Halogen lamp spectral distribution [81]

The test setup is very similar to the setup used in testing PbS CQD photodiodes on glass samples. Unlike photodiodes on glass samples, this time, the samples are illuminated from the top, through the ohmic ITO contact. For illumination Motic MLC-150C Cold Light Source is used. Motic MLC-150C uses 21V/150W EKE Halogen

Lamp for the light source. Also the color temperature, hence illumination power can be adjusted with a knob on Motic MLC-150C.

The irradiance of the illumination on sample is calibrated using Thor Labs PM100 Optical Power Meter System. The Germanium (Ge) detector of Optical Power Meter System is put in place of the Al/PbS detector on the chuck and then the power is measured at different wavelengths for color temperatures ranging from 3200 K to 2400 K.

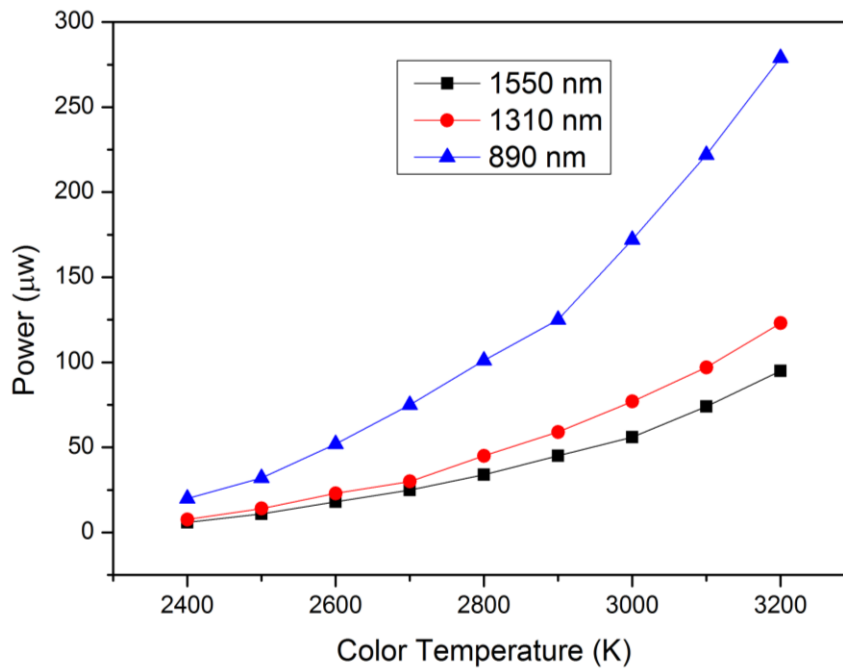


Figure 45. The graph of the illumination power measured by optical power meter system at 1550 nm, 1310 nm and 890 nm wavelength, with respect to different color temperature adjusted by Motic light source.

4.3.4 Measurement Results

Al/PbS photodiode is fabricated using the fabrication steps that are described in previous chapter. The process is started by cleaning the $1\mu\text{m}$ oxide deposited silicon substrates using acetone, methanol, isopropanol and DI water baths for five minutes each in the ultrasonic bath. Al is deposited on the sample by DC sputter deposition. After 250 nm Al is deposited with the parameters given in section 5.2.2, the PbS CQD

layer is spin deposited on the sample. The layer by layer deposition process together with ligand exchange procedure is applied as follows;

1. 0.2 mL PbS in toluene is dropped on surface and spinned at 2500 rpm for 15 sec.
2. 0.4 mL of 3-MPA/methanol solution (1:10) is dropped on surface and spinned at 2500 rpm for 15 sec.
3. 0.8 mL methanol is dropped on surface and spinned at 2500 rpm for 45 sec.
4. 0.8 mL toluene is dropped on surface and spinned at 2500 rpm for 45 sec.
5. Sample is spin dried at 2500 rpm for 45 sec.
6. Steps from 1-5 is repeated 9 times.

Following PbS CQD layer coating, the sample is annealed in ambient environment for 5 min at 100 °C on hot plate. Then the sample is placed on wafer holder of sputtering equipment with the hard mask and ITO is sputter deposited with the parameters given in previous section.

As a first step, the photodiode is placed in Probe station and connected to Agilent Parameter Analyzer to measure current voltage diode characteristics under dark. The enclosing shield is closed while making measurements in order to block the surrounding light. The bias voltage is applied to Al contact and swept from -2 V to 2 V and diode currents are measured for each applied bias voltage. The resulting I-V graph of Al/PbS schottky diode is given in Figure 46.

Under dark, the sample shows typical diode behavior, and achieves rectification over 14 between $\pm 2V$. The dark current at -1V is 1.9 nA, and 4.3 nA at -2V, which is better than the version that is built on glass in chapter 3 Also, it should be noted that the reverse breakdown of this diode occurs at 4V reverse bias.

As a next step the sample is tested under illumination. The probes are connected to Semiconductor Parameter Analyzer and firstly, I-V measurement for $\pm 2V$ is taken under dark conditions at room temperature. After that the detector is illuminated from top with Motic Light Source. In addition to this, the illumination irradiance on sample is calibrated using ThorLabs PM100 Optical Power Meter System. The Germanium (Ge)

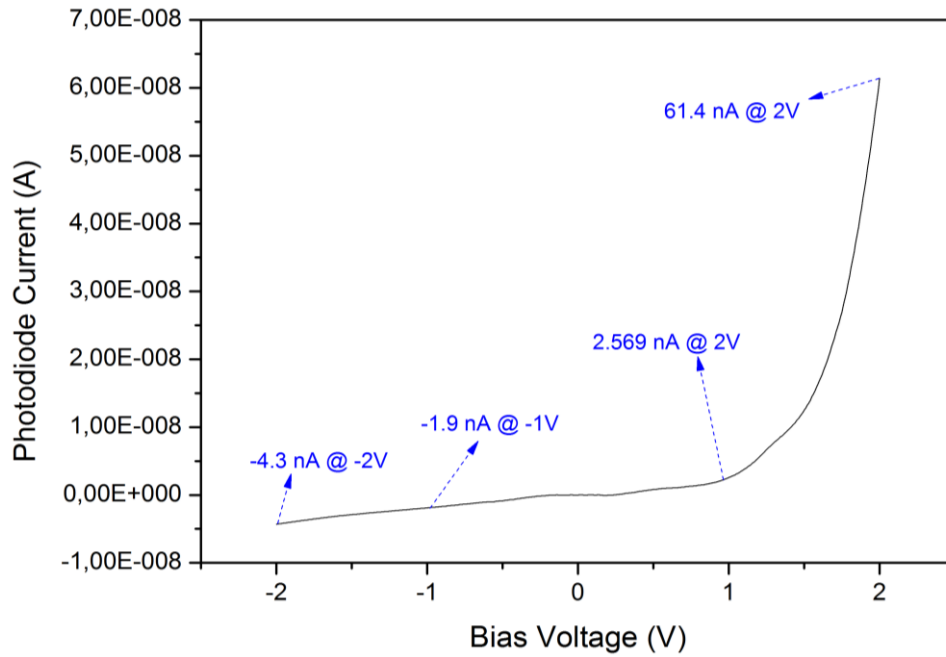


Figure 46. I-V graph of Al/PbS photodiode on Si substrate under dark. Rectification over 10 is achieved between $\pm 2V$

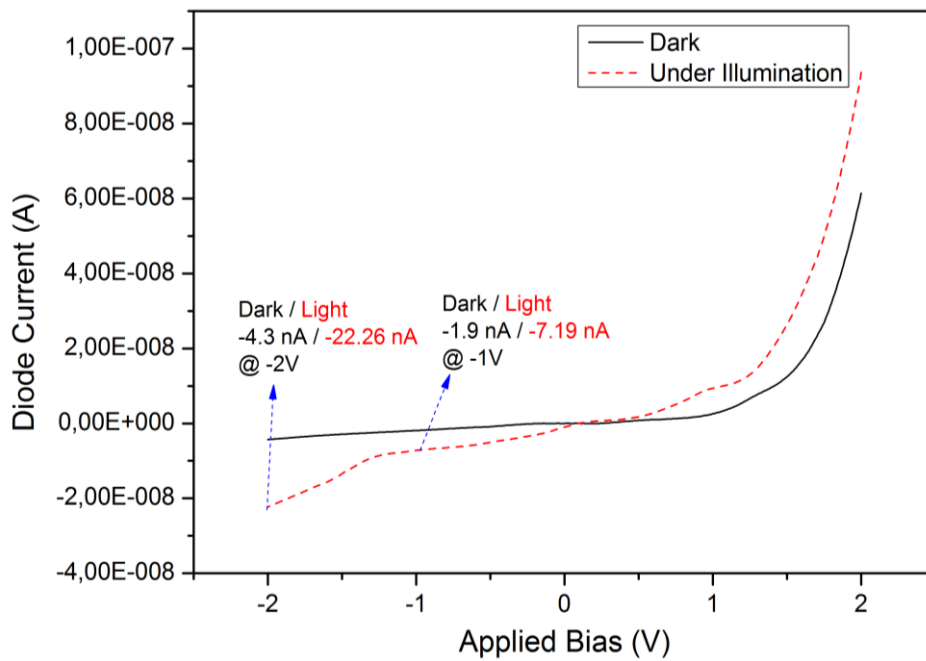


Figure 47. I-V curves of Al/PbS CQD schottky photodiode under dark (black curve) and under $140 \mu W/cm^2$ illumination (red curve)

detector of Optical Power Meter System is put in place of the Al/PbS detector on the small optic table and then the power on the PbS detector is estimated from the power

reading on the reference detector. It is found to be that the Al/PbS detector is illuminated with $140 \mu\text{W}/\text{cm}^2$ at 1550 nm wavelength.

The current characteristics depending on applied bias in both dark and when exposed to $140 \mu\text{W}/\text{cm}^2$ illumination at 1550 nm is given in Figure 47. At 1 V reverse bias, the dark current is 1.9 nA and the current under illumination is 7.19 nA that shows approximately 4 fold increase in current. The responsivity achieved at 1 V reverse bias is 0.12 A/W which is moderate and the quantum efficiency of the device is found to be 9.43% . The normalized detectivity is calculated with the assumption that shot noise is dominating the total noise of the detector and it is calculated as $8,47 \times 10^{10}$ Jones.

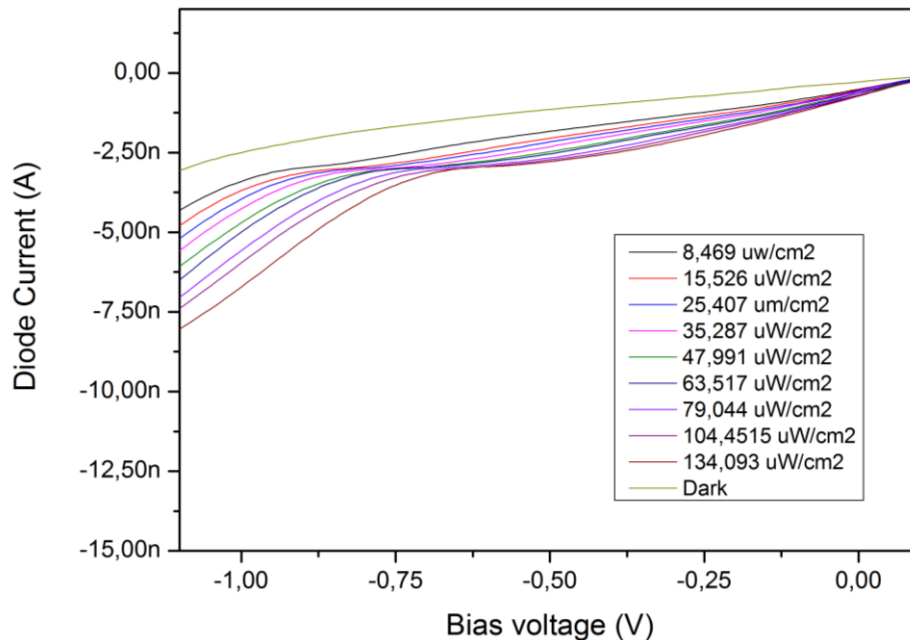


Figure 48. Bias voltage vs diode current graph for irradiance between $8,469 \mu\text{W}/\text{cm}^2$ and $134,093 \mu\text{W}/\text{cm}^2$.

Under 2 V reverse bias voltage, the dark current increases to 4.3 nA ; however, the photocurrent also increases to 22.26 nA , which presents around 5 fold increase. The responsivity achieved under 2 V reverse bias is $0,4 \text{ A/W}$ and the quantum efficiency is extracted as 32% . With the assumption of shot noise is dominating the noise-current, the detectivity is calculated as $1,91 \times 10^{11}$ Jones. Comparing with the Al/PbS device on glass substrates that are realized in Chapter 3, this version achieves better detectivity

depending on decreased dark current. The reason of better dark current performance is related with the schottky metal – PbS CQD layer interface. In glass substrate samples, the schottky metal is deposited using sputter deposition which damages the PbS CQD film, thus damages the PbS CQD film – schottky metal interface. In the samples that are realized on Si substrate, first, schottky metal is deposited and then PbS CQD layer is spin deposited on it. This results in better interface between PbS film and metal without damaging the PbS film.

As a next step the correlation between the photoresponse on the reverse bias and irradiance is measured. The irradiance is changed between $8,469\mu\text{W}/\text{cm}^2$ and $134,093\mu\text{W}/\text{cm}^2$ and the diode current behavior in the reverse bias is observed. Figure 48 shows the photocurrent change around 1V reverse bias due to the irradiance change and it can be seen that with increasing irradiance, the photocurrent of the diode increases. The correlation between irradiance and photocurrent is clearer in Figure 49 where the photocurrent change due to the irradiance is drawn for 1V reverse bias. The photoresponse is linear over irradiance change from $8,469\mu\text{W}/\text{cm}^2$ to $134,093\mu\text{W}/\text{cm}^2$.

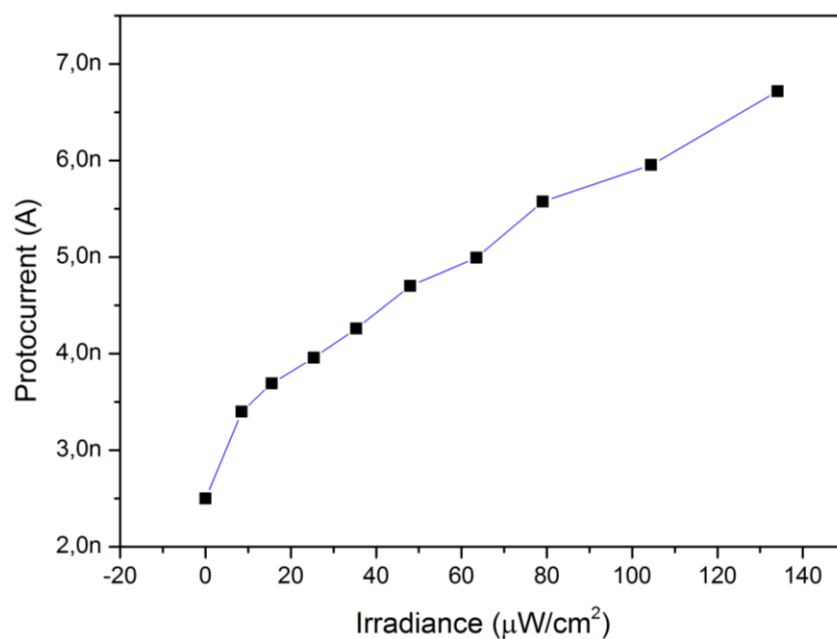


Figure 49. Photocurrent change depending on irradiance measured under 1V reverse bias. Linear behavior is observed from $8,469\mu\text{W}/\text{cm}^2$ and $134,093\mu\text{W}/\text{cm}^2$

4.4 PbS CQD Photodiodes on Mimic of ROIC

In previous chapter, we have realized Al/PbS photodiodes on silicon substrates, in the order of first, forming Al electrodes on Si/SiO₂ samples, then coating PbS layer and finally depositing transparent conductive ITO on top; for the first time as to our knowledge. We have observed performance increase comparing to Al/PbS photodiodes that are fabricated on glass samples, which is also discussed in chapter 3.

In this chapter, in the direction of fully integration of PbS CQD photodiodes on read out electronics that are fabricated using conventional Si CMOS processes; we fabricated mimics of top layers of ROICs on Si substrates and fabricate our PbS Schottky diodes on top of them. This work presents a proof of concept of fabricating PbS CQD photodiodes to ROICs in order to have monolithically integrated SWIR detector. The procedure is shown in Figure 50.

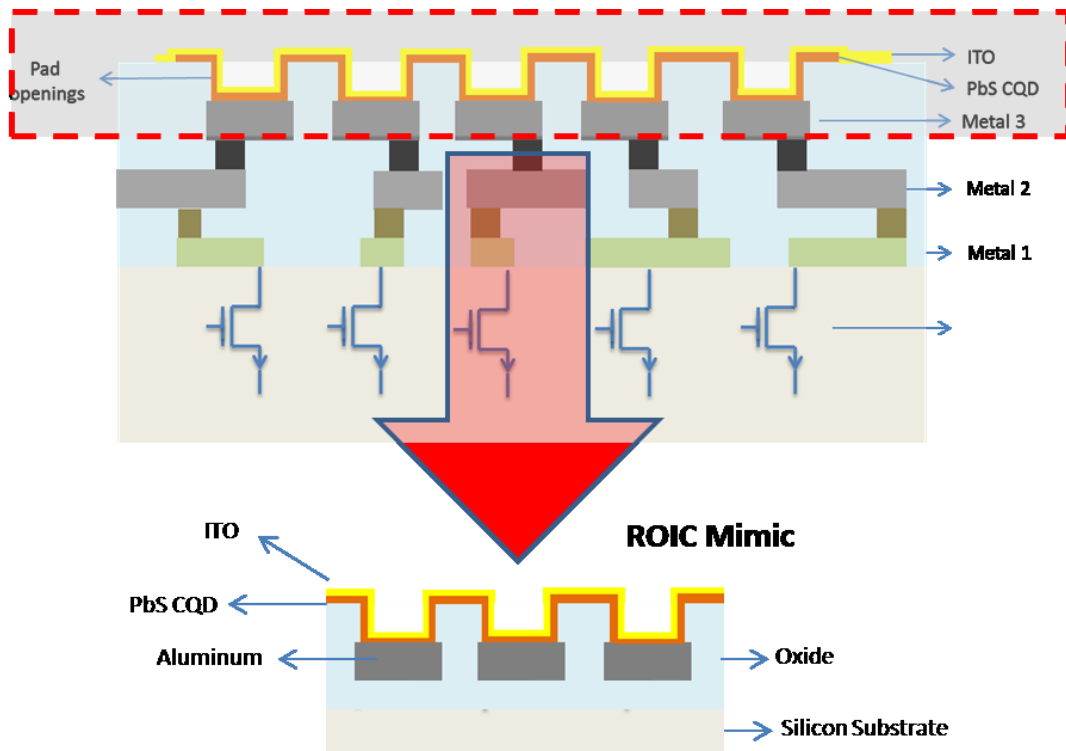


Figure 50. Schematic of mimicking the top layer of ROIC and fabricating PbS photodiodes in order to test integration

4.4.1 ROIC Mimic

In order to mimic the pixels of the ROIC, the surface of the ROIC is analyzed and the pixel sizes and pixel spacing are measured. After that same sizes is used to design the mask that will be used creating mimic chip. The bond pad openings, which defines the photodiode are in monolithically integrated photodiodes, have the area of $5\ \mu\text{m} \times 5\ \mu\text{m}$. The vertical spacing of pixels are $33\ \mu\text{m}$ from center to center and horizontal spacing is $40\ \mu\text{m}$ from center to center. The photography and dimensions of the bond pad openings on ROIC is shown in Figure 51. For the mimic chip, 3×2 pixel array with the diode areas $5\ \mu\text{m} \times 5\ \mu\text{m}$ is drawn together with oxide openings, ITO layer, and the pads connected to the anode and cathodes. The layout is also shown in Figure 52. Red lines defines Al pads, green lines are for oxide openings, yellow is the mask to define PbS area and blue lines stands for ITO layer.

4.4.1.1 Fabrication steps of PbS CQD photodiodes on ROIC mimic

The fabrication of PbS CQD photodiodes on ROIC mimic starts with cleaning of Si substrates with $1\ \mu\text{m}$ thermally grown oxide on them (step (a) in Figure 53). Al is deposited using DC magnetron sputtering from an Al target which is shown in step (b) of Figure 53. Deposition takes place with 250 W DC power and 35 sccm Ar flow in the chamber with the pressure of 1.7×10^{-2} mbar. 15 min deposition resulted in 250 nm Al film. The next step, Figure 53 step (c), is patterning the Al layer with our first mask in order to mimic the top metal layer of ROIC chip. HPR 504 photoresist is spin coated with the process of spinning at 500 rpm 5 sec. for spreading and then spinning at 4000 rpm for 45 sec. for coating the sample with $1,25\ \mu\text{m}$ PR. Then, the sample is soft baked at $110\ ^\circ\text{C}$ for 1 min. and exposed 35 sec. in Karl Suss contact aligner using our 1st mask. PR is developed for 35 sec. and finally hard bake takes place at $120\ ^\circ\text{C}$ for 1 min. After PR is patterned, Al is dry etched using Oxford Plasma Lab 100 ICP/RIE tool using a Cl based recipe. 30 sccm C_2 and 30 sccm BCl_3 is used in the process. The chamber pressure is adjusted to 5mTorr and 100W RF and 1000W ICP power is used. The recipe is run for 1 min and etched the Al layer completely. After that the remaining resist is removed by acetone rinse for 5 min and then applying O_2 plasma (Figure 53 step (d)). Microscope picture of resulting patterned Al bottom contacts is shown in Figure 54.

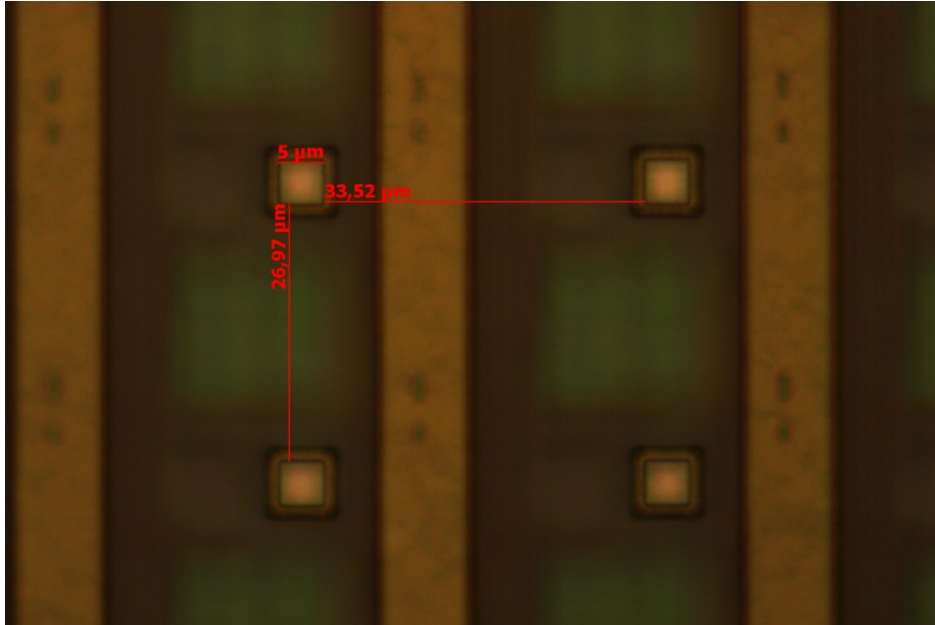


Figure 51. Size and spacing of pixels measured from ROIC chip. The bond pad openings are $5\ \mu\text{m} \times 5\ \mu\text{m}$ and the vertical spacing of pixels are $33\ \mu\text{m}$ from center to center and horizontal spacing is $40\ \mu\text{m}$.

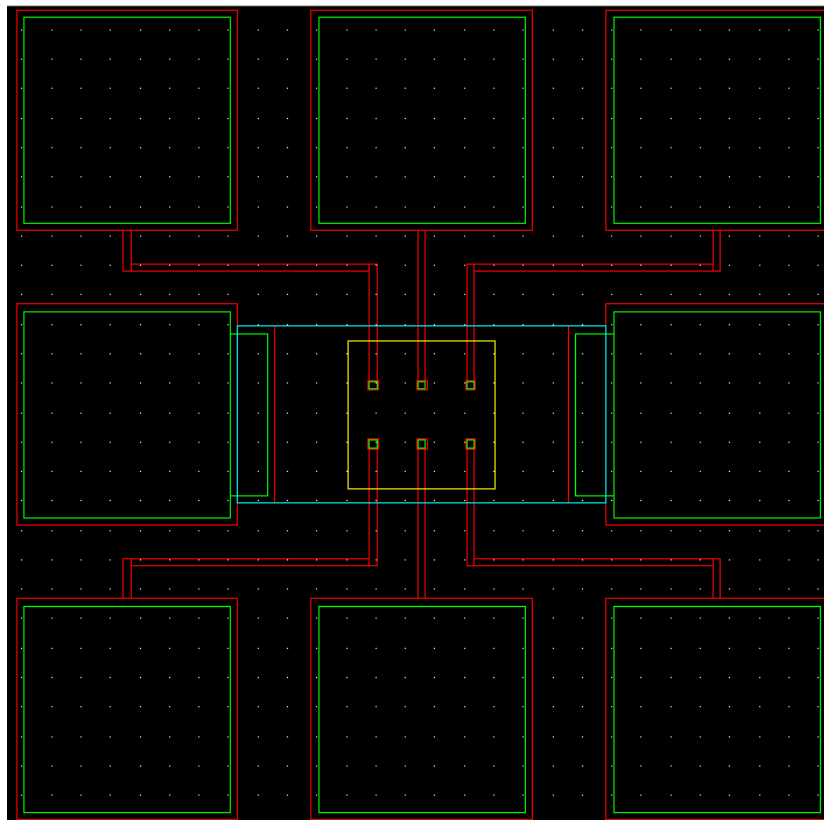


Figure 52. The mimic chip layout for 2×3 pixel array with the size of $5\ \mu\text{m} \times 5\ \mu\text{m}$. Pads are connected to each pixel for testing.

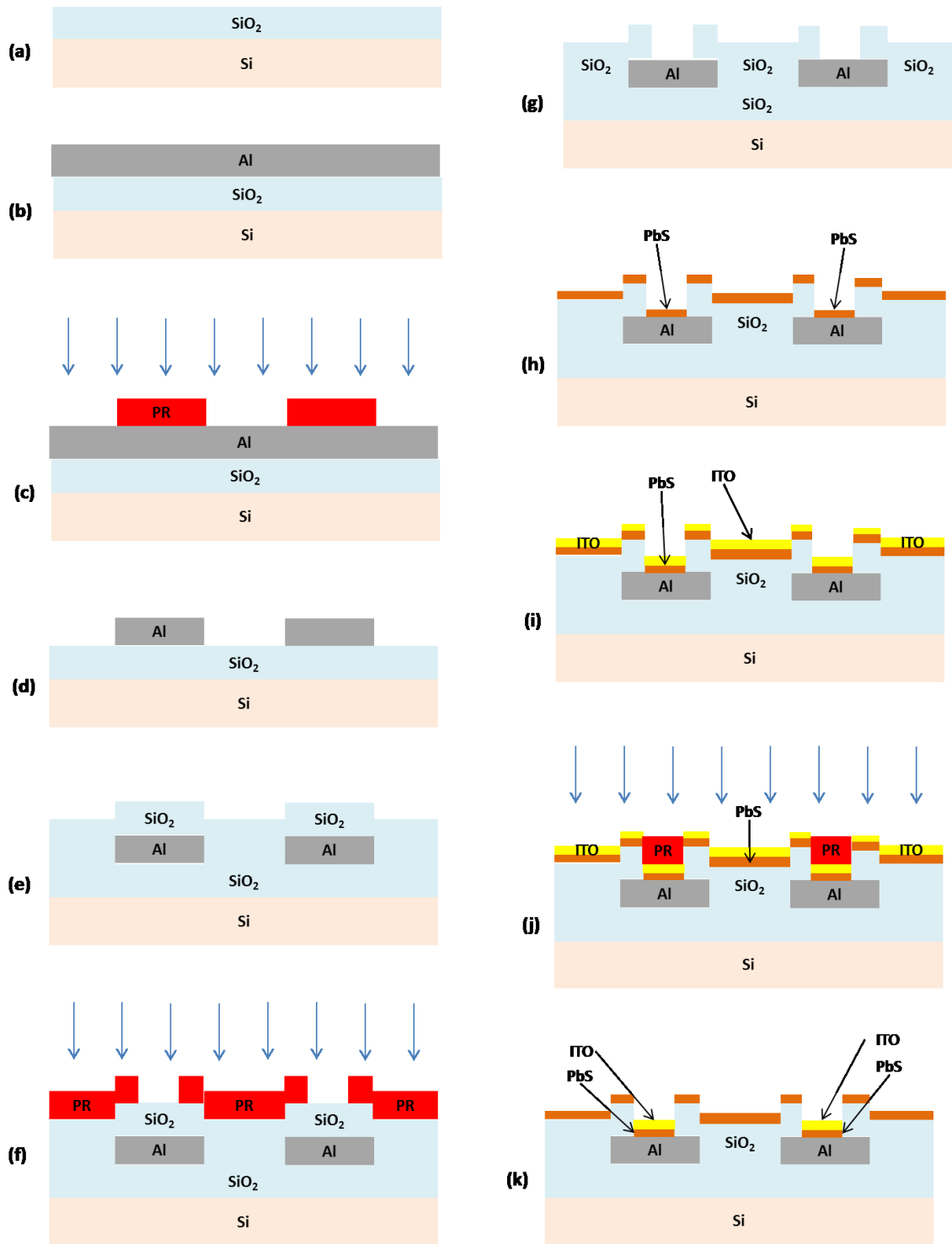


Figure 53. Fabrication steps of PbS CQD photodiodes integrated on ROIC mimic

Next step is to deposit oxide layer on top of Al contacts and then to open the bond pad openings such like the top passivation oxide layer of ROIC chips. Oxford Plasma Lab 80 PECVD tool is used to deposit 0,8 μm oxide layer which is shown in Figure 53 step (e). The deposition is carried out using 150 W RF power and 400 sccm SiH₄ (5% in N₂)

and 1000 sccm N₂O flow. Deposition rate was 160 nm/min and 5 min deposition resulted in 800 nm oxide thickness. Then the oxide layer is patterned using HPR 504 resist using exactly same steps as it is done in Al layer which is illustrated in in Figure 53 step (f). Following the patterning, the sample is put into Oxford Plasma Lab System 100 for a dry etch process. RIE only recipe is used for SiO₂ etching. CHF₃ and Ar gases used during process with 35 sccm and 75 sccm flows respectively. The chamber pressure is kept at 30 mTorr during process and 150 W RF power is applied. The etch rate was 80 nm/min and 10 min etch completely removed the oxide layer. Next, PR is removed with acetone bath and O₂ plasma and the pad openings on Al are achieved as shown in Figure 53 step (g). Microscope picture of the resulting layer is shown in Figure 55. At this point, we have the mimic of the top layers of ROIC.

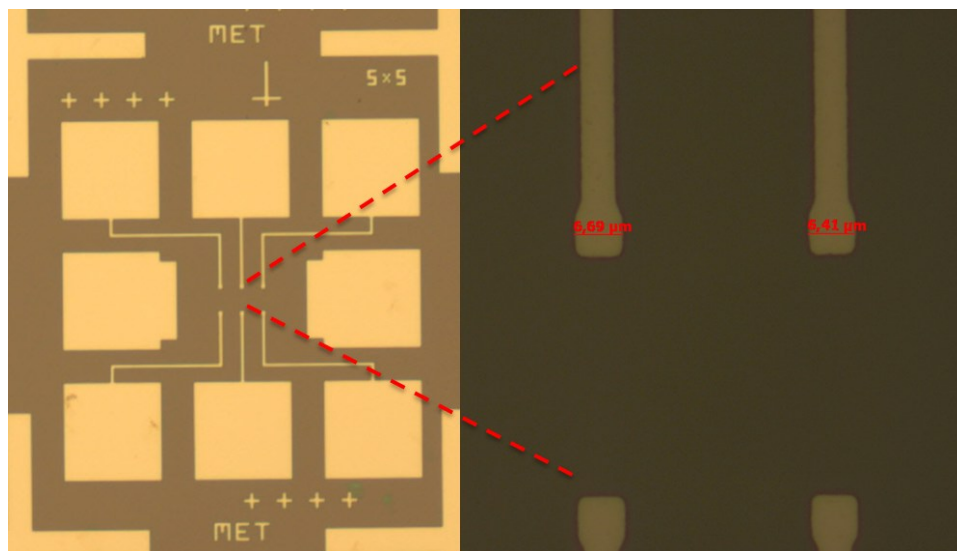


Figure 54. Microscope picture of patterned bottom Al contacts. The bottom contact has a size of 6,5 μm x 6,5 μm.

In Figure 53 step (h), our integrated PbS CQD diode process starts by spin casting PbS layers on the surface of ROIC mimic. Layer by layer deposition and ligand exchange procedures is applied as previously done in section 5.2.4. Following this ITO is deposited on top of PbS layer. The optimized process of ITO DC sputter deposition is used in this process. Pre-sputtering is done at 150 W DC power with 35 sccm Ar and 2 sccm O₂ flow with a chamber pressure of 2×10^{-2} mbar. Following this sputtering is carried out at 150 W with only Ar gas present in the chamber which has a flow of 35 sccm and under 8×10^{-3} mbar chamber pressure. The deposition takes 10 min resulting

~230 nm thick ITO films (Figure 53 step (i)). For patterning ITO films PR mask is applied covering the areas that forms the top contact as shown in Figure 53 step (j). After that the ITO is dry etched in Oxford Plasma Lab 100 ICP etcher using a CH₄/H₂ chemistry with an etch rate of 80 nm/min. The process parameters in ITO etching is selected as 50 sccm CH₄ flow, 20 sccm of H₂ flow, 10 mTorr chamber pressure, 1000 W ICP power, 200 W RF power, temperature 60°C and backside helium pressure of 10 Torr. After ITO etching the PR is removed using acetone rinse and a short O₂ plasma. The microscope picture of the sample after ITO etch is shown in Figure 56.

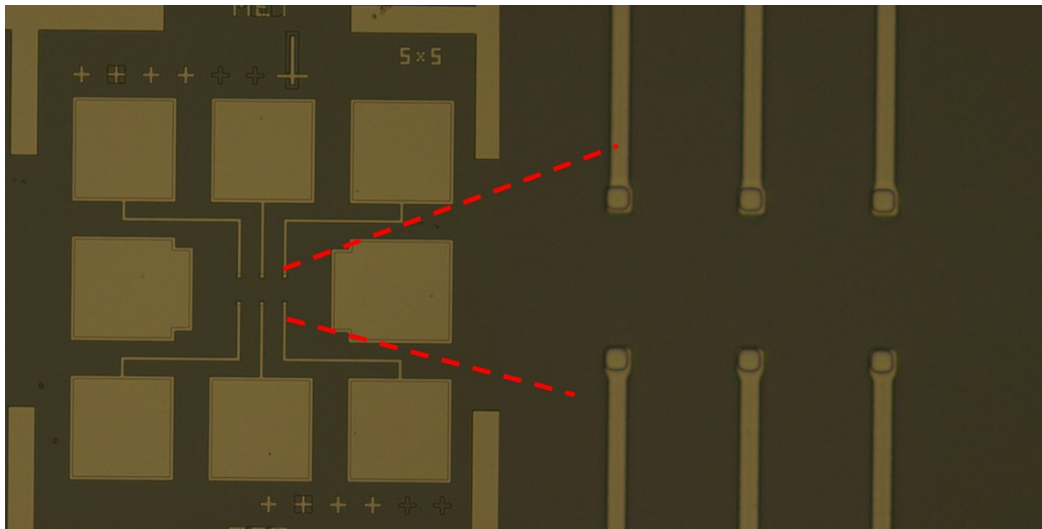


Figure 55. Microscope picture of the oxide over the Al layer is patterned and the bond pond areas left open which defines the photodiode area.

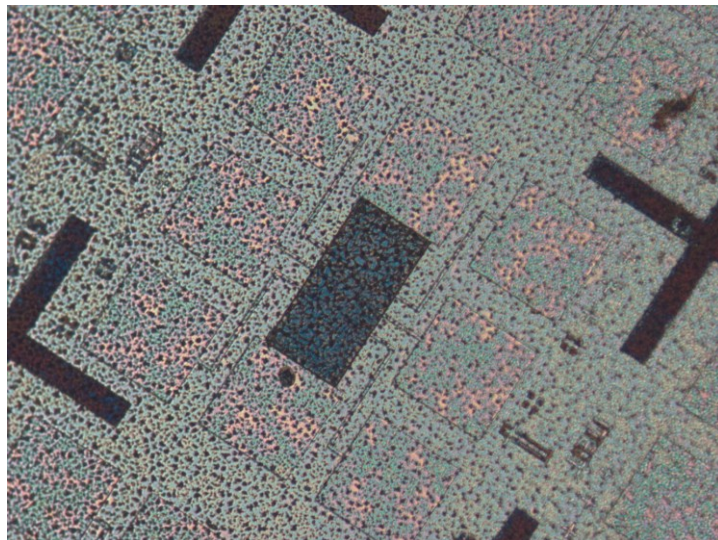


Figure 56. PbS diode picture after ITO etch.

4.4.2 Test Setup and Measurements of PbS CQD photodiodes on ROIC mimic

After the fabrication is completed, the PbS CQD photodiodes on ROIC mimic are tested using similar test setup of our previous measurements. Agilent Parameter Analyzer is used for I-V measurements. Cascade PM5 probe station with a dark enclosure is used to probe the photodiodes and do the dark current measurements.

First the bias voltage is applied to Al contact and swept from -2 V to 2 V without any illumination and diode current are measured for each applied bias voltage. Figure 57 shows the I-V graph of PbS CQD under dark conditions. From the graph, the diode behavior can be observed, however the rectification ratio was low as 1.45 at ± 1 V and 2 at ± 1 V.

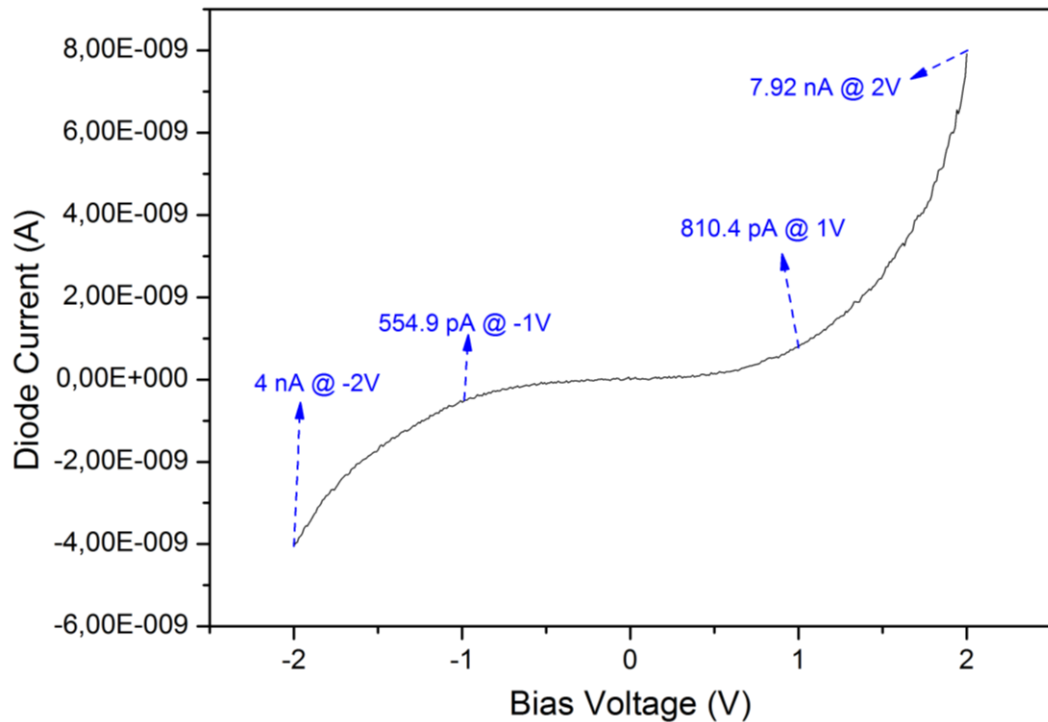


Figure 57. I-V characteristics of PbS CQD diode under dark.

Following that the sample is tested under illumination. The probes are connected to Semiconductor Parameter Analyzer and firstly, I-V measurement for ± 2 V is taken under dark conditions at room temperatures. After that the detector is illuminated from top with Motic Light Source. In addition to this, the illumination irradiance on sample is calibrated using ThorLabs PM100 Optical Power Meter System. The Germanium (Ge)

detector of Optical Power Meter System is put in place of the Al/PbS detector on the small optic table and then the power on the PbS detector is measured from the power reading on the reference detector. It is found to be that the Al/PbS detector is illuminated with $140 \mu\text{W}/\text{cm}^2$ at 1550 nm wavelength.

The current characteristics depending on applied bias in both dark and when exposed to $140 \mu\text{W}/\text{cm}^2$ illumination at 1550 nm is given in Figure 58. The red curve on the graph represents the diode current under illumination and the black curve represents the dark current. At 1 V reverse bias, the dark current is 555 pA and the current under illumination is $2,86 \text{ nA}$ that shows approximately 5 fold increase in current. The responsivity achieved at 1 V reverse bias is 0.205 A/W and the quantum efficiency of the device is found to be 16.4% . With the assumption of shot noise dominating the noise current, the normalized detectivity is calculated as $1,36 \times 10^{11}$ Jones at 1 V reverse bias.

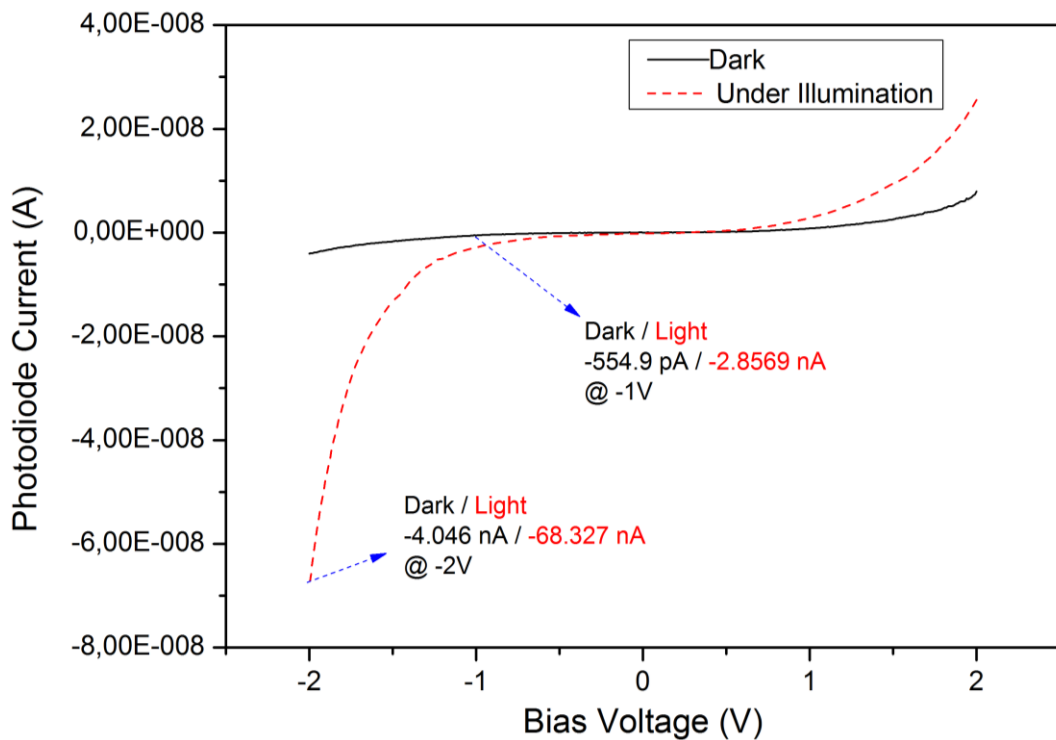


Figure 58. I-V characteristics of the sample under dark and under $140 \mu\text{W}/\text{cm}^2$ illumination.

Under 2 V reverse bias voltage, the dark current increases to 4.05 nA , however the photocurrent also increases to $68,3 \text{ nA}$ which presents around 16 fold increase. The

responsivity achieved under 2 V reverse bias is 5,73 A/W. With the assumption of shot noise is dominating the noise-current, the detectivity is calculated as $1,41 \times 10^{12}$ Jones.

4.5 Results and Discussion

In this chapter we have fabricated PbS CQD photodiodes on silicon substrates and also on the mimics of the ROICs. In terms of integration, it is crucial to realize them in this manner, because monolithic integration is the most important advantage of solution based photodetectors. First, PbS CQD photodiodes are realized in reverse order of the fabrication steps of the diodes realized on glass substrates, previously. In this kind of photodiodes, achieved rectification was smaller than the counterparts that are implemented on glass substrates. However, the dark current performances of these devices were better than the versions on glass substrates and are on the order of 400 pA. This low dark current is correlated with the reverse fabrication steps such as; while fabricating on glass the schottky metal is sputter deposited on PbS CQD film damaging it and the interface between the film and the metal; however, while realizing photodiodes on silicon, the PbS layer is spin deposited on schottky metal and the interface between film and metal is not affected by plasma deposition.

The PbS CQD photodiode achieved 0,4 A/W responsivity under 2 V reverse bias voltage. The quantum efficiency is extracted as 32 %. With the assumption of shot noise is dominating the noise-current, the detectivity is calculated as $1,91 \times 10^{11}$ Jones. Comparing with the Al/PbS device on glass in chapter 3, this version achieves better detectivity depending on decreased dark current.

In addition to this, in order to estimate the monolithically integrated PbS CQD photodiodes to read-out integrated circuits, a mimic of ROICs top layers are realized on silicon substrates. Al contacts are formed, which is the replica of ROIC's pixel structure realized by the top layer of the IC process. Then the sample is coated with SiO₂ which is similar to the passivation oxide on the ROIC. Finally, 5 μm x 5 μm vias are opened in oxide on Al contacts to create a replica of the bond pad openings on the ROIC which defines our active photodiode area. After that the optimized PbS CQD layer deposition and ITO top contact formation realized.

The rectification in this monolithically integrated PbS CQD photodiodes was low as 1.45 at ± 1 V and 2 at ± 2 V under dark conditions.. The dark current performance of these diodes was good such as, they achieved dark currents in the range of 400 pA at 1V reverse bias. PbS CQDS photodiodes on ROIC mimics achieved 0.2 A/W responsivity and 16.4% quantum efficiency at 1V reverse bias. Increasing the reverse bias to 2V, the photodiodes behave more like a photoconductor giving a responsivity of 5,73 A/W. This high responsivity is a result of gain which is characteristic behavior in photoconductors. Also these detectors achieved very high normalized detectivities such as; 1.36×10^{11} Jones and 1.42×10^{12} Jones under 1V and 2V reverse bias respectively. These results are quite good and can be comparable with InGaAS SWIR detectors that nominally have detectivities around 10^{12} Jones at room temperatures.

Looking to the photoresponse of these detectors, as seen in Figure 58, it can be observed that under increased reverse bias the photoresponse increases enormously. But also in forward bias, we have observed an increase in the current under illumination. This behavior implies that these integrated PbS CQD photodetectors works more like a photoconductor. This can be also related to low rectification characteristics. The poor schottky barrier results in the device to enter a photoconductive mode that is formed vertically of Al/PbS/ITO.

Table 6 presents the comparison of PbS CQD photodiodes on glass, silicon and ROIC, which are realized in this work, with the state of the art solution based photodiodes in the literature. Al/PbS CQD photodiodes on Si substrates achieved higher efficiency and responsivity than most of the examples in the literature. Also normalized detectivity of this photodiode is quite good such that most of the examples except ref. 32, stay under 10^{11} at wavelengths of 1400 nm.

The PbS photodiode that is realized on ROIC mimics also achieved moderate responsivity of 0.2 A/W and efficiency of 15% at 1 V reverse bias. At this bias the normalized detectivity is extracted as 1.36×10^{11} Jones which is quite high. However; when the reverse bias is increased to 2V, the responsivity increases enormously to 5.73 A/W that is more like a photoconductor behavior and this result is higher than all the examples in the list. Also at this bias point, the PbS CQD photodiode achieved $1.41 \times$

10^{12} Jones detectivity, which is comparable with the single crystal compound semiconductor detectors.

Table 6. Comparison of PbS CQD photodiodes on glass, silicon and ROIC, which are realized in this work, with the state of the art solution based photodiodes in the literature

Year	λ (nm)	EQE(%) or R(AW ⁻¹)	D* meas (Jones)	3dB BW (Hz)	Material	Features
2005 [24]	400-700	0.2 % @ 0V, 550nm 15% @ -6V, 550 nm	10 ⁸	5x10 ⁴	CdSe quantum dots	Early quantum-photodiode
2009 [32]	Vis-1600	25% @ -1V 12% @ 0V	10 ¹² @ 1450 nm	10 ⁶	PbS QD	Megahertz response in fully depleted photodiode
2009 [33]	Vis-1450	16.5% @ -5V, 1220 nm 0,16 A/W @ -5V, 1220 nm	2.3x10 ⁹ @ 532nm	2x10 ³	PbS QD +PCBM + P3HT	Integrated into an image array
2009 [34]	Vis-1450	20% at 1100 nm	10 ¹² NIR 10 ¹³ VIS		PDDTT + PCBM	Long-wavelength polymer photodetector
2010 [35]	250 – 1600 nm	24% @ 0V, 980 nm 49% @ -2.5V, 980 nm			PbS QD – C60 Heterojunction	Heterojunction with C60
2011 [36]	Up to 1300 nm	23% 430nm 7% 610nm	4.7x10 ⁹ @ 1300 nm		P3HT:Pbs QD:PCBM blend	Pb QDs with polymer blend
2011 [37]	600-1400 nm	0.2 % at 1100 nm	1x10 ¹¹ @ 1200 nm 1x10 ⁹ @ 1300 nm		TFB+PbSe CQ + ZnO NC	Better dark current perf. With blocking layers
This work Al/Pbs	Vis -1600	15,6 % @ -2V 0.195 A/W @ -2V	8.19 x 10 ¹⁰ @ -2V		PbS QD	High detectivity @ 1550 nm
This work Au-Ti/Pbs	Vis -1600	53.3% @ -3V 0.667 A/W @ -3V	2.12 x 10 ¹⁰ @ -3V		PbS QD	High efficiency, long lifetime
Al/PBS on Si	Vis -1600	32 % 0.4 A/W	1,91 x 10 ¹¹		PbS QD	On silicon substrate
Al/PbS on ROIC mimic	Vis -1600	0.2 A/W, 16.4% PD 5,73 A/W PC	1,36 x 10 ¹¹ PD 1,41x 10 ¹² PC		PbS QD	Integrated on ROIC mimic

Chapter 5

PLASMONICS IN PbS CQD PHOTOCONDUCTORS

As mentioned before, PbS CQD photodetectors gain importance due to their solution-processability and bandgap tunability extended from the visible to the infrared spectrum. Recently PbS CQDs are used in many applications such as photoconductive detectors, photodiodes and CQD solar cells [36, 60]. PbS CQDs offer high absorption coefficients 10^5 cm^{-1} in the visible spectrum yet, their absorption coefficient near their band edge is 10^4 cm^{-1} . For this reason, thick films are required to fully absorb the incident light [56]. However, having thicker films presents a bottleneck in achieving efficient carrier extraction. In photoconductive detectors, further enhancement in sensitivity can be achieved by employing thinner absorbing layers in view of the dark current reduction and reduced generation-recombination noise. Light trapping schemes to increase absorption in the active layer can offer the possibility to overcome these challenges towards more efficient QD solar cells and more sensitive photodetectors.

The use of plasmonics to improve the performance of photodetectors and solar cells has experienced rapidly growing interest in the past decade and most of the efforts have been focused on light trapping via far-field scattering where incident light is scattered by plasmonic nanostructures and coupled into trapped modes in the active region of the cell. In thin cells, however, light must undergo multiple scattering events in order to increase the optical path and thus the losses in the scattering structure is very critical. Additionally, for cells with ultra-thin active regions, such as quantum dot and polymer solar cells on the order of 100-300 nm thick, the number of guided photonic modes in the structure is restricted, reducing the overall broadband absorption enhancement that can be achieved [82].

Use of small metal nanoparticles (MNP), 3-50nm, is advantageous in solution based semiconductors, because small nanoparticles can also be synthesized and processed in solution phase. At small sizes of MNPs, far field scattering is not the major

component of the enhancement and the optical fields in small sized MNPs are enhanced locally in the vicinity of MNP, called near field enhancement. In the literature, Light trapping schemes based on far-field scattering from metal nanostructures on silicon solar cells [83] and on near field enhancements from embedded metal nanoparticles (MNPs) in polymer solar cells [84], have been reported. In terms of absorption enhancement using plasmonics in PbS CQDs photodetectors, only one paper is reported [85]. Konstantatos et. al. report broadband responsivity enhancement in PbS colloidal quantum dot (CQDs) photoconductive photodetectors due to absorption increase offered by a plasmonic scattering layer of Ag islandised films. In order to create and islandised Ag film, a very thin layer of Ag is deposited on substrate and annealed at 250 °C to form discrete MNPs. They achieved 2.4 fold increase in responsivity; however, this process is not IC compatible because of high temperature annealing.

In this chapter, plasmonic enhancement to PbS CQD photoconductors is achieved using solution based gold nanoparticles. Colloidal gold nanoparticles with 5 nm diameter are placed in the middle of PbS CQD film in order to increase scattering of incident light and thus enhance the responsivity of the photoconductor. In this chapter, different than previous chapters, photoconductor topology is used to observe the absorption and responsivity change depending on metal nanoparticles. The reason for that is the photoconductor topology is simpler than the photodiode one such that, CQD film is spin cast on the interdigitated electrodes. The simple structure has given us the ability to focus more on the metal nanoparticle implementation in the PbS film.

5.1 PbS CQD based photoconductor

5.1.1 Structure and fabrication of PbS CQD based photoconductor

A typical CQD photoconductor employ coplanar electrodes coated with a continuous film of nanocrystals which is described in section 2.3.2. The realization of these devices is greatly simplified by the simple spin casting of a quantum dot film atop electrodes prefabricated on a substrate. The current flow direction is primarily within

the horizontal plane. The distance photocarriers must travel and thus their transit time, relevant to gain is determined by the contact separation.

In this work, PbS CQD based photoconductors is fabricated on silicon substrates. The photodetector is composed of interdigitated electrodes that have $5\mu\text{m}$ finger width and $5\mu\text{m}$ spacing between fingers. The length of each finger is $1000\mu\text{m}$. The total active area of the photoconductors is $1000\mu\text{m} \times 1000\mu\text{m}$. The fabrication process of PbS CQD photoconductor is quite straightforward. The process is started with cleaning of P-type Si wafers that have $1\mu\text{m}$ thermally grown oxide on top. Then Al is deposited on the substrate using DC magnetron sputtering. Deposition takes place with 250 W DC power and 35 sccm Ar flow in the chamber with the pressure of 1.7×10^{-2} mbar. 15 min deposition resulted in 250 nm Al layer.

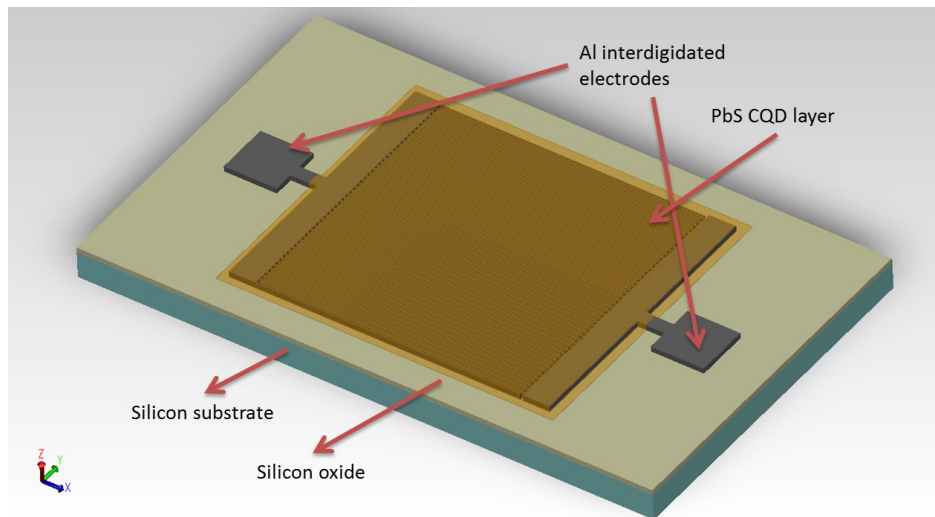


Figure 59. 3D illustration of PbS CQD based photodiode

After the interdigitated electrodes are formed, the PbS layer is spin deposited on the electrodes. Previously optimized layer by layer spin deposition steps is also used in these samples. In addition to that, long oleic acid capping ligands are replaced with shorter ligands threating PbS layer with 3-MPA during the spin coating process. The details of spin coating of PbS and solid state ligand exchange procedure is given in detail in section 3.3.4 and 3.4 respectively. The thickness of the resulting PbS CQD layer is measured as 300 nm.

5.1.2 Test setup and measurements of PbS CQD photoconductors

A test setup is prepared for characterization of PbS CQD photoconductors that is very similar to previous test setups. Cascade PM5 DC Probe Station is used for probing of the photoconductor contacts. Agilent Semiconductor Parameter Analyzer is used for I-V measurements.

First the photoconductors are placed in probe station and the shield enclosure of the probe station is closed without any illumination inside. The bias voltage that is applied to the two contacts of the photoconductor are swept from 0 to 10V and the current is measured for each voltage point by semiconductor parameter analyzer. The resulting I-V graph under dark conditions is given in Figure 60. Without illumination it can be easily observed that the current linearly increases with increasing bias voltages. The dark current measured is 0.4 nA at 1 volt bias and increases to 1.5 nA at 2 V bias, 5.8 nA at 5V bias and 17 nA at 10 V bias.

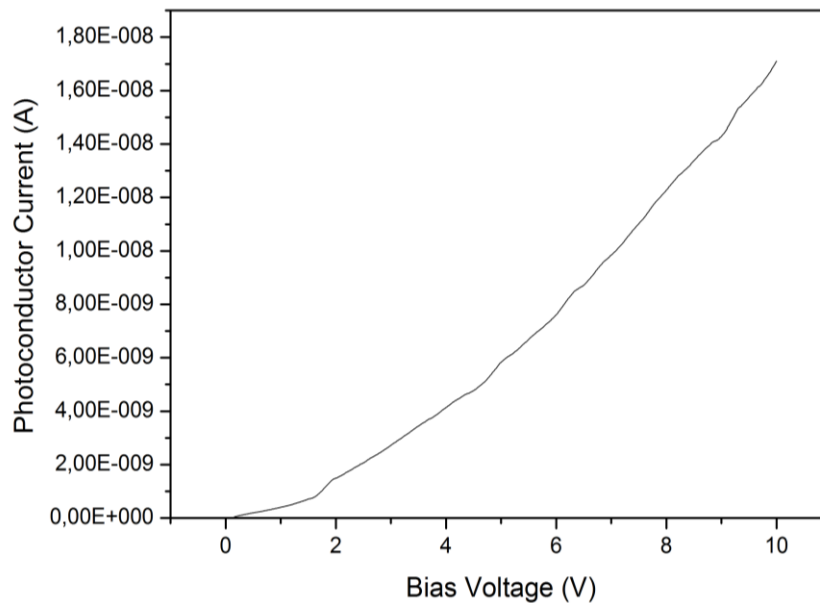


Figure 60. I-V characteristics of PbS CQD photoconductor under dark conditions

Next the photoresponse of photoconductor is measured in the presence of illumination. For illumination Motic MLC-150C Cold Light Source is used which is described in section 4.3.3. The illumination irradiance on sample is calibrated using ThorLabs PM100 Optical Power Meter System. The Germanium (Ge) detector of

Optical Power Meter System is put in place of the Al/PbS detector on the small optic table and then the power on the PbS detector is estimated from the power reading on the reference detector. It is found to be that the Al/PbS detector is illuminated with $140 \mu\text{W}/\text{cm}^2$ at 1550 nm wavelength.

The photoresponse characteristic of the PbS CQD photoconductor in linear scale is given in Figure 61. Both dark current and the current under illumination are measured up to 10 V . Since, we use photoconductor topology here instead of photodiode topology; we have applied higher bias voltages between two terminals in order to increase the gain. It can be observed from the graph that the photocurrent increases with the applied biases. At low bias voltages the photocurrent is around a couple nano amperes, increases to 44 nA at 5 V bias and at 10 V bias voltage the photoconductor gives $1,9 \mu\text{A}$ photocurrent which is around 100 fold higher than dark current. This is the typical characteristic of photoconductors which is described in section 2.3.2. Photoconductive gain is a function of the electric field in the semiconductor and increases with applied bias.

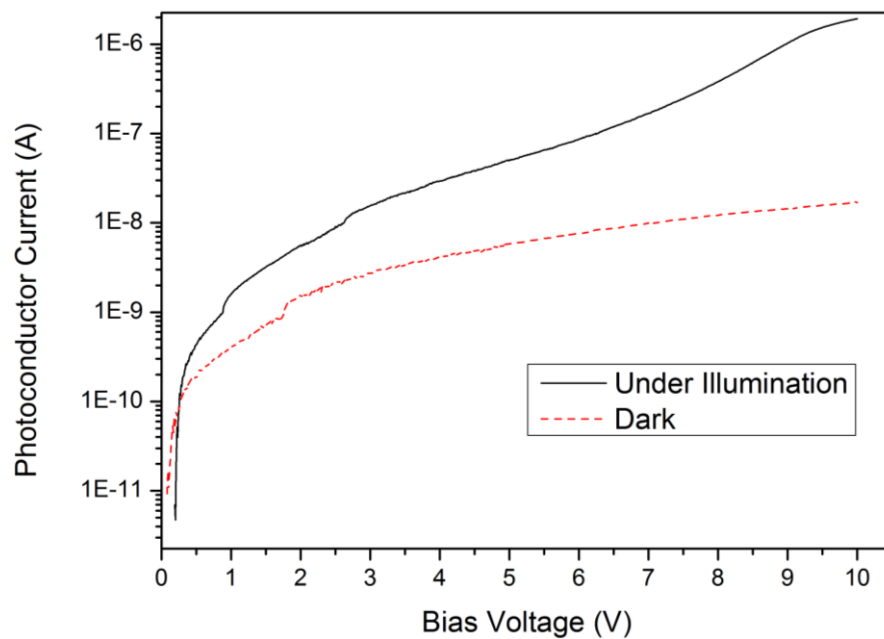


Figure 61. I-V characteristics of photoconductor under dark and under $140 \mu\text{W}/\text{cm}^2$ illumination

The responsivity change due to the applied bias voltage is presented in Figure 62. Around 5 V bias, the responsivity was around 0.1 A/W whereas it dramatically

increases with further bias and reaches 5 A/W at 10 V bias. Both photocurrent and responsivity increase are related with increasing electric field between the contacts of the photoconductor with applied bias. Unlike photodiodes, in photoconductors, there can be more than one charge carrier traversing the device for a single carrier generation event resulting photoconductive gain, which is a function of the electric field in the semiconductor and increases with bias as shown in equation 2.9 in section 2.3.2. Detectivity is calculated by the assumption that the noise-current spectral density is dominated by shot noise in the dark current and it is extracted for 10 V bias as $4,17 \times 10^{12}$ Jones.

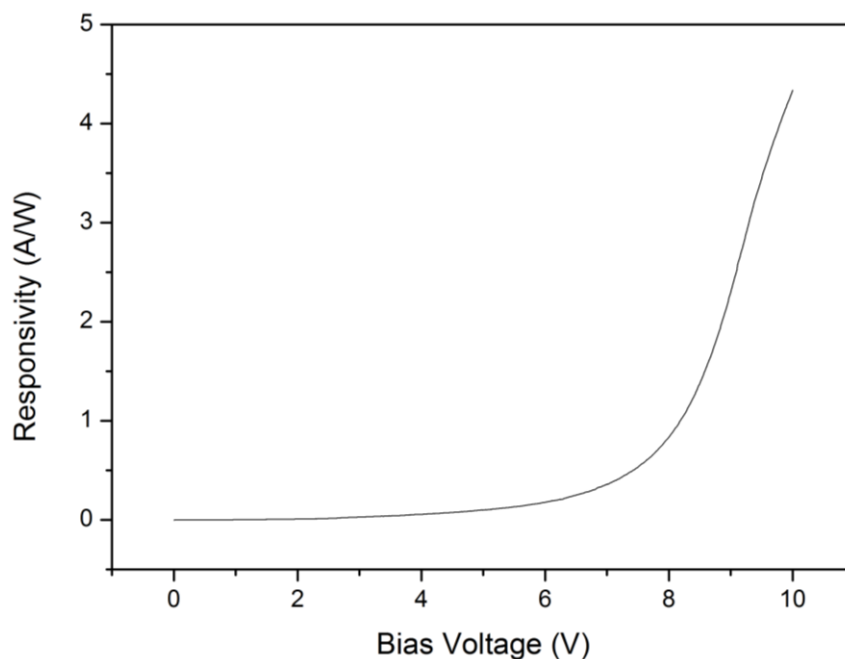


Figure 62. Responsivity change due to the applied bias. At higher biases responsivity increases due to higher electric field.

As a next step, the correlation between the photoresponse on the reverse bias and irradiance is measured. The irradiance is swept between $8,469 \mu\text{W}/\text{cm}^2$ and $134,093 \mu\text{W}/\text{cm}^2$ and the photoconductor current behavior is observed as shown in Figure 63. It can be seen that with increasing irradiance, the photocurrent of the photoconductor increases. The correlation between irradiance and photocurrent is clearer in Figure 64 where the photocurrent change due to the irradiance is drawn for 10V bias. The photoresponse is linear over irradiance change from $8,469 \mu\text{W}/\text{cm}^2$ to $134,093 \mu\text{W}/\text{cm}^2$. The photoconductive mechanism in PbS relies on the availability of minority carrier electron traps. With increasing illumination levels, these traps become full, altering the

photoresponse of the device. This effect limits the linearity of the photoresponse of PbS CQD photoconductors. It can be observed from Figure 66 that, from $8.5 \mu\text{W}/\text{cm}^2$ upto $140 \mu\text{W}/\text{cm}^2$ the photoresponse is linear meaning that the traps do not become full in this region.

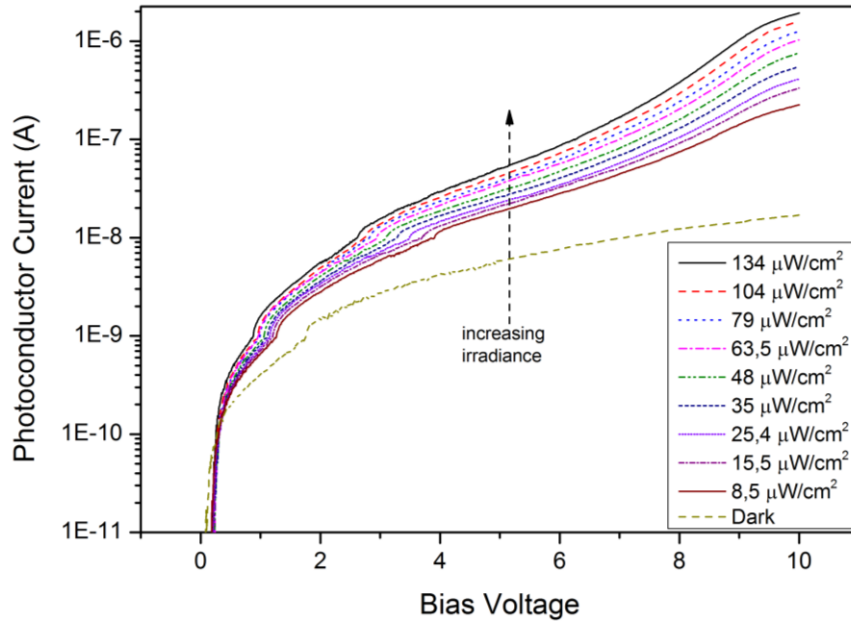


Figure 63. Photocurrent vs. bias voltage graph for irradiances between $8,5 \mu\text{W}/\text{cm}^2$ to $134 \mu\text{W}/\text{cm}^2$

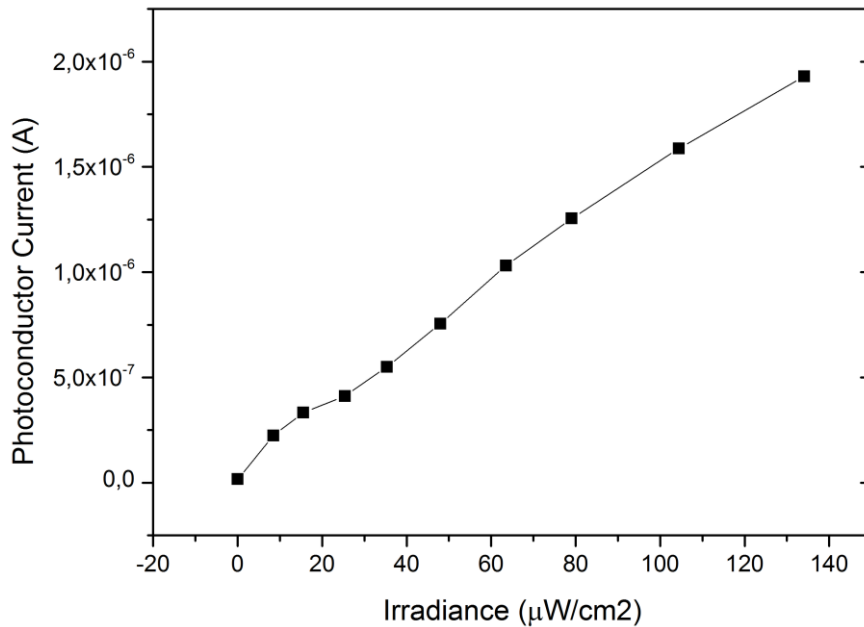


Figure 64. Photoconductor current change due to the irradiance change

5.2 Responsivity Enhancement of PbS Photoconductors Using Plasmonics

5.2.1 Plasmonic PbS photoconductor structure

In PbS CQD photoconductors thick films are required to fully absorb the incident light; however, having thicker films presents a bottleneck in achieving efficient carrier extraction. In order to overcome this bottle neck gold nanoparticles is placed in PbS CQD film in order to take advantage of plasmonic scattering. Figure 65, presents a summary of our strategy to enhance the absorbance of PbS CQD film and thus enhance the responsivity of PbS photoconductors. Figure 65 (a) shows a conventional PbS CQD photoconductor which is formed of coating PbS CQD layer on top of Al interdigitated electrodes by using layer by layer spin coating technique. We introduced gold nanoparticles during the middle layers of spin coating process in order to have a gold nanoparticle / PbS blend in the middle in order to scatter the light more into the PbS film as shown in Figure 65 (b).

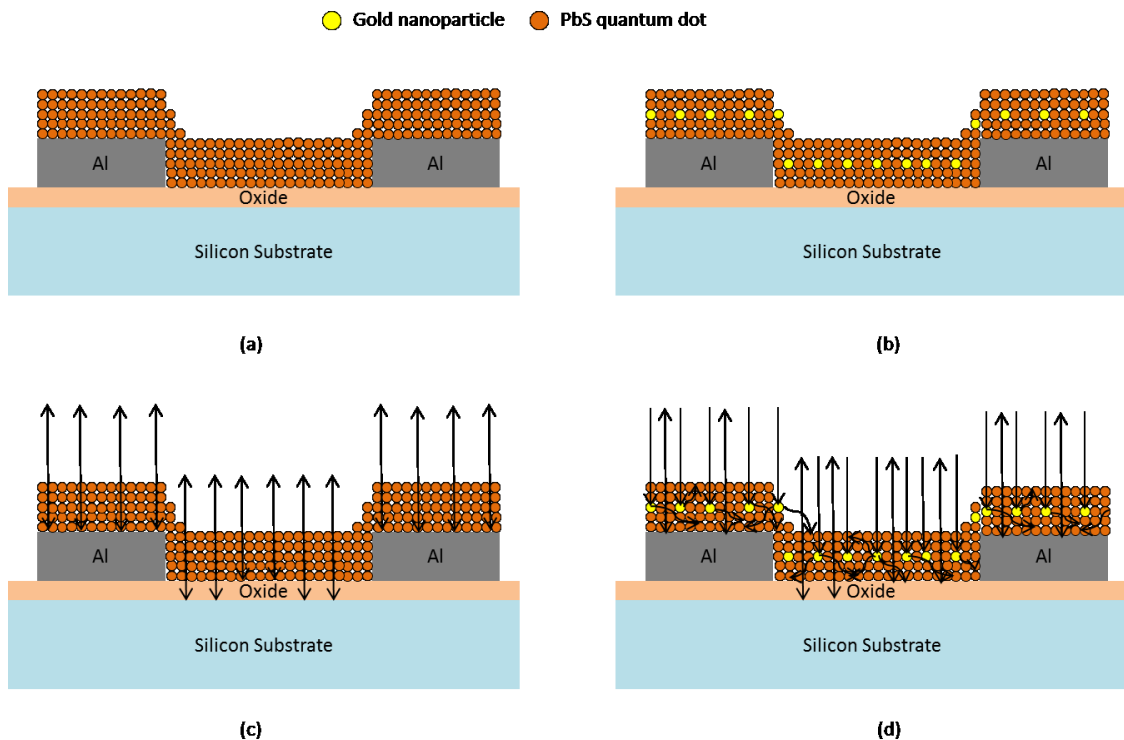


Figure 65. a) Conventional PbS CQD photoconductor b) gold nanoparticles applied for plasmonic scattering to enhancer responsivity c) absorption and reflection in conventional PbS CQD photoconductor d) gold nanoparticles scatter incident light more into the PbS film enhancing absorbance thus enhancing responsivity

In conventional photoconductors, a portion of incident light is absorbed by the PbS film, whereas the rest is either reflected back from Al/PbS or Si/SiO₂/PbS interface, or transmitted through the substrate as shown in Figure 65 (c). On the other hand, when gold nanoparticles is introduced in the film, a portion of the incident light, scatters form gold nanoparticles into the film which results increase in the absorbance. This scattering event is illustrated in Figure 65 (d). This increase in the absorbance also improves the responsivity of the device.

5.2.2 Fabrication of plasmonics enhanced PbS CQD photoconductors

PbS CQD based photoconductors is fabricated on silicon substrates that have 1 μm thermally grown oxide on them. The photodetector is composed of interdigitated electrodes that have 5μm finger width and 5μm spacing between fingers. The length of each finger is 1000 μm. The total active area of the photoconductors is 1000 μm x 1000 μm. The process is started with cleaning of P-type Si wafers that have 1μm thermally grown oxide on top. Then Al is deposited on the substrate using DC magnetron sputtering. Deposition takes place with 250 W DC power and 35 sccm Ar flow in the chamber with the pressure of 1.7×10^{-2} mbar. 15 min deposition resulted in 250 nm Al layer.

Following forming of the interdigitated electrodes, the PbS layer is spin deposited on the electrodes. Previously optimized layer by layer spin deposition steps is also used in these samples. In addition to that, long oleic acid capping ligands are replaced with shorter ligands threating PbS layer with 3-MPA during the spin coating process. During the layer by layer depositing and solid state ligand exchange steps, colloidal gold nanoparticles is spin cast and the PbS layer by layer process continued afterwards. The devices composed of 8 layers of PbS. Gold nanoparticles is spin cast after the 4th layer that places the in the middle, sandwiched between PbS films. The reason for that is to avoid electrical shorts between the fingers. The thickness of the resulting PbS CQD layer is measured as 300 nm.

Colloidal gold nanoparticles are obtained from Sigma Aldrich. The particle size of the gold nanoparticles is selected to be 5 nm which is equal to the size of PbS CQDs. Colloidal gold nanoparticles are dispersed in citrate buffer. The concentration of gold

nanoparticles is 5.5×10^{13} particles/mL. Two different concentrations of gold nanoparticles are prepared; one being 0.01% in citrate (as received) and the other 0.1% in citrate as shown in Figure 66 in order to study the effect of concentration is responsivity enhancement.

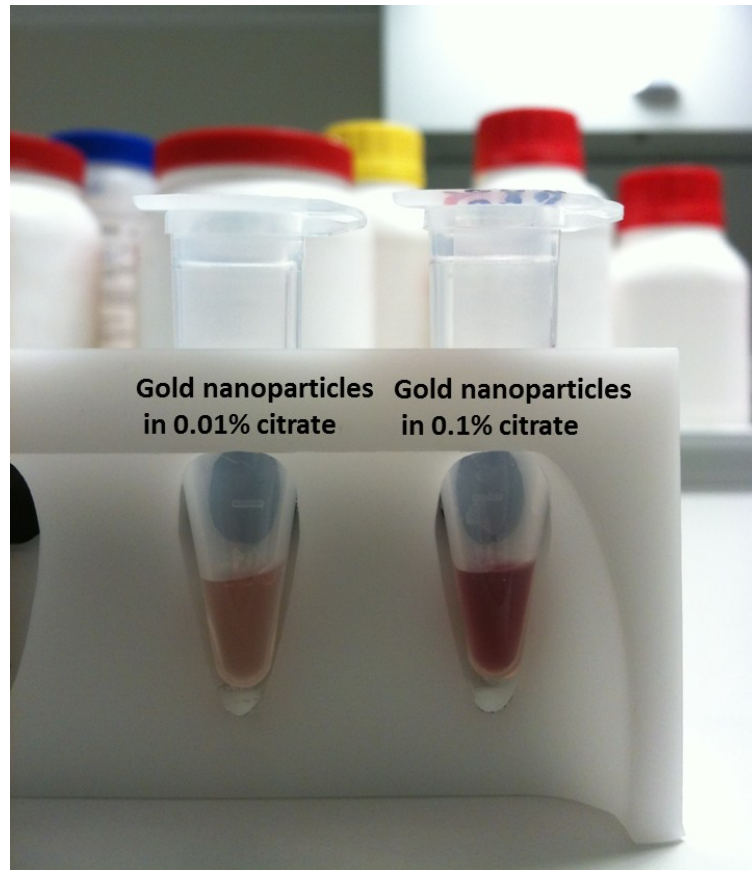


Figure 66. Two different concentration of colloidal gold nanoparticle solution in citrate is prepared; one 0.01% and the other is 0.1% in citrate

5.2.3 Measurement results

Three identical PbS CQD photoconductor device is fabricated; one of the being conventional photoconductor without any gold nanoparticles (reference sample), one processed with 0.01% solution of gold nanoparticles and the other processed 0.1% solution of gold nanoparticles. The test setup is identical to the one used in section 5.1.2 where Cascade PM5 DC Probe Station is used for probing of the photoconductor contacts, Agilent Semiconductor Parameter Analyzer is used for I-V measurements and Motic MLC-150C Cold Light Source is used for illumination.

Bias voltage – photoconductor current graph of PbS CQD photoconductor without any gold nanoparticles is shown in Figure 67. Dark current at 5V bias is 6,5nA whereas under $140 \mu\text{W}/\text{cm}^2$ illumination, photoconductor current is 37,4 nA. At 10 V bias both dark current and photocurrent increases dramatically, dark current being 53,4 nA and photocurrent under illumination is 3,68 μA . At 10 V bias, the PbS CQD reference photoconductor achieve a responsivity of 8,22 A/W. Also detectivity is calculated with the assumption that the noise-current spectral density is dominated by shot noise in the dark current and it is extracted for 10 V bias as $4,45 \times 10^{12}$ Jones.

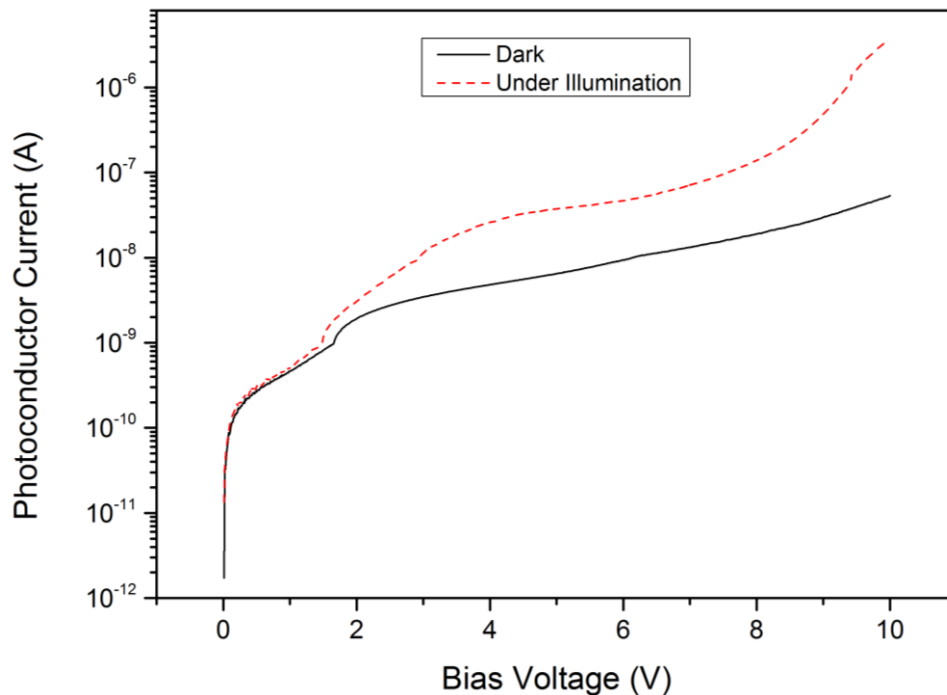


Figure 67. I-V graph of reference sample under dark and $140 \mu\text{W}/\text{cm}^2$ illumination

Bias voltage – photoconductor current graph of PbS CQD photoconductor that 0.01% gold nanoparticles solution is applied, is shown in Figure 68. Dark current at 5V bias is 75.7 nA whereas under $140 \mu\text{W}/\text{cm}^2$ illumination, photoconductor current is 1.55 μA . At 10 V bias both dark current and photocurrent increases dramatically, dark current being 5.47 μA and photocurrent under illumination is 15 μA . At 10 V bias, the PbS CQD reference photoconductor achieve a responsivity of 19.1 A/W. Also detectivity is calculated with the assumption that the noise-current spectral density is dominated by shot noise in the dark current and it is extracted for 10 V bias as $1,15 \times 10^{12}$ Jones.

Bias voltage – photoconductor current graph of PbS CQD photoconductor that 0.1% gold nanoparticles solution is applied, is shown in. Dark current at 5V bias is 75.7 nA whereas under $140 \mu\text{W}/\text{cm}^2$ illumination, photoconductor current is $1.55 \mu\text{A}$. At 10 V bias both dark current and photocurrent increases dramatically, dark current being $5.47 \mu\text{A}$ and photocurrent under illumination is $15 \mu\text{A}$. At 10 V bias, the PbS CQD reference photoconductor achieve a responsivity of 21.6 A/W. Also detectivity is calculated with the assumption that the noise-current spectral density is dominated by shot noise in the dark current and it is extracted for 10 V bias as $1,15 \times 10^{12}$ Jones.

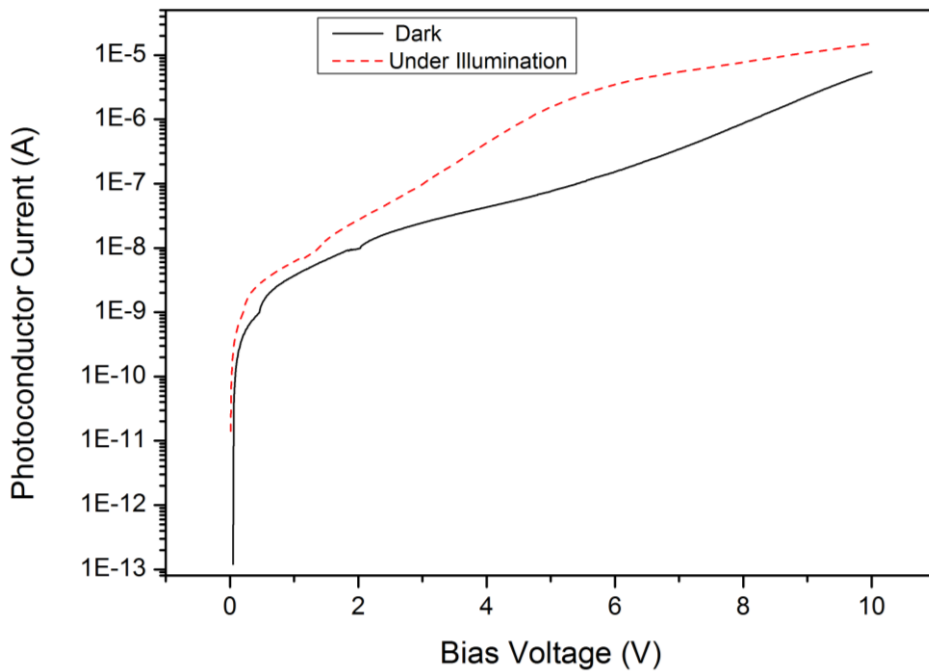


Figure 68. I-V graph of the sample that 0.01% gold nanoparticles is applied, under dark and $140 \mu\text{W}/\text{cm}^2$ illumination

PbS CQD photoconductor with gold nanoparticles that are applied in a 0.1% solution shows an I-V characteristic that is given in Figure 69. At 10 V bias, dark current is $9.23 \mu\text{A}$ and photocurrent under illumination is $32.9 \mu\text{A}$. At 10 V bias, the PbS CQD reference photoconductor achieve a responsivity of 53 A/W. Also detectivity is calculated with the assumption that the noise-current spectral density is dominated by shot noise in the dark current and it is extracted for 10 V bias as 2.21×10^{12} Jones.

Comparing three devices we can see that introducing gold nanoparticles in the PbS film increases the photocurrent yet, at the same time it increases the dark currents

too as shown in Figure 70. Increasing photocurrent is a clear indication of increased absorption of the PbS layer due to the plasmonic scattering. The dark current increase can be associated with gold nanoparticles, decreasing the effective resistance of the film and thus increasing the leakage currents.

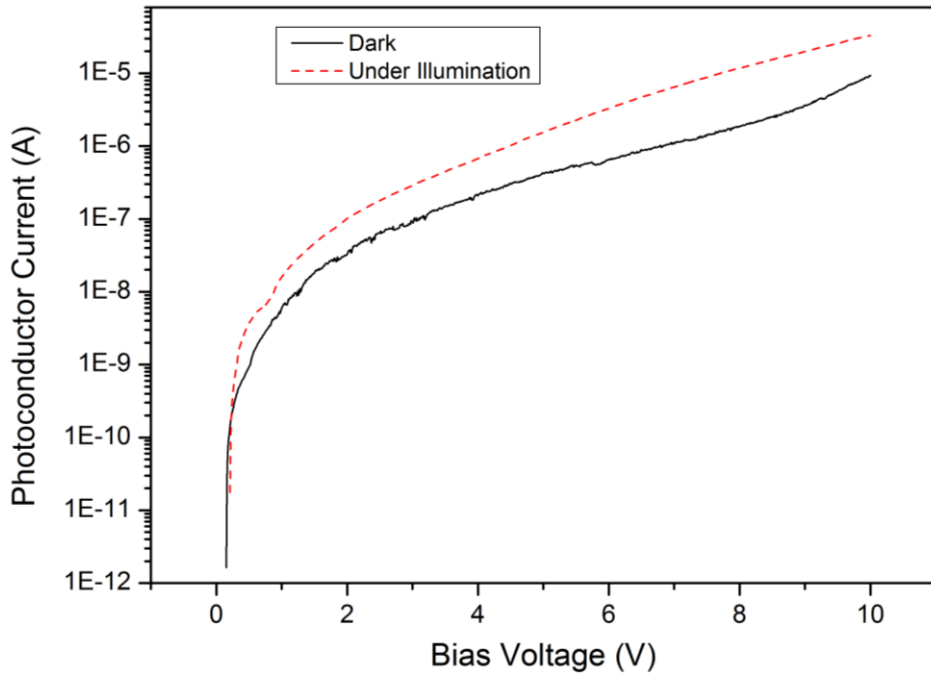


Figure 69. I-V graph of the sample that 0.1% gold nanoparticles is applied, under dark and $140 \mu\text{W}/\text{cm}^2$ illumination

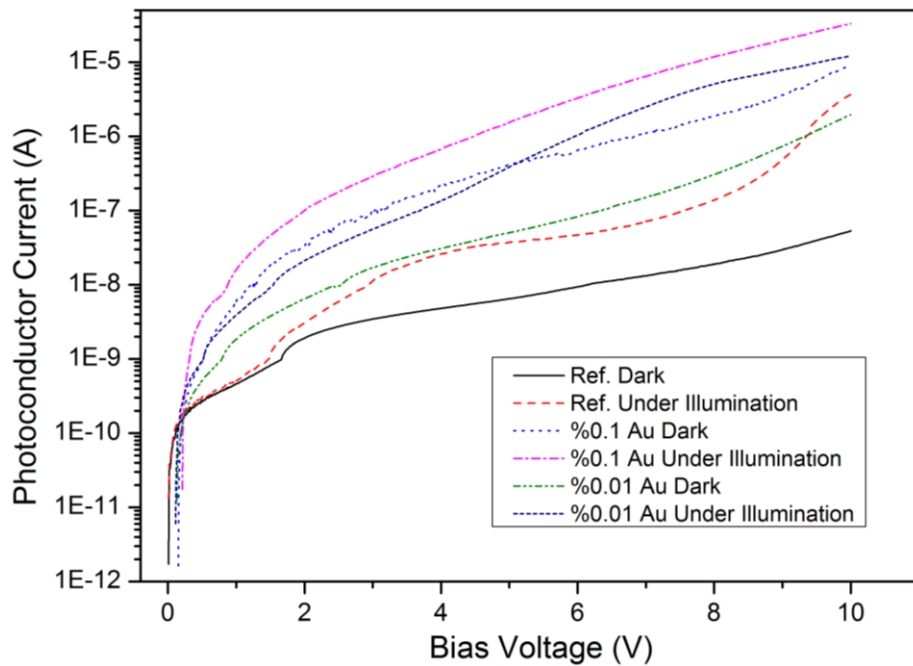


Figure 70. I-V graphs of all three samples under dark and under illumination.

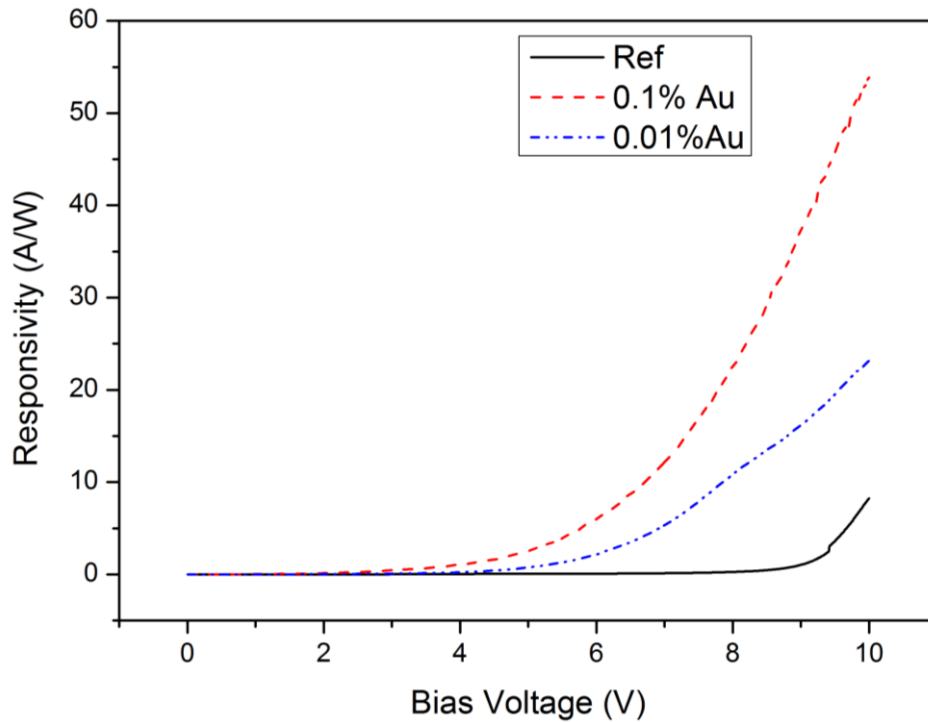


Figure 71. Responsivity of the three devices for changing bias voltages. Responsivity increases with introducing Au nanoparticles.

The responsivity change of the three samples is given in Figure 71. At 10 V bias the responsivity of reference sample was 8,22 A/W and increased to 21.6 A/W for the sample processed with 0.01% Au nanoparticles. Increasing the concentration of the applied Au nanoparticles to 0.1% resulted further increase in responsivity and it is measured as 53,7 A/W at 10 V bias for the sample treated with 0.1% Au nanoparticles. So it can be said that introducing 0.01% Au nanoparticles in PbS film increases the responsivity 2.6 fold whereas introducing 0.1% Au nanoparticles results in 6.5 fold increase in responsivity. However it must be noted that the detectivity of the samples are decreased by introducing gold nanoparticles. At reference sample the detectivity is calculated as 4.45×10^{12} Jones where as it is decreased to 1.15×10^{12} Jones for 0.01% Au applied sample and to $2,21 \times 10^{12}$ Jones for 0.1% Au applied sample. The dark current increase associated with introducing metal impurities in the film resulted decrease in detectivity.

5.3 Results and Discussion

In this chapter we have studied to improve the absorption of the PbS CQD films using plasmonic scattering. In this work, colloidal gold nanoparticles of sizes 5nm is integrated in PbS film during spin deposition process. The devices composed of 8 layers of PbS and gold nanoparticles is spin cast after the 4th layer that places the in the middle, sandwiched between PbS films. The reason for that is to avoid electrical shorts between the fingers. The thickness of the resulting PbS CQD layer is measured as 300 nm. Two different solutions of gold nanoparticles in citrate, 0.1% and 0.01% is used to fabricate two different devices. Comparing these two devices and a reference one that do not have any metal nanoparticles, it has been seen that introducing gold nanoparticles in the PbS film increases the photocurrent and responsivity yet, at the same time it increases the dark currents too. Introducing 0.01% Au nanoparticles in PbS film increases the responsivity 2.6 fold whereas introducing 0.1% Au nanoparticles results in 6.5 fold increase in responsivity. However it must be noted that the detectivity of the samples are decreased by introducing gold nanoparticles. At reference sample the detectivity is calculated as 4.45×10^{12} Jones where as it is decreased to 1.15×10^{12} Jones for 0.01% Au applied sample and to 2.21×10^{12} Jones for 0.1% Au applied sample. The dark current increase associated with introducing metal impurities in the film resulted decrease in detectivity.

Table 7 gives the comparison of PbS CQD photoconductors realized in this work, with the state of the art solution based photoconductors in the literature. Comparing with photodiodes given in Table 6, it can be observed that the normalized detectivities are higher in photoconductors such as in the orders of 10^{12} ; however, the bandwidths of photoconductors are in the order of tens of Hz. Most of the solution based photodetectors in the literature are in the visible range up to 850 nm. Clifford et. al [25] presented a high performance photoconductor working up to 1500 nm, with a responsivity of 1000 A/W at 40 V bias and have the normalized detectivity of 5×10^{12} at 1450 nm and 5×10^{13} at 975 nm. Another IR solution based photoconductor is based on HgTe quantum dots that works from visible to 3000 nm. This photoconductor achieves 4.4 A/W responsivity and 3×10^{10} Jones normalized detectivity. Reference Al/PbS photoconductors realized in this study achieves 5 A/W responsivity at 10 V bias at 1550

nm wavelength. The normalized detectivity of these photoconductors are 4.17×10^{12} Jones which is one of the best responsivities reported up to date. Introducing Au nanoparticles to PbS films increased the responsivities up to 19.1 A/W and 53 A/W for 0.01% and 0.1% Au nanoparticles in citrate, respectively. However, detectivities for gold nanoparticle introduced samples are lower than the reference one, yet still better than most of the others.

Table 7. Comparison of PbS CQD photoconductors realized in this work, with the state of the art solution based photoconductors in the literature

Year	λ (nm)	EQE(%) or R(AW ⁻¹)	D* meas (Jones)	3dB BW (Hz)	Material	Features
2006 [25]	Vis-1300	1000 AW ⁻¹ @ 40 V	5×10^{13} @ 975 nm 5×10^{12} @ 1450 nm	2×10^1	PbS QD	Record sensitivity, pure QD device.
2007 [26]	Vis-850	120 AW ⁻¹	5×10^{12}	2×10^1	PbS QD	Visible only device using ultraconfined dots
2007 [27]	Vis-3000	4.4 AW ⁻¹	3×10^{10}	10^1	HgTe QD	Long wavelength operation
2008 [28]	350-650	50 AW ⁻¹	5×10^{12}		P3HT+PCBM+ CdTe QD	Sensitive heterojunction device
2008 [29]	Vis-850	10 AW ⁻¹	1.3×10^{13}	5×10^1	PbS QD	High-uniformity device
2008 [30]	Vis-850	12 AW ⁻¹	10^{12}	3×10^1	PbS QD	Single-trap time constant
2009 [31]	250-930	18 AW ⁻¹	1.5×10^{14}	3×10^1	PbS QD	Multi excitation generation enhanced
Ref Al/PbS PC	Vis-1600	5 AW ⁻¹	4.17×10^{12}		PbS QD	
Al/PbS 0.01% Au	Vis-1600	19.1 AW ⁻¹	1.15×10^{12}		PbS QD	Plasmonic scattering by Au NP
Al/PbS 0.1% Au	Vis-1600	53 AW ⁻¹	2.21×10^{12}		PbS QD	Plasmonic scattering by denser Au NP

Chapter 6

CONCLUSIONS & FUTURE WORK

This work presents a study on PbS CQD based photodetectors to implement low cost, high performance photodetectors that can be alternatives to conventionally used InGaAs, HgCdTe, Ge, PbS or PbSe compound semiconductor counterparts, especially in applications where there are cost constraints. Throughout the study, different examples of PbS CQD based photodetectors are implemented on both glass and silicon substrates. IC integration has been our primary focus in this study. Therefore, in implementation of various photodetectors, the process conditions are always selected to be at low temperature.

Up to now, in the literature the PbS CQD based photodiodes is mainly fabricated on ITO coated glass samples. Since it eases the process steps and conventionally implemented like this, the study started by implementing PbS CQD based schottky photodiodes on glass samples. While implementing these devices, PbS CQD film formation is studied in detail, which is the most crucial part in realizing solution based photodiodes or photoconductors. Improvement in film quality is observed when layer by layer deposition topology is used. Also solid state ligand exchange procedure is used to increase the carrier mobility in the PbS film. Both layer by layer spin deposition and ligand exchange procedure takes place at the same time and the steps are optimized that resulted in pinhole and crack free, shiny uniform PbS films. The optimized process is used for all devices in this study.

Two different kinds of PbS CQD schottky diodes are implemented on glass, one having aluminum metal to form a schottky barrier and the other using titanium and gold stack. Ti-Au/PbS diode show higher rectification ratio than the Al/PbS one; however, the

dark current of the Ti-Au/PbS diode is measured to be higher than Al/PbS. This high dark current can be attributed to the interaction of PbS–Ti/Al interface. Sputter depositing of Ti is done at higher powers than Al resulting higher damage to PbS layer thus increase the dark current in the device. On the other hand, Ti-Au/PbS photodiode achieve higher photocurrents than Al/PbS photodiode under same illumination. At 2V reverse bias, Ti-Au/PbS diode responsivity is measured as 0,354 A/W which is higher than the Al/PbS diode that achieves 0.195 A/W responsivity; however, the detectivity of Ti-Au/PbS is $2,22 \times 10^{10}$ Jones, which is lower than Al/PbS diode that has 8.19×10^{10} Jones detectivity because of the high dark current. High dark current limits the sensitivity of the diode. Increasing the reverse bias voltage to 3V in Ti-Au/PbS photodiode the responsivity increases to 0,667 A/W. The quantum efficiency is measured as 53.3% at 3 V reverse bias. However, extracting detectivity for 3V reverse bias, it is observed that, it has decreased to $2,12 \times 10^{10}$ Jones because of the limiting behavior of the high dark current.

It has been also observed that the lifetime of the Ti-Au/PbS CQD photodiodes is higher than the Al/PbS CQD photodiodes. Using Au-Ti stack instead of Al improves lifetime of the device by limiting the oxidation of underlying PbS layer. Ti is a low work function metal like Al and Au on Ti decreases the oxidation of Ti layer and hence the underlying PbS layer.

Comparing these photodiodes with the state of the art examples of solution based photodiodes we can easily see that, overall performance of our photodiodes is better than most of the reported examples. For instance, Al/Pbs CQD photodiodes achieved high normalized detectivities as 8.19×10^{10} Jones. Excluding the study of Clifford et. al. [32], these photodiodes performs the highest normalized detectivity among the presented solution based photodiodes up to date. Also quantum efficiencies of these detectors are comparable and even better than other examples shown in Table 6. Au-Ti/PbS photodiodes, on the other hand, presents superior responsivity and quantum efficiency. The responsivity of this photodiode, at 3V reverse bias, is measured to be 0.667 A/W and the quantum efficiency is measured as 53.3%. These values are higher than all of the published works on solution based photodiodes. The normalized detectivity of Au-Ti/PbS diodes is extracted as 2.12×10^{10} Jones at 3V reverse bias.

Careful study and optimization of the spin deposition process and ligand exchange is the most crucial part in the way of achieving this. In this work, the processing and ligand exchange procedure carried on in ambient conditions and together with the final annealing step, the doping of the PbS layer is stabilized. Direct application of short 3-MPA ligands to the oleic acid capped PbS CQDs, improves the stability of CQDs and improves the carrier mobilities in the film. Optimized steps of layer by layer deposition and the solid state ligand exchange ensures that 3-MPA is successfully replaced the long oleic acid ligands without any residues. Also, as to our knowledge, this is the first time that 3-MPA is applied directly to oleic acid capped PbS CQDs by solid state ligand exchange for SWIR photodiodes.

The high efficiencies achieved in this work is also related with the optimized thickness of the PbS film. Typically, absorbance of PbS CQD layer lies in the range of 10^4 - 10^5 cm^{-1} [31] so, thick layers of PbS CQD layers is required to fully absorb the incoming light. However minority carrier diffusion lengths in these layers are around 100 nm and can be increased by correct ligand passivation [31]. So in order to have moderate absorption and efficient device, together with successful ligand passivation, we also have selected the PbS CQD layer thickness as 250 nm. By applying reverse bias of 2V, which is acceptable for most of the IC processes, the diode is fully depleted and photogenerated carriers drifted by the presence of electric field increasing the quantum efficiency of the PbS CQD photodiodes.

In this work it is also aimed to fabricate PbS CQD photodiodes on silicon substrates and also on the mimics of the ROICs. In terms of integration, it is crucial to realize them in this manner, because monolithic integration is the most important advantage of solution based photodetectors.

Creating PbS CQD photodetectors on Si substrates or on ROIC chips entails successful deposition of transparent conductive layers which will form the top layer of the device where the incident light is transmitted into the PbS layer. So a detailed study is carried out on sputter deposition of high quality transparent conductive layers on PbS CQD films. It has been observed that higher DC powers results in better conductivity but decreases transmittance. Also power above 300W damages the ITO target resulting

in cracks on the target. In order to improve the transmittance and conductivity, it has been observed that the main chamber pressure has to be decreased. For that reason all the ITO sputter deposition processes throughout the work is made at lowest chamber pressure achieved to start the plasma in our sputter deposition system, which is 8×10^{-3} mbar. In order to further increase the transmittance, conventional method is to introduce O_2 gas in the plasma during deposition. However, O_2 in the plasma gas decreases the conductivity of the ITO film. As a solution, O_2 is used in pre sputtering resulting in increased O_2 content in ITO target, and then sputter deposition is carried out using Ar only plasma and O_2 rich ITO target. The optimum pre-sputtering time is found to be 3 min for 10 min sputtering resulting in 230 nm ITO film. We have satisfied the aimed resistivity constraint, $<1 \times 10^{-3} \Omega \cdot \text{cm}$, by achieving $6,25 \times 10^{-4} \Omega \cdot \text{cm}$ resistivity. Also we have achieved good transmittance at 1450 such as 87,733 %.

Studying recent work in the literature, it has been observed that the PbS CQD based photodetectors are implemented on glass substrates. In this work we have fabricated PbS CQD photodiodes on silicon substrates and also on the mimics of the ROICs. In terms of integration, it is crucial to realize them in this manner, because monolithic integration is the most important advantage of solution based photodetectors. First, PbS CQD photodiodes are realized in reverse order of the diodes fabricated on glass substrates previously. SiO_2 coated Si substrates are used, Al is deposited as bottom contact the PbS CQD is coated on Al contact. Lastly ITO layer is deposited using a shadow mask. In this kind of photodiodes rectification achieved was smaller than the counterparts that are implemented on glass substrates. However, the dark current performance of these devices was better than the versions on glass substrates and is on the order of 400 pA. The reason for this is the difference in formation of PbS/metal interface. In PbS CQD photodiodes realized on the glass, schottky metal is sputter deposited on the PbS CQD film, which damages the film and hence the metal/PbS film interface. However, in PbS CQD photodiodes realized on the silicon substrate the PbS film is pin deposited on schottky metal. This reduces the damage on the schottky metal/PbS CQD film interface that is introduced with sputter deposition of metals.

Under 2 V reverse bias voltage, Al/PbS CQD photodiode on Si substrate achieved 0,4 A/W responsivity and the quantum efficiency is extracted as 32 %. With the

assumption of shot noise is dominating the noise-current, the detectivity is calculated as $1,91 \times 10^{11}$ Jones. Comparing with the Al/PbS device on glass in chapter 3, this version achieves better detectivity depending on decreased dark current.

In addition to this, in order to estimate the monolithically integrated PbS CQD photodiodes to read-out integrated circuits, a mimic of ROICs top layers are realized on silicon substrates. Al contacts are formed, which is the replica of ROIC's pixel structure realized by the top layer of the IC process. Then the sample is coated with SiO₂ which is similar to the passivation oxide on the ROIC. Finally, 5 μm x 5 μm vias are opened in oxide on Al contacts to create a replica of the bond pad openings on the ROIC which defines our active photodiode area. After that the optimized PbS CQD layer deposition and ITO top contact formation realized.

The rectification in this monolithically integrated PbS CQD photodiodes was low as 1.45 at ±1 V and 2 at ±2 V under dark conditions.. The dark current performance of these diodes was good such as, they achieved dark currents in the range of 400 pAs at 0.5 V reverse bias. Under 1 V reverse bias, the photodiodes achieve moderate responsivity and quantum efficiency such as, 0.2 A/W and 16.4% respectively. Under 2 V reverse bias voltage, the responsivity achieved as 5,73 A/W. With the assumption of shot noise is dominating the noise-current, the detectivity is calculated as $1,41 \times 10^{12}$ Jones. These results are quite good and can be comparable with InGaAS SWIR detectors that nominally have detectivities around 10^{12} Jones at room temperatures.

Also, as shown in Table 6, both Al/PbS photodiodes on silicon substrates and on ROIC mimic show excellent performance comparing the other state of the art works in solution based detector. In Al/PbS on silicon sample, 32% quantum efficiency, diversify this photodiode than the previous reported ones as being the most efficient photodiode. Also the normalized detectivity was good, which is 1.91×10^{11} Jones. On the other hand, Al/PbS photodiode on ROIC mimic, achieves moderate responsivity and efficiency.at 1V reverse bias. When 2V reverse bias applied, the photodiode behave more like photoconductor, giving 5.73A/W responsivity. And the normalized detectivity of the device is increased to 1.41×10^{12} Jones. Responsivity of this photodiode is the

highest responsivity in the photodiodes reported up to now. Also normalized detectivity was the highest one among the other solution based photodiodes.

Looking to the photoresponse of these detectors, it can be observed that under increased reverse bias, the photoresponse increases enormously. But also in forward bias, we have observed an increase in the current under illumination. This behavior implies that these integrated PbS CQD photodetectors works more like a photoconductor. This can be also related to low rectification characteristics. The poor schottky barrier results in the device to enter a photoconductive mode that is formed vertically of Al/PbS/ITO.

We have also studied the absorption behavior due to the plasmonic scattering in the PbS CQD films. In PbS CQD photoconductors thick films are required to fully absorb the incident light; however, having thicker films presents a bottleneck in achieving efficient carrier extraction. In order to overcome this bottleneck plasmonic scattering is used to enhance absorbance in thin films. Conventional method in PbS CQD photoconductors is to create metal nanoparticle islands under the PbS CQD film, however, this required high temperature annealing. In this work, colloidal gold nanoparticles of sizes 5nm is integrated in PbS film during spin deposition process. The devices composed of 8 layers of PbS and gold nanoparticles is spin cast after the 4th layer that places the in the middle, sandwiched between PbS films. The reason for that is to avoid electrical shorts between the fingers. The thickness of the resulting PbS CQD layer is measured as 220 nm. Two different solutions of gold nanoparticles in citrate, 0.1% and 0.01% is used to fabricate two different devices. Comparing these two devices and a reference one that do not have any metal nanoparticles, it has been seen that introducing gold nanoparticles in the PbS film increases the photocurrent and responsivity yet, at the same time it increases the dark currents too. Introducing 0.01% Au nanoparticles in PbS film increases the responsivity 2.6 fold whereas introducing 0.1% Au nanoparticles results in 6.5 fold increase in responsivity. However, it must be noted that the detectivity of the samples are decreased by introducing gold nanoparticles. At reference sample the detectivity is calculated as 4.45×10^{12} Jones where as it is decreased to 1.15×10^{12} Jones for 0.01% Au applied sample and to

2.21×10^{12} Jones for 0.1% Au applied sample. The dark current increase associated with introducing metal impurities in the film resulted decrease in detectivity.

Most of the solution based photodetectors in the literature are in the visible range up to 850 nm. Clifford et. al [25] presented a high performance photoconductor working up to 1500 nm, with a responsivity of 1000 A/W at 40 V bias and have the normalized detectivity of 5×10^{12} at 1450 nm and 5×10^{13} at 975 nm. Another IR solution based photoconductor is based on HgTe quantum dots that work from visible to 3000 nm. This photoconductor achieves 4.4 A/W responsivity and 3×10^{10} Jones normalized detectivity. Reference Al/PbS photoconductors realized in this study achieves 5 A/W responsivity at 10 V bias at 1550 nm wavelength. The normalized detectivity of these photoconductors are 4.17×10^{12} Jones which is one of the best responsivities reported up to date. Introducing Au nanoparticles to PbS films increased the responsivities up to 19.1 A/W and 53 A/W for 0.01% and 0.1% Au nanoparticles in citrate, respectively. However, detectivities for gold nanoparticle introduced samples are lower than the reference one, yet still better than most of the others.

As a future work, large-scale integration of CQD photodiodes with read-out silicon microelectronics would complete the initial direction of this study, demonstrating an IR sensitive, monolithically integrated imaging array. Assuming the performance of CQD photodiodes would be maintained or improved upon, such an array would be capable of SWIR imaging using only naturally occurring airglow illumination.

In this direction, further studies have to be carried out in order to decrease dark current performance and schottky diode characteristics of the photodiodes that are monolithically integrated. Better study of Al/PbS interface, surface modifications and different ligand exchange procedures is required to reach the performance of currently used single crystal photodetectors.

Also another bottleneck that has to be overcome is the behavior of the device in ambient conditions. A detailed study of the Schottky barrier characteristics as a function of exposure to an ambient atmosphere could be undertaken.

In addition to that, further studies on plasmonic effects have to be undertaken. Plasmonics is a promising technique in improving the absorption characteristics of the PbS CQD layers. Through a good modeling of nanoparticles in the PbS films and applying this technique in PbS CQD based photodiodes can lead to performance parameter leaps.

REFERENCES

- [1] (30 November 2007 04.07.2012). *Infrared Vision*. Available: <http://mivim.gel.ulaval.ca/dynamique/index.php?idD=58&Lang1>
- [2] A. Rogalski, "Infrared detectors: an overview," *Infrared Physics & Technology*, vol. 43, pp. 187-210, 2002.
- [3] L. T. P. E .P .G .Smith, G .M .Venzor, E .M .Norton, M .D .Newton, P .M .Goetz, V .K . and Randall, "HgCdTe Focal Plane Arrays for Dual-Color Mid- and Long-Wavelength Infrared Detection," *Journal of Electronic Materials*, vol. 33, pp. 509–516, 2004.
- [4] W. A. R. D .F .King, E .A .Patten, R .W .Graham, T .F .McEwan, J .G .Vodicka, R .F . Bornfreund, P .M .Goetz, G .M .Venzor, and S .M .Johnson, "3rd-Generation 1280 × 720 FPA Development Status at Raytheon Vision Systems," *Proceedings of SPIE 6206*, 2006.
- [5] P. A. N .T .Gordon, J .Giess, A .Graham, J .E .Hails, D .J .Hall, L .Hipwood, C .L .Lones, C .D .Maxeh, J .Price, "Design and Assessment of Metal-Organic Vapour Phase Epitaxy-Grown Dual Wavelength Infrared Detectors," *Journal of Electronic Materials*, vol. 36, pp. 931-936, 2007.
- [6] R. B. M .Münzberg, W .Cabanski, H .Lutz, J .Wendler, J .Ziegler, R .Rehm, and M . Walther, "Multi Spectral IR Detection Modules and Applications," *Proceedings of SPIE 6206*, 2006
- [7] S. V. B. S .D .Gunapala, J .K .Liu, J .M .Mumolo, C .J .Hill, S .B .Rafol, D .Salazar, J . Woollaway, P .D. LeVan, and M .Z .Tidrow, "Towards Dualband Megapixel QWIP Focal Plane Arrays," *Infrared Physics & Technology* vol. 50, pp. 217-226, 2007.
- [8] E. C. A .Nedelcu, P .Bois, and X .Marcadet, "Research Topics at Tales Research and Technology: Small Pixels and Third Generation Applications," *Infrared Physics & Technology*, vol. 50, pp. 227-233, 2007.
- [9] J. A. A .Rogalski, and L .Faraone, "Third-Generation Infrared Photodetector Arrays," *Journal of Applied Physics* vol. 105, pp. 091101-44, 2009.
- [10] M. W. R .Rehm, J .Schmitz, J .Fleißner, J .Ziegler, W .Cabanski, and R .Breiter, "Bispectral Thermal Imaging with Quantum-Well Infrared Photodetectors and InAs/GaSb Type II Superlattices," *Proceedings of SPIE 6292*, p. 629404, 2006.
- [11] M. L. E .Varley, S .J .Lee, J .S .Brown, D .A .Ramirez, A .Stintz, and S .Krishna, "Single Bump, Two-Color Quantum Dot Camera," *Applied Physics Letters 91*, p. 081120, 2007.
- [12] S. D. G. S .Krishna, S .V .Bandara, C .Hill, and D .Z .Ting, "Quantum Dot Based Infrared Focal Plane Arrays," *Proceedings of IEEE 95*, pp. 1838-52, 2007.
- [13] A. Rogalski, "Recent progress in infrared detector technologies," *Infrared Physics & Technology*, vol. 54, pp. 136-154, 2011.
- [14] A. Rogalski, *Infrared Detectors*, 2nd ed. FL, USA: CRC Press Taylor & Francis Group, 2011.
- [15] D. Henz. (2011, 04.07.2012). *The IR Market's Shifting Landscape*.
- [16] C. Q. Choi, "Glow for the Dark," *Scientific American*, vol. 297, pp. 30-32, 2007.

- [17] D. C. Dayton, J. Gonglewski, C. S. Arnauld, I. Mons, and D. Burns, "SWIR Sky-Glow Cloud Correlation with NIR and Visible Clouds: An Urban and Rural Comparison: Postprint " *Technical Paper*, 2009.
- [18] R. Vandermissen, "Night-vision camera combines thermal and low light level images," *Photonik*, 2008.
- [19] M. H. Ettenberg. (2005) A little Night Vision. *Advanced Imaging Magazine*. Available: www.advancedimagingpro.com
- [20] Application Note: Defence Applications for SWIR InGaAs cameras. Available: http://www.machinevision.ca/files/IR_App_Notes/ ApplNote-SWIR_defense.pdf
- [21] InGaAs Products: Overview. Available: <http://www.sensorsinc.com/products.html>
- [22] M. P. Hansen and D. S. Malchow, "Overview of SWIR detectors, cameras, and applications," in *Thermosense Xxx*. vol. 6939, V. P. Vavilov and D. D. Burleigh, Eds., ed, 2008, pp. U82-U92.
- [23] (2011, Characteristics and use of infrared detectors. *Technical Information SD-12*. Available: http://sales.hamamatsu.com/assets/applications/SSD/infrared_kird9001e04.pdf
- [24] E. L. Dereniak and G. D. Boreman, *Infrared Detectors and Systems*. New York,: John Wiley & Sons, 1996.
- [25] E. H. Sargent, "Infrared Quantum Dots," *Advance Materials*, vol. 17, pp. 515-522, 2005.
- [26] V. I. Klimov, *Semiconductor and metal nanocrystals : synthesis and electronic and optical properties*. New York: Marcel Dekker Inc. , 2004.
- [27] C. B. Murray, D. J. Norris, and M. G. Bawendi, "SYNTHESIS AND CHARACTERIZATION OF NEARLY MONODISPERSE CDE (E = S, SE, TE) SEMICONDUCTOR NANOCRYSTALLITES," *Journal of the American Chemical Society*, vol. 115, pp. 8706-8715, Sep 1993.
- [28] E. H. Sargent, "Infrared quantum dots," *Advanced Materials*, vol. 17, pp. 515-522, Mar 2005.
- [29] E. J. Klem, J. S. Lewis, and D. Temple, "Multispectral UV-Vis-IR imaging using low-cost quantum dot technology," in *Infrared Technology and Applications Xxxvi, Pts 1 and 2*. vol. 7660, B. F. Andresen, G. F. Fulop, and P. R. Norton, Eds., ed, 2010.
- [30] G. M. Whitesides and J. C. Love, *Scientific American*, vol. 285, pp. 38-47, 2001.
- [31] G. Konstantatos and E. H. Sargent, "Nanostructured materials for photon detection (vol 5, pg 391, 2010)," *Nature Nanotechnology*, vol. 5, Dec 2010.
- [32] E. L. Dereniak and D. G. Crowe, *Optical Radiation Detectors*. New York: John Wiley & Sons, 1984.
- [33] R. H. Hamstra and P. Wendland, "Noise and Frequency Response of Silicon Photodiode Operational Amplifier Combination," *N. Appl. Opt.*, vol. 11, p. 1539, 1972.
- [34] D. N. B. Hall, R. S. Aikens, R. Joyce, and T. W. McCurnin, "Johnson Noise Limited Operation of Photovoltaic InSb Detectors," *Appl. Opt.*, vol. 14, pp. 450-453, 1975.
- [35] D. C. Oertel, M. G. Bawendi, A. C. Arango, and V. Bulovic, "Photodetectors based on treated CdSe quantum-dot films," *Appl. Phys. Lett.*, vol. 87, pp. 21-35, 2005.

- [36] G. Konstantatos, "Ultrasensitive solution-cast quantum dot photodetectors," *Nature Nanotechnology*, vol. 442, pp. 180-183, 2006.
- [37] G. Konstantatos, J. Clifford, L. Levina, and E. H. Sargent, "Sensitive solution-processed visible-wavelength photodetectors," *Nature Photonics*, vol. 1, pp. 531-534, 2007.
- [38] M. Boberl, M. V. Kovalenko, S. Gamerith, E.J.W.List, and W. Heiss, "Inkjet-printed nanocrystal photodetectors operating up to 3 μm wavelengths," *Advanced Materials* vol. 19, pp. 3574-3578, 2007.
- [39] H. Y. Chen, M. K. F. Lo, G. Yang, H. G. Monbouquette, and Y. Yang, "Nanoparticle-assisted high photoconductive gain in composites of polymer and fullerene," *Nature Nanotechnology*, vol. 3, pp. 543-547, 2008.
- [40] S. H. e. al., "Smooth-morphology ultrasensitive solution-processed photodetectors," *Advanced Materials*, vol. 20, pp. 4398-4402 2008.
- [41] G.Konstantatos, L. Levina, A. Fischer, and E. H. Sargent, "Engineering the temporal response of photoconductive photodetectors via selective introduction of surface trap states," *Nano Letters*, vol. 8, pp. 1446-1450, 2008.
- [42] V. Sukhovatkin, S. Hinds, L. Brzozowski, and E. H. Sargent, "Colloidal quantum-dot photodetectors exploiting multiexciton generation," *Science*, vol. 324, pp. 1542-1544, 2009.
- [43] J. P. C. e. al., "Fast, sensitive and spectrally tuneable colloidal-quantum-dot photodetectors," *Nature Nanotechnology*, vol. 4, pp. 40-44, 2009.
- [44] T. R. e. al., "Near-infrared imaging with quantum-dot-sensitized organic photodiodes," *Nature Photonics*, vol. 3, pp. 332-336, 2009.
- [45] X. G. e. al., "High-detectivity polymer photodetectors with spectral response from 300 nm to 1450 nm," *Science*, vol. 325, pp. 1665-1667, 2009.
- [46] E. J. Klem and J. S. Lewis, "Multispectral UV-Vis-IR imaging using low-cost quantum dot technology," *Infrared Technology and Application XXXVI Proc. of SPIE*, vol. 7660, 2010.
- [47] S. L. Calvez, H. Bourvon, H. Kanaan, S. M.-d. Gatta, C. Philippot, and P. Reiss, "Enabling NIR imaging at room temperature using quantum dots," *Infrared Sensors, Devices and Applications*, 2011.
- [48] G. Sarasqueta, K. R. Choudhury, J. Subbiah, and F. So, "Organic and Inorganic Blocking Layers for Solution-Processed Colloidal PbSe Nanocrystal Infrared Photodetectors," *Adv. Funct. Mater.*, vol. 21, pp. 167-171, 2011.
- [49] D. Mocatta, G. Cohen, J. Schattner, O. Millo, E. Rabani, and U. Banin, "Heavily Doped Semiconductor Nanocrystal Quantum Dots," *Science*, vol. 332, pp. 77-81, 2010.
- [50] D. Cui, J. Xu, G. Paradee, S. Xu, and A. Y. Wang, "Developing PbSe/PbS core-shell nanocrystals quantum dots toward their potential heterojunction applications," *Journal of Experimental Nanoscience*, vol. 2, pp. 13-21, 2007.
- [51] *Evident Technologies*. Available: <http://www.evidenttech.com/>
- [52] M. A. Hines and G. D. Scholes, "Colloidal PbS Nanocrystals with Size-Tunable Near-Infrared Emission: Observation of Post-Synthesis Self-Narrowing of the Particle Size Distribution," *Advanced Materials*, vol. 15, pp. 1844-1849, 2003.
- [53] J. P. Clifford, K. W. Johnston, L. Levina, and E. H. Sargent, "Schottky barriers to colloidal quantum dot films," *Appl. Phys. Lett.*, vol. 91, pp. 2531171-2531173, 2007.
- [54] *Teknoma A.S.* Available: <http://www.teknoma.net>

- [55] K. W. Johnston, A. G. Pattantyus-Abraham, J. P. Clifford, S. H. Myrskog, S. Hoogland, H. Shukla, E. J. D. Klem, L. Levina, and E. H. Sargent, "Efficient Schottky-Quantum-Dot Photovoltaics: The Roles of Depletion, Drift, and Diffusion," *Appl. Phys. Lett.*, vol. 92, p. 122111(3), 2008.
- [56] J. Tang and E. H. Sargent, "Infrared Colloidal Quantum Dots for Photovoltaics: Fundamentals and Recent Progress," *Advanced Materials*, vol. 23, pp. 12-29, 2011.
- [57] K. S. Jeong, J. Tang, H. Liu, J. Kim, A. W. Schaefer, K. Kemp, L. Levina, X. H. Wang, S. Hoogland, R. Debnath, L. Brzozowski, E. H. Sargent, and J. B. Asbury, "Enhanced Mobility-Lifetime Products in PbS Colloidal Quantum Dot Photovoltaics," *Acs Nano*, vol. 6, pp. 89-99, Jan 2012.
- [58] C. B. Murray, C. R. Kagan, and M. G. Bawendi, "Synthesis and characterization of monodisperse nanocrystals and close-packed nanocrystal assemblies," *Annu. Rev. Mater. Sci.*, vol. 30, pp. 545-610, 2000.
- [59] W. Commons. (2006, Oleic acid 3D Available: <http://en.wikipedia.org/wiki/File:Oleic-acid-3D-vdW.png>)
- [60] J. M. Luther, M. Law, M. C. Beard, Q. Song, M. O. Reese, R. J. Ellingson, and A. J. Nozik, "Schottky Solar Cells Based on Colloidal Nanocrystal Films," *Nano Letters*, vol. 8, pp. 3488-3492, 2008.
- [61] G. I. Koleilat, L. Levina, H. Shukla, S. H. Myrskog, S. Hinds, A. G. Pattantyus-Abraham, and E. H. Sargent, "Efficient, Stable Infrared Photovoltaics Based on Solution-Cast Colloidal Quantum Dots," *ACS Nano*, vol. 2, pp. 833-840, 2008.
- [62] D. V. Talapin and C. B. Murray, "PbSe Nanocrystal Solids for n- and p-Channel Thin Film Field-Effect Transistors.," *Science*, vol. 310, pp. 86-89, 2005.
- [63] B. Sun, A. T. Findikoglu, M. Sykora, D. J. Werder, and V. I. Klimov, "Hybrid Photovoltaics Based on Semiconductor Nanocrystals and Amorphous Silicon," *Nano Letters*, vol. 9, pp. 1235-1241, 2009.
- [64] G. I. Koleilat, L. Levina, H. Shukla, S. H. Myrskog, S. Hinds, A. G. Pattantyus-Abraham, and E. H. Sargent, "Efficient, Stable Infrared Photovoltaics Based on Solution-Cast Colloidal Quantum Dots," *Acs Nano*, vol. 2, pp. 833-840, 2008.
- [65] R. Debnath, J. Tang, D. A. Barkhouse, X. Wang, A. G. Pattantyus-Abraham, L. Brzozowski, L. Levina, and E. H. Sargent, "Ambient-Processed Colloidal Quantum Dot Solar Cells via Individual Pre-Encapsulation of Nanoparticles," *Journal of American Chemical Society*, vol. 132, pp. 5952-5953, 2010.
- [66] W. Gang, Liu Hongyu, Z. Chao, Y. Bailiang, and H. Ximin, "Preparation and Characterization of Low Resistance and High Transmittance ITO Films," *Chinese Journal of Liquid Crystals and Displays*, vol. 149, p. 23, 1999.
- [67] A. Antony, M. Nisha, R. Manoj, and M. K. Jayaraj, "Influence of target to substrate spacing on the properties of ITO thin films," *Applied Surface Science*, vol. 225, pp. 294-301, 2004.
- [68] N. G. Patel, P. D. Patel, and V. S. Vaishnav, "Indium tin oxide (ITO) thin film gas sensor for detection of methanol at room temperature," *Sensors and Actuators B: Chemical*, vol. 96, pp. 180-189, 2003.
- [69] Z. Erjing, Z. Weijia, L. Jun, Y. Dongjie, H. J. Jacques, and Z. Jing, "Preparation of ITO thinfilms applied in nanocrystalline silicon solar cells," *Vacuum*, vol. 86, pp. 290-294, 2011.

- [70] X. D. Liu, E. Y. Jiang, and D. X. Zhang, "Electrical transport properties in indium tin oxide films prepared by electron-beam evaporation " *Journal of Applied Physics*, vol. 104, p. 073711, 2008.
- [71] H. C. Lee, J. Y. Seo, Y. W. Choi, and D. W. Lee, *Vacuum*, vol. 72, pp. 269-276, 2004.
- [72] J. O. Park, J. H. Lee, J. J. Kim, S. H. Cho, and Y. K. Cho, *Thin Solid Films* vol. 474, pp. 127-132, 2005.
- [73] J. Kim, K. Jeon, G. Kim, and S. Lee, "Electrical, structural, and optical properties of ITO thin films prepared at room temperature by pulsed laser deposition," *Applied Surface Science*, vol. 252, pp. 4834-4837, 2006.
- [74] D. Kim, Y. Han, J. S. Cho, S. K. Koh, and . *Thin Solid Films*, vol. 377, pp. 81–86, 2000.
- [75] A. Amaral, P. Brogueira, and C. N. d. Carvalho, *Surf. Coat. Technol.*, vol. 125, pp. 151-156, 2000.
- [76] A. E. Hichou, A. Kachouane, J. L. Bubendorff, J. E. M. Addou, M. Troyon, and A. Bougrine, *Thin Solid Films*, vol. 458, pp. 263-268, 2004.
- [77] Y. C. Park, Y. S. Kim, H. K. Seo, S. G. Ansari, and H. S. Shin, *Surf. Coat. Technol.*, vol. 161, pp. 62-69, 2000.
- [78] H. Zhou, D. Yi, and X. Yang, *Surface Technology*, vol. 35, 2006.
- [79] L. Gupta, A. Mansingh, and P.K.Srivastava, "Band Gap Narrowing and the Band Structure of Tin Doped Indium Oxide Films," *Thin Solid Films*, vol. 176, pp. 33-44, 1989.
- [80] I. Elfallal, R.D.Rilington, and A. E. Hill, "Formation of a statistical thermodynamic model for the electron concentration in heavily doped metal oxide semiconductors applied to the tin-doped indiumoxide system," *Thin solid films*, vol. 223, pp. 303-310, 1993.
- [81] M. W. Davidson. Tungsten-Halogen Incandescent Lamps. Available: <http://zeiss-campus.magnet.fsu.edu/articles/lightsources/tungstenhalogen.html>
- [82] F. P. G. d. Arquer, F. J. Beck, and G. Konstantatos, "Absorption Enhancement in Solution Processed Metal-Semiconductor Nanocomposites," *Optics Express*, vol. 19, p. 21038, 2011.
- [83] K. Nakayama, K. Tanabe, and H. A. Atwater, "Plasmonic nanoparticle enhanced light absorption in GaAs solar cells," *Applied Physics Letters*, vol. 93, p. 121904, 2008.
- [84] B. P. Rand, P. Peumans, and S. R. Forrest, "Long-range absorption enhancement in organic tandem thin-film solar cells containing silver nanoclusters," *Applied Physics*, vol. 96, p. 7519, 2004.
- [85] F. P. G. d. Arquer, F. J. Beck, M. Bernechea, and G. Konstantatos, "Plasmonic light trapping leads to responsivity increase in colloidal quantumdot photodetectors," *Applied Physics Letters*, vol. 100, p. 043101, 2012.

APPENDIX I

ITO DEPOSITION OPTIMIZATION

Description of Sputtering System

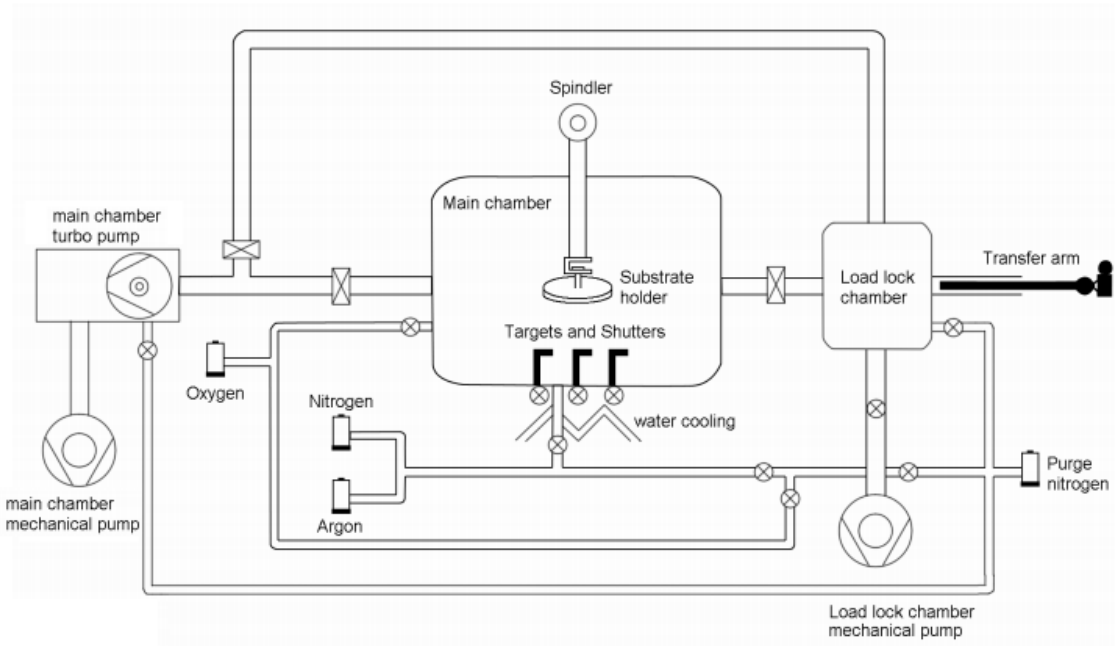


Figure 72. Schematic of the sputtering system

The sputtering system used in this work is a systems supplied by a local company (Teknoplazma). The system has both RF and DC power supply and can do RF and DC magnetron sputtering. The schematic of the system is given in Figure 72. The system consist of one main chamber in which the sputter deposition process is done and a load lock chamber that is used to load samples without braking the vacuum. The substrate holder is placed on upper part of the main chamber. It is connected to a spindle motor that rotate it during the deposition process in order to improve uniformity.

The targets and shutters to close these targets are placed on the bottom part of the main chamber. The system is compatible with 2'' diameter target sizes and it can be loaded up to three targets. Main chamber mechanical pump and turbo pump is connected to the main chamber through a variable gate valve and its position can be adjusted from 0 to 1000. The load lock chamber also has a mechanical pump that is

used to take the pressure of the LLC to vacuum levels in order to open the valve between main chamber and load lock chamber to load the samples. There is a transfer arm on the load lock side and the samples are manually loaded to main chamber.

There are four gas inlets to the system; oxygen, high purity nitrogen, argon and purge nitrogen. The first three is connected to the system through mass flow controllers (MFC). Ar MFC has a range from 0 sccm to 100 sccm, O₂ can be adjusted in the range from 0 to 20 sccm and Argon has a MFC that works in the range of 0 to 50 sccm. Purge nitrogen is used to vent both load lock chamber and the main chamber.

The sputter system has two power supplies; one RF and one DC. Both RF and DC magnetron sputtering can be done on the system by connecting DC power supply to the target for DC magnetron sputtering and by connecting RF power supply to the target and DC power supply to the sample holder for RF magnetron sputtering. The range of RF power is in between 0 to 300W and the DC power can be applied up to 400W.

In this work, only DC magnetron sputtering is used up to 350 W power levels and various flows of Ar and O₂ gases are used in the plasma depending on the different processes.

Sputter Processing of ITO

The glass or silicon samples are cleaned through acetone, methanol, isopropanol and DI rinses in ultrasonic cleaner prior to the deposition. The ITO thin films have been prepared at room temperature (300K) by reactive DC magnetron sputtering from a metallic, In:Sn – 90:10 wt%, 99.99% purity, 2'' diameter, 0.125'' thick, circular targets. The sputter chamber is initially evacuated to a base pressure of 1x10⁻⁶ mbar. The flow rates of argon (sputter gas) and oxygen (reactive gas) are controlled through independent mass flow controllers. Ar and O₂ flow rates are varied throughout different samples. The chamber pressure, in the presence of sputter and reactive gasses, is adjusted to desired pressure using variable gate valve. The deposition time is generally kept at 10 min, resulting film thicknesses around 240 nm, depending on the power. DC powers from 50W to 350W are applied to different samples but the main intention was to keep power levels low.

Characterization of ITO coated samples

As a first step, the thicknesses of ITO films are measured after the deposition step. KLA Tencor's P6 Surface Profilometer is used to measure the thickness. For step height measurements in order to find the thickness of the film some part of the sample is covered with carbon tapes and no deposition occur under these films. In this manner, the step height between the substrate and the film can be measured.

The electrical characterization of the films is done using 4 point probe measurements in order to calculate films sheet resistance and resistivity. Cascade Microsystems' C4S four point probe is used together with Keithley current source and nano-voltmeter. Resistivity, ρ , of the layer has been measured with a 4-point-probe, four precisely aligned probes that make electrical contact with a sample as seen in Figure 73. In this method, a known current I is applied from a power supply to the sample through probes 1 and 4. The voltage drop due to current flow is then measured by a voltmeter connected across probes 2 and 3. Measured resistance, $V/I = R$, and the resistivity of the sample are related to the equation I.1 as following,

$$\rho = \frac{\pi t V}{\ln 2 I} = 4.532 \frac{tV}{I} \quad (\text{I.1})$$

where r is the sample thickness. Equation I.1 solves electrostatic problems associated with the spreading of current flow from the two outside probes as shown in Figure 73. Units of the value of ρ are Ohm.cm ($\Omega\cdot\text{cm}$). 4PP is also used to derive the sheet resistance R_s . If the thickness of the Equation I.1 is unknown, then;

R_s has the units of Ohms/square (Ω/\square), the derivation of which can be understood if one considers that the electrical resistance of an arbitrary section of the film is related to its resistivity and to the physical dimensions of thickness, length and width by the equation I.2

$$R = \frac{\rho l}{t b} \quad (\text{I.2})$$

where l and b is the width and length of the rectangular section and t is the thickness of the layer. If the length and width of the rectangular section are equated, making the rectangle a square, the resulting value of resistance is a function of thickness and resistivity only shown in the equation I.3;

$$R = \frac{\rho}{t} = R_s \quad (I.3)$$

$$R_s = 4.532 V/I \quad (I.4)$$

Optical characterization of the sputter deposited ITO layers is done by UV-VIS-NIR spectrometer. The ITO coated samples are placed into the system, their substrates are placed as reference and transmission spectrum is given by the equipment. We are interested in wavelengths around 1500 nm, so the measurement range of the spectrometer is adjusted to the range 700 -2000 nm.

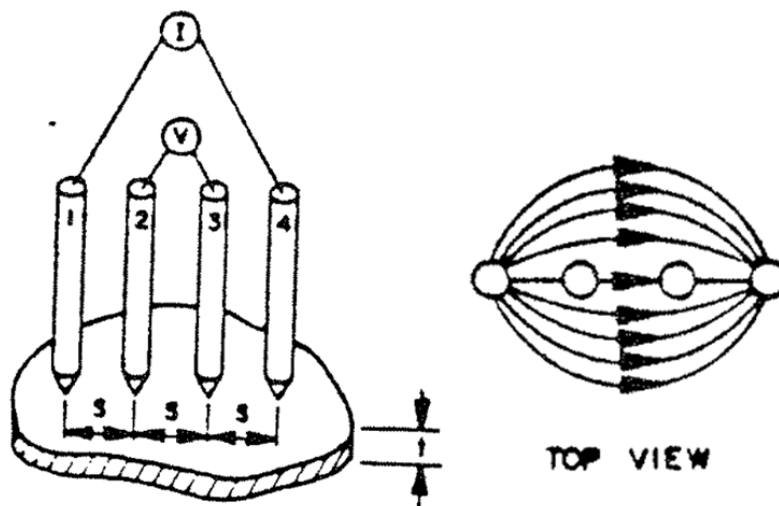


Figure 73. A 4PP consists of equally spaced tungsten carbide points that are brought into contact with a layer (left). The spreading of current flow between probes 1 and 4 and the resulting electrostatic fields must be considered in calculating semiconductor resistivity from 4-point probe measurements

Results

Sample #1-2, low power DC magnetron sputtering

The ITO deposition trials start with a standard low power DC magnetron deposition process. After the chamber base pressure reached to 1×10^{-6} mbar, Ar flow is

adjusted to 35 sccm and variable gate valve is adjusted to position 360/1000, supplying main chamber pressure of $1,7 \times 10^{-2}$ mbar. Very low DC power, 50 W, is applied to Indium tin oxide (90%_{wt} In₂O₃, 10%_{wt} SnO₂) target. The deposition time is kept at 5 min. resulted in 35 nm which is below our thickness aim. This sample presents 5.89 MΩ/□ sheet resistance and its resistivity is calculated as 20,6 Ω.cm which is too high for our requirements. However its transmittance at 1450 nm is very close to 100%.

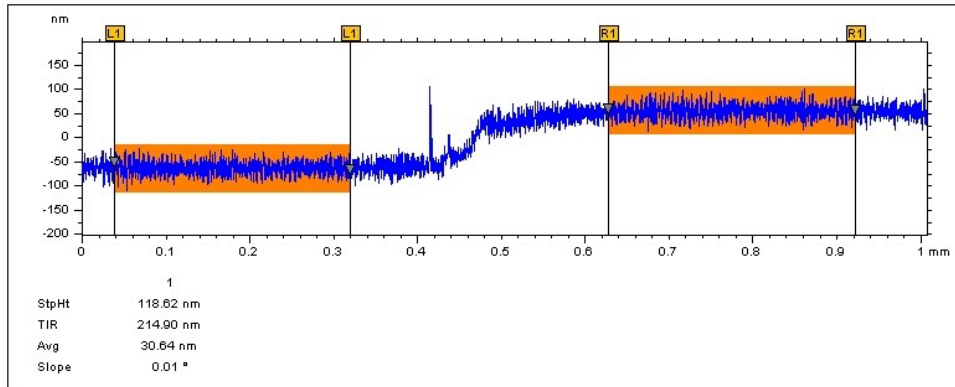


Figure 74. Thickness of sample #2 measured by surface profilometer

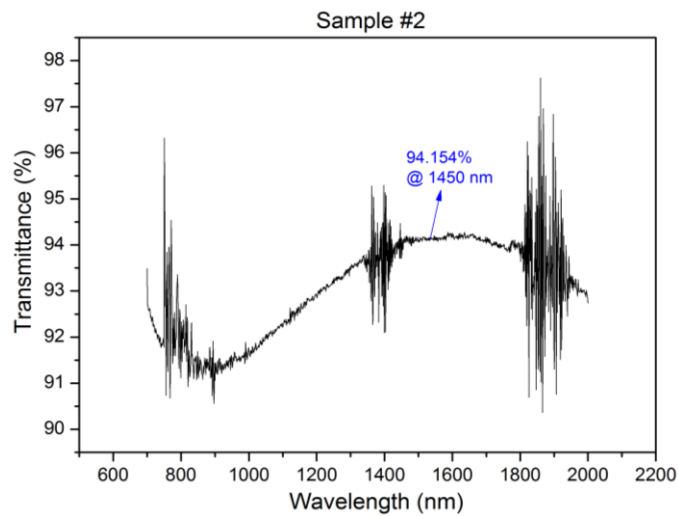


Figure 75. Sample #2 Transmittance between 700 nm – 2000 nm

In order to have a thicker layer, another sample is prepared with a deposition time of 25 min while keeping all the other parameters same as sample #1. Increasing deposition time from 5 min to 25 min the layer thickness is increased from 35 nm to 118 nm as shown in Figure 74. Sheet resistance is measured by 4PP as 19,487 kΩ/□ and the resistivity is extracted as $2,3 \times 10^{-1}$ Ω.cm. The transmission characteristic is measured

by spectrometer and is shown in Figure 75. At 1450 nm the sample give 94.154% Transmittance.

Sample # 3, Moderate power DC magnetron sputtering

Since the resistivity and sheet resistance performance of sample #1 and #2 is poor, the power of sputtering is increased to 100 W. The chamber pressure and Ar flow are kept same as previous samples, at $1,7 \times 10^{-2}$ mbar and 35 sccm respectively. The sample is sputter deposited from ITO target for 15 minute. The thickness achieved for 15 min. deposition is 280 nm as shown in Figure 76.

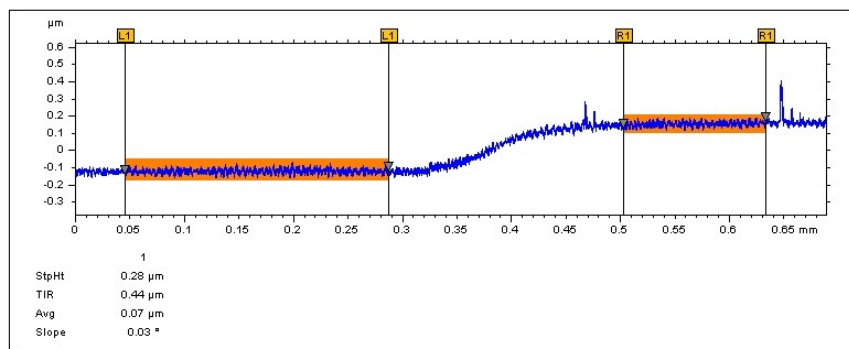


Figure 76. Thickness of sample #3 measured by surface profilometer

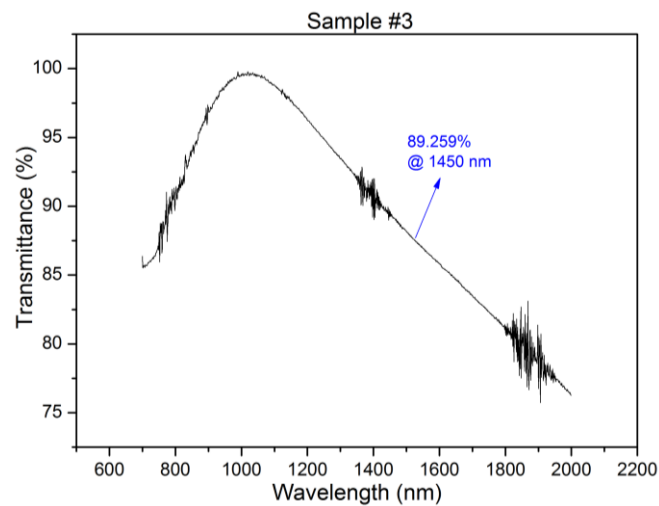


Figure 77. Transmission graph of sample #3 between 700-2000 nm wavelengths

By doubling the sputter deposition DC power, an improvement is observed in sheet resistance and resistivity such that the sheet resistance is decreased to $4.269 \text{ k}\Omega/\square$

and the resistivity is decreased to $1.2 \times 10^{-1} \Omega \cdot \text{cm}$. However, transmittance decreased a bit to 89.259 % at 1450 nm.

Sample #4 and #5, higher power lower pressure DC magnetron sputtering

As it is observed in sample #3 and #4 that increasing the power improves the resistivity, in sample #4 and #5 the sputtering DC power is increased to 200W. In sample #4 the Ar flow is decreased to 30 sccm and the chamber pressure in deposition is adjusted to 7×10^{-3} mbar by adjusting the position of the variable valve to 420. The sputtering time is kept at 5 min resulting ITO layer thickness of 150 nm as seen in Figure 78. Increasing the sputtering power to 200W and also decreasing the chamber pressure resulted a big improvement in sheet resistance as $113.3 \Omega/\square$ and in resistivity as $1,7 \times 10^{-3} \Omega \cdot \text{cm}$. However, it decreased the transmittance to 70,616 % as seen in Figure 80.

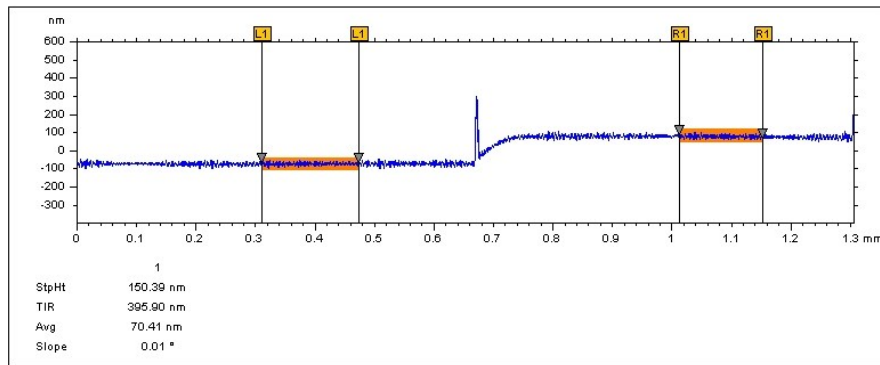


Figure 78. Thickness of sample #4 measured by surface profilometer

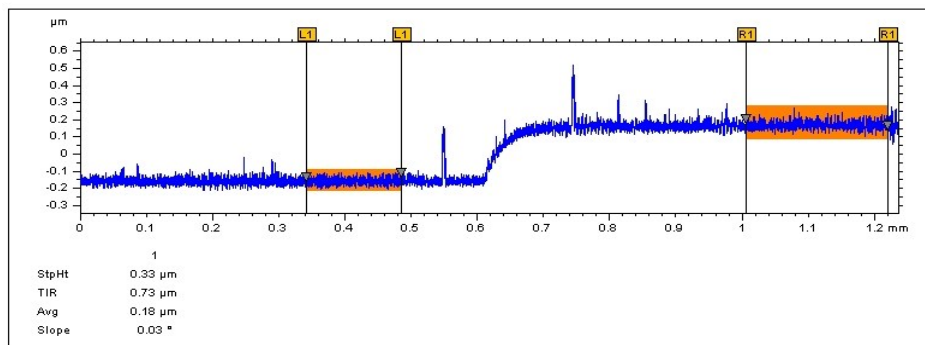


Figure 79. Thickness of sample #5 measured by surface profilometer

When processing sample #5, the process parameters of sample #4 is repeated by only increasing the chamber pressure slightly to 8×10^{-3} mbar by changing the variable gate valve position to 410 and by increasing the deposition time from 5 min to 10 min. 10 min deposition time resulted 330 nm film thickness as shown in Figure 80. Thicker film resulted an improvement in sheet resistance such as, 45,32 Ω/\square and a slight improvement in resistivity such as 1.5×10^{-3} $\Omega\cdot\text{cm}$, however it resulted poor transmittance behavior as shown in Figure 81. Thicker film resulted transmittance of 47,011 % at 1450 nm.

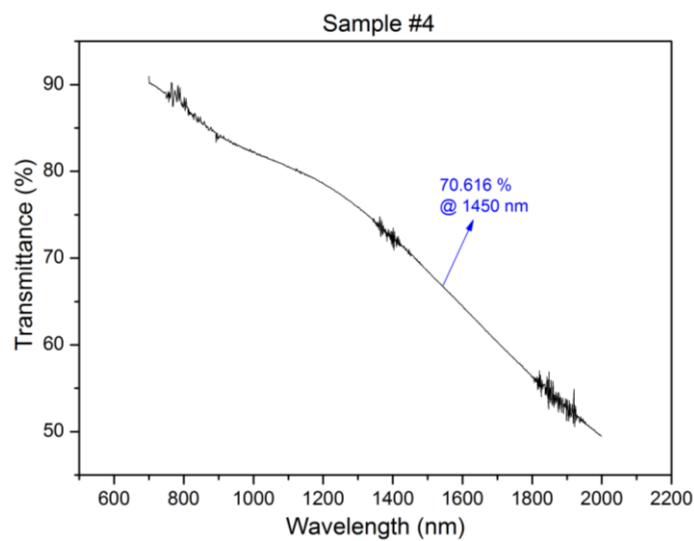


Figure 80. . Transmittance graph of sample #4 between 700-2000 nm wavelengths

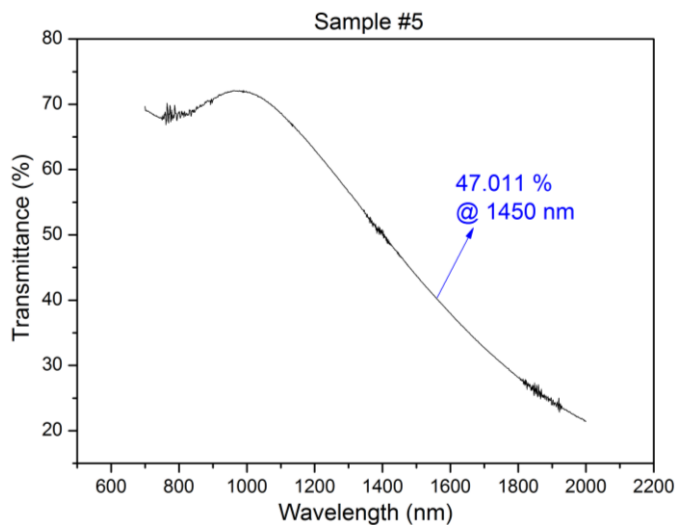


Figure 81. Transmittance graph of sample #5 between 700-2000 nm wavelengths.
Transmittance decreased dramatically to 47.011% at 1450 nm

Sample #6, DC magnetron sputtering with Ar and O₂

In sample #6, in order to increase the O₂ concentration in the film and thus the transmittance of the layer, O₂ is introduced into the process chamber together with Ar during the sputtering process. The DC power is selected as 200 W. For 6.5 ratio between Ar and O₂, Ar flow rate is increased to 77 sccm and 5 sccm of O₂ is flowed together with Ar. The position of the variable gate valve is increased to 700/1000 in order to achieve 1.1×10^{-2} mbar chamber pressure. The sputtering process takes 7,5 minute resulting 193 nm thickness as seen in Figure 82.

Comparing to sample #4, using O₂ in the process improved the transmittance to 78.802 % as seen in Figure 83. However, introducing O₂ and increased chamber pressure resulted increased sheet resistance such as 1033.3 Ω/\square and increased resistivity of 1.99×10^{-2} $\Omega\cdot\text{cm}$ which is very high comparing to our requirements.

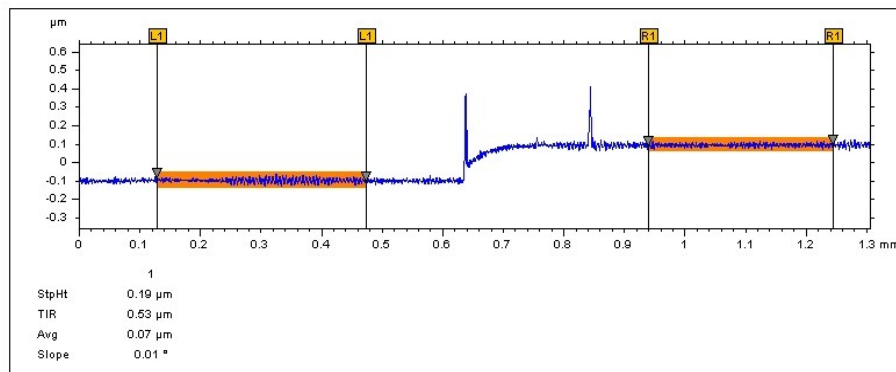


Figure 82. Measured thickness of sampe #6.

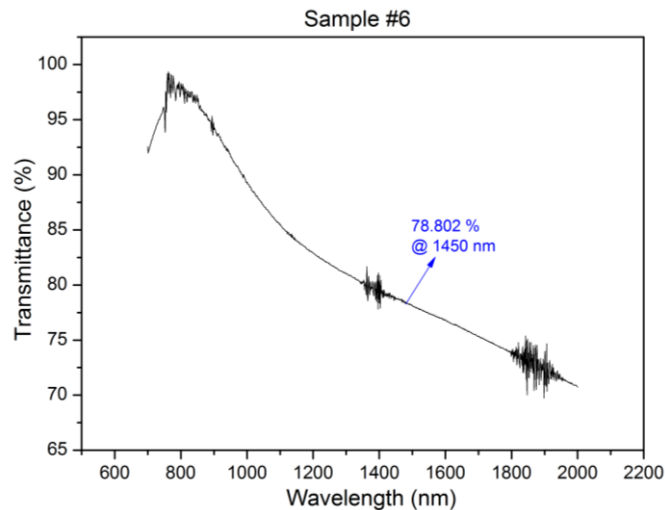


Figure 83. Transmittance graph of sample #6 between 700-2000 nm wavelength

Sample #7, High power, low pressure DC magnetron sputtering with Ar and O₂

In order to improve the resistivity comparing to sample #5 and 6, the DC sputtering power is increased to 350 W. Also previously it is observed that decreasing the chamber pressure during sputtering improves the resistivity, so that the pressure is kept at 8×10^{-3} mbar during sputtering. Ar/O₂ ratio is decreased to 5.3 and the sample is sputter deposited from ITO target for 3.5 min resulting 150 nm ITO film as seen in Figure 84. High power and relatively low pressure is resulted in improved resistivity comparing to sample #6. The sheet resistance is measured as $285.5 \Omega/\square$ and the resistivity is measured as $4,28 \times 10^{-3} \Omega.cm$. Also we can observe the positive effect of using O₂ in enhancement of transmittance comparing the transmittance result of sample #7 that is shown in Figure 85, with the sample #4 that has exactly the same thickness with sample #7. Sample #4 that is deposited with 200 W at sample pressure using Ar plasma resulted 70 % transmittance whereas sample #7, deposited with 350 W power using Ar/O₂ mixture resulted in 88.486% transmittance at 1450 nm, however, although the deposition power is high in sample #7, which is supposed to achieve lower resistivity than sample #4, it is higher due to the O₂ introduction to plasma. Moreover applying 350 W power to the ITO target resulted damage in the target so the power level have to be decreased.

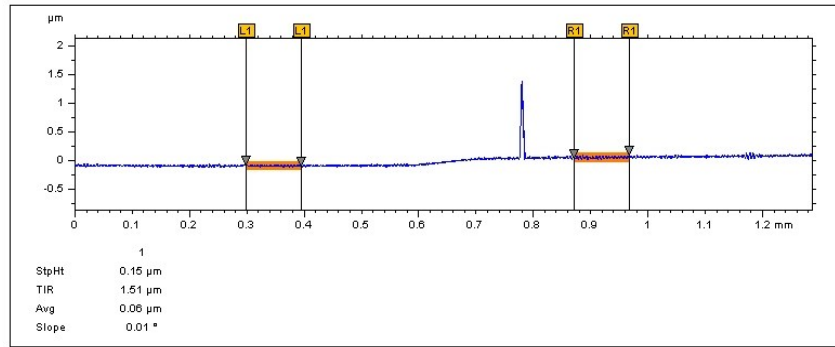


Figure 84. 4 min sputtering at 350 W DC power resulted 150 nm thicknesses for sample #6

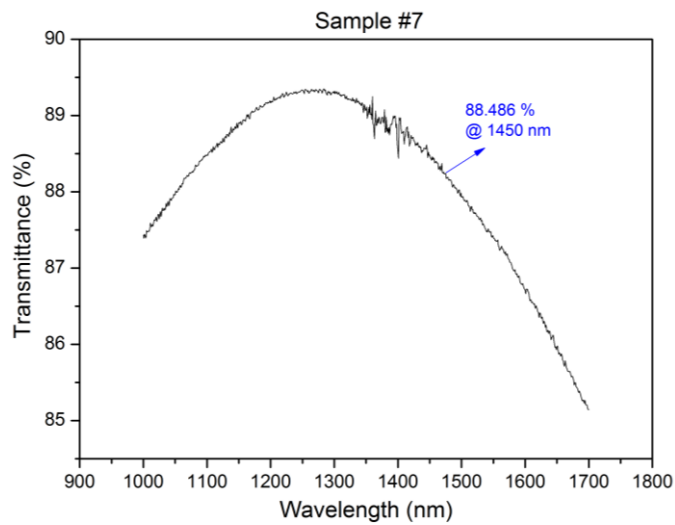


Figure 85. Transmittance graph of sample #7 in the range between 1000-1700 nm

Sample #8, Moderate power, moderate pressure, low O₂ ratio

In sample #8, the DC power is lowered to 150 W and the chamber pressure is kept at 1×10^{-2} mbar during deposition by adjusting the variable gate valve position to 450/1000. The O₂ ratio in the deposition is decreased to 3 by setting Ar flow to 70 sccm and O₂ flow to 2 sccm. Total sputtering time is 10 min resulting 231 nm thick of ITO layer as shown in Figure 86.

Transmittance of sample #8 is good as seen in Figure 87, which is 88.234% at 1450 nm. However it has resulted really poor sheet resistance and resistivity characteristics due to low power, moderate pressure and presence of O₂ concentration.

The sheet resistance is measured as $172 \text{ k } \Omega/\square$ and the resistivity is calculated as $3,98 \text{ } \Omega.\text{cm}$ which is too high for our requirements.

Sample #9, Low power with O₂ pre-sputtering

In the previous samples, it has been observed that introducing O₂ to the chamber during sputtering improves the transmission of the layer; however, at the same time it reduces the conductivity of the layer and thus resistivity values increase. It has been tried to find an optimum point that the resistivity values are below $1 \times 10^{-3} \text{ mbar}$ and the transmittance is higher than 70%, but this point could not be achieved using pure Ar plasma or a mixture of Ar/O₂ due to the limitations of the sputtering system used. In order to overcome this, in the pre-sputtering phase, O₂ is introduced into the chamber which improves the ITO target oxidation state. After pre-sputtering period, the sputtering is done in pure Ar plasma without O₂ flow.

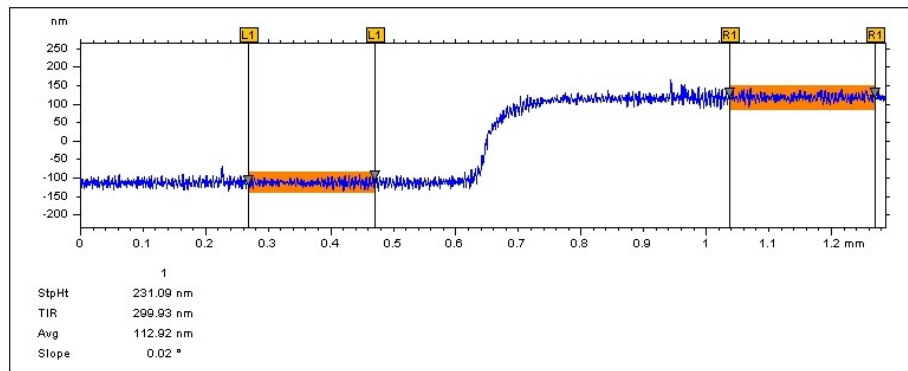


Figure 86. Thickness measurement of sample #8

Sample #9 is deposited with aforementioned method. The sputtering power is adjusted to 80 W, chamber pressure is kept at $1.7 \times 10^{-2} \text{ mbar}$ by adjusting the variable valve position to 360. Before deposition, 5 min. pre-sputtering is applied with same process parameter and by only introducing 5 sccm O₂ into the chamber. After 5 min. pre sputtering the deposition is started in absence of O₂ gas and sputtering time was 5 min resulting in 75 nm thickness. The transmittance of the layer was quite high as seen in Figure 88. At 1450 nm wavelength it gives a transmittance of 94.498 % and this good result also depends on layer being thin. Looking to the 4PP measurement results, the

sheet resistance is $2.356 \text{ k } \Omega/\square$ and the resistivity is $5.98 \times 10^{-3} \text{ } \Omega\cdot\text{cm}$. The resistivity value is still high and further optimization is required in pressure and power parameters.

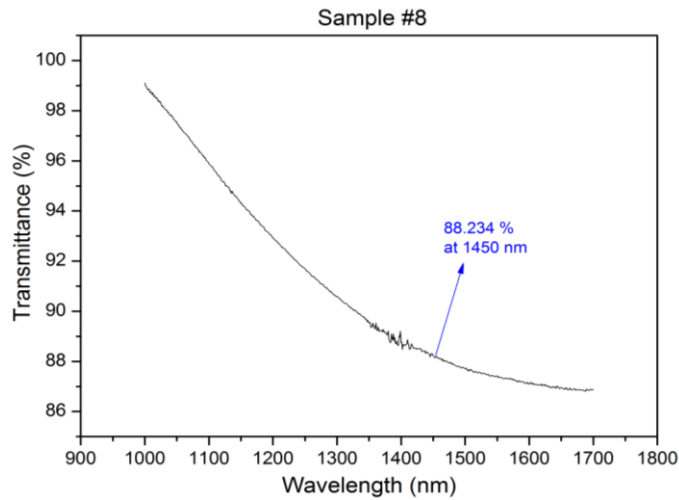


Figure 87. Transmittance graph of sample #8 in the range between 1000-1700 nm

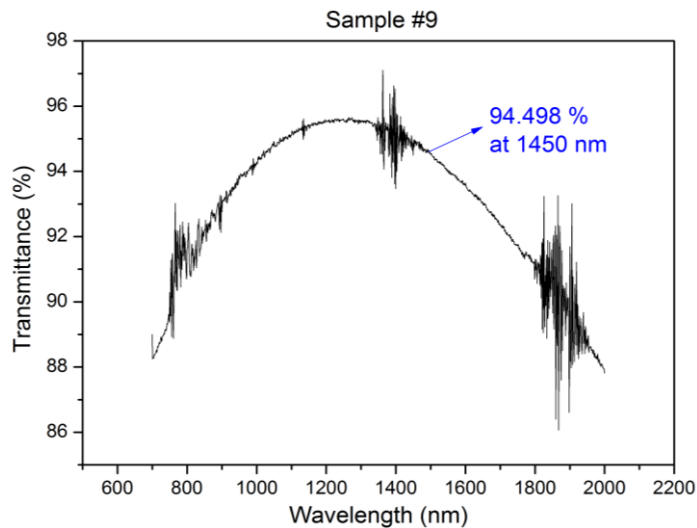


Figure 88. Transmittance graph of sample #9 between 700 nm and 2000 nm

Sample #10,#11, and #12, pre-sputtering with O₂, pressure and power optimization

In samples #10,#11 and #12, different DC power between 80W to 200W is applied at various chamber pressures ranging from 1.4×10^{-2} to 1×10^{-2} . Sample #10 is deposited with 150 W DC power and the chamber pressure is kept at 1.4×10^{-2} mbar during deposition which takes 10 min. The Ar flow is set to 25 sccm. Also 3 min pre

sputtering with 25 sccm Ar / 2 sccm O₂ is done in order to oxidize the target. Total thickness is measured as 222 nm as shown in Figure 89.

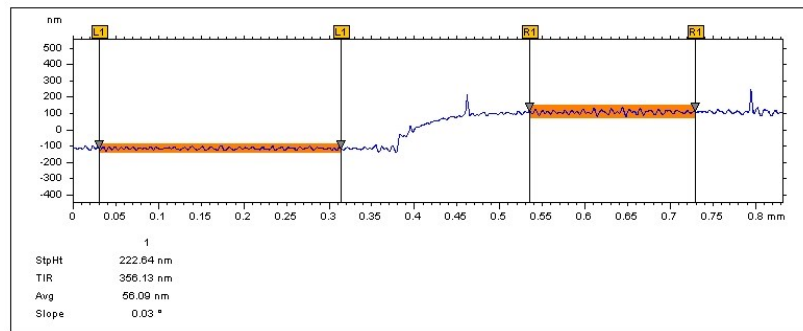


Figure 89. Thickness of sample #10 is measured as 222 nm.

The resistivity of the sample was improved to $4.73 \times 10^{-3} \Omega/\square$ and the sheet resistance is measured as 213 Ω/\square . The transmittance is a bit low, such as 73.929 % at 1450 nm as shown in Figure 90.

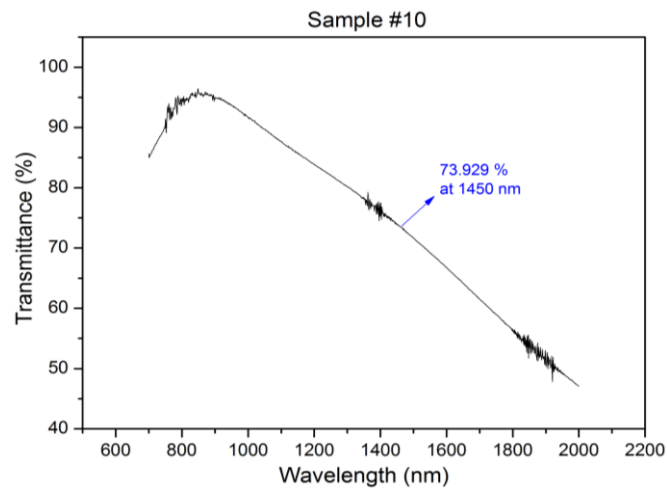


Figure 90. Transmittance graph of sample #10

In sample #11 lower power is applied for deposition such as 80 W and the chamber pressure is decreased to 1.1×10^{-2} with 35 sccm Ar flow. 3 min. pre-sputtering is done at 1.4×10^{-2} mbar with 35 sccm Ar and 5 sccm O₂. 10 min. deposition resulted in 110 nm thickness. The sheet resistance increased slightly to 543 Ω/\square and the resistivity to $5,98 \times 10^{-3} \Omega/\square$. The transmittance is measured as 85% at 1450 which is also improved depending on the thin layer of ITO.

In sample # 12 the power increased further to 200 W and the pressure is dropped to 1×10^{-2} mbar. Higher power depositions resulted lower transmittance but and lower resistivity. Transmittance is tried to be increased by applying 3 min. pre-sputtering with 35 sccm Ar / 5 sccm O₂ flow. 7 min deposition resulted 146 nm film thickness. Measured sheet resistance was 181 Ω/\square and measured resistivity was $2,54 \times 10^{-3}$. Sample achieved 72 % transmittance at 1450 nm as shown in Figure 93.

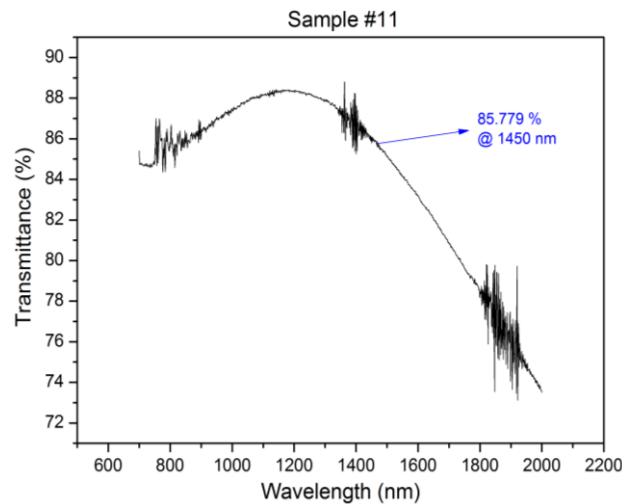


Figure 91. Transmittance graph of sample #11

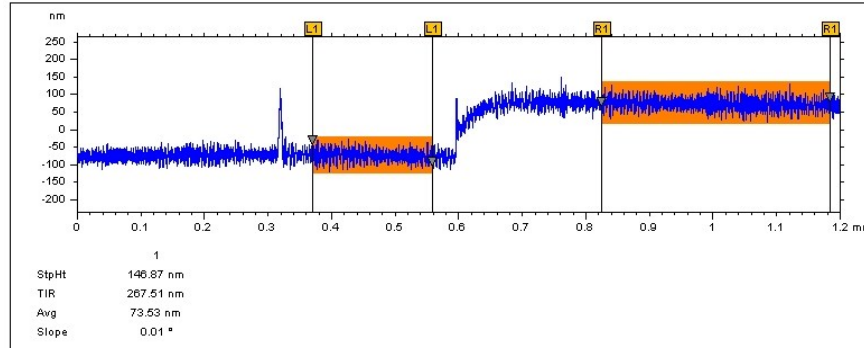


Figure 92. Thickness of sample #12. 7 min deposition at 200W resulted in 146 nm thickness

Sample #13, moderate power, low pressure, pre-sputtering with O₂

Up to now it has been observed that high powers provide better resistivity, yet they result in degradation in transmittance. Applying O₂ during sputtering improves transmittance, yet in contrast it decreases resistivity. Also it has been observed that lower deposition pressures cause better resistivity behavior. In addition to that oxidizing

target by applying O₂ and Ar mixture in pre-sputtering also presents better transmittance behavior. Taking everything into account, in sample #13 150 W DC power is used for sputtering. As previously optimized in samples #10, #11 and #12, 3 min. pre-sputtering is applied by a mixture of 35 sccm Ar and 2 sccm O₂ with a chamber pressure of $1,4 \times 10^{-2}$ mbar. In deposition, O₂ valve is closed and sputtering is done in pure Ar plasma with 35 sccm Ar flow. Variable gate valve position is set to 420/1000 resulting in 8×10^{-3} mbar that resulted best resistivity up to now in sample #5. This pressure level is the minimum that we can ignite a plasma with moderate power. The sputtering time is set to 10 min. which gives us the desired thickness of 230 nm as shown in Figure 94.

In this sample we have reached the desired resistivity which is measured as $6,25 \times 10^{-4} \Omega \cdot \text{cm}$ and the sheet resistance which is measured as $27 \Omega \cdot \text{cm}$. Sample #13 achieved good transmittance at 1450 such as 87,733 % as seen in Figure 95. Counting in transmissivity and resistivity, sample # 13 has achieved the best performance and is used for all of our samples from now on. The summary of all the samples created in this chapter together with sputter deposition process parameters and the measurement results of thickness, electrical resistance, sheet resistance, resistivity and transmissivity is given in Table 5.

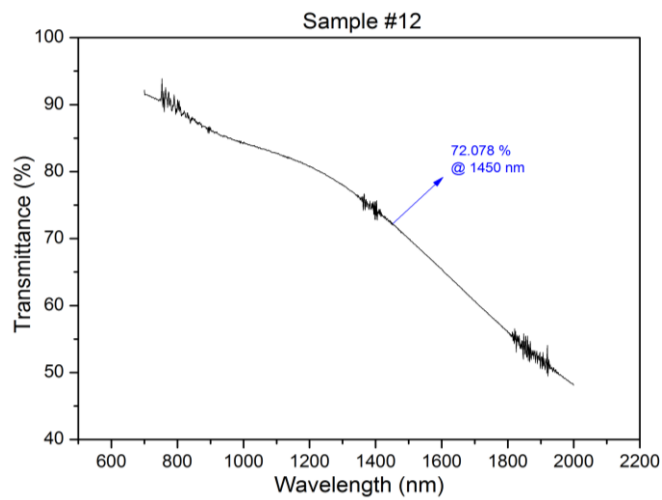


Figure 93. Transmittance graph of Sample #12

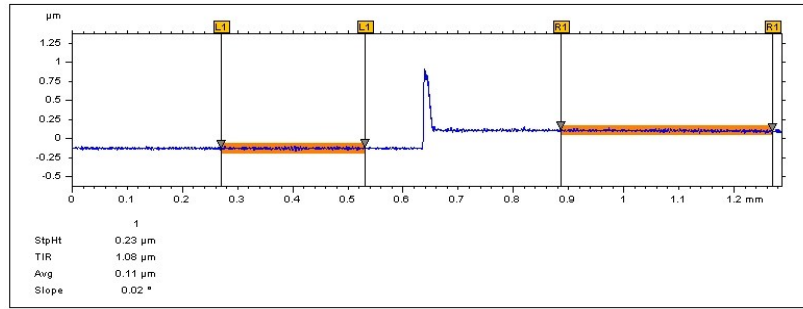


Figure 94. Measured thickness of sample #13. 10 min deposition with 150 W DC power resulted in 230 nm thickness.

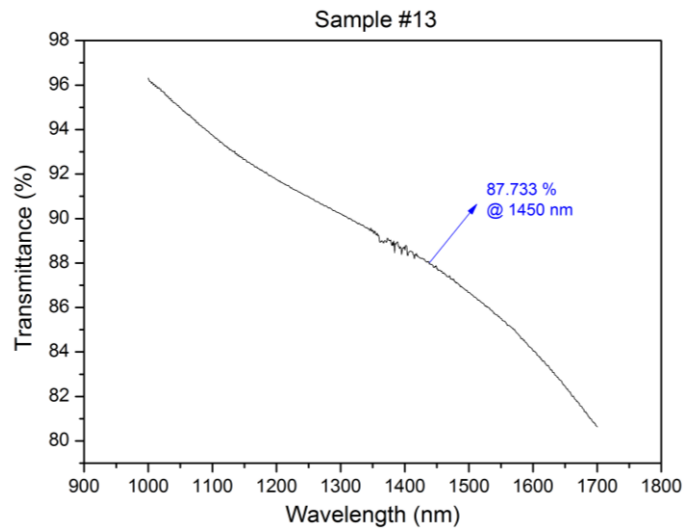


Figure 95. Transmittance graph of sample #13. 87.733 % transmittance is measured at 1450 nm